Structural and functional explorations of the MICOS Mic60-Mic19 subcomplex

Inaugural-Dissertation
to obtain the academic degree
Doctor rerum naturalium (Dr. rer. nat.)

submitted to the Department of Biology, Chemistry, Pharmacy
of Freie Universität Berlin

by

Kathrin Funck (née Lipka)

2021

Die vorliegende Arbeit wurde von Januar 2017 bis September 2021 am
Max-Delbrück-Centrum für Molekulare Medizin in der Helmholtz-Gemeinschaft (MDC)
in Berlin-Buch unter der Anleitung von Prof. Dr. Oliver Daumke angefertigt.

1. Gutachter: Prof. Dr. Oliver Daumke
2. Gutachter: Prof. Dr. Udo Heinemann

Disputation am 18.02.2022

Contents

1. Summary

Mitochondria are highly dynamic organelles of great research interest due to their involvement in many crucial biological processes, such as ATP production, calcium homeostasis or apoptosis. Several human diseases are linked to altered mitochondrial morphology and mitochondrial dynamic defects, but the underlying disease mechanisms have remained mostly unclear. The mitochondrial contact site and cristae organizing system (MICOS) complex has crucial functions in mitochondrial membrane architecture, as it is involved in the formation of crista junctions and ensures that the cristae membrane remains attached to the inner boundary membrane. This hetero-oligomeric protein complex consists of at least six components in yeast and was shown to form large complexes in the megadalton mass range. MICOS can be divided into two subcomplexes built by Mic10-Mic12-Mic26-Mic27 and Mic60-Mic19, but their architecture and even the exact stoichiometry have not been clarified yet.

In this work, the crystal structures of two fusion constructs containing conserved C-terminal domains of *Chaetomium thermophilum* Mic60 and Mic19 were determined, providing insights into the organization of the MICOS Mic60-Mic19 subcomplex. Residues involved in the interaction between the mitofilin domain of Mic60 and the CHCH domain of Mic19 were identified and analyzed in detail by biochemical and cell-based methods. These studies revealed that single amino acid exchanges can disturb the interaction *in vitro* and lead to an abnormal cristae morphology in yeast mitochondria. The predicted lipid binding site (LBS) of Mic60 is part of the mitofilin domain, which assembles as an inter-domain swapped dimer. Structure-based analysis of the dimerization interface and the membrane binding site of the mitofilin domain elucidated the structural requirements for membrane binding and remodeling.

Even though several proteins involved in mitochondrial shaping have been identified in the past, their exact mechanisms for establishing mitochondrial architecture have remained unexplored. The results of this work make a substantial contribution towards the characterization of the MICOS complex, therefore contributing to a molecular understanding of mitochondrial membrane remodeling and disease development.

2. Zusammenfassung

Die Forschung an Mitochondrien ist von großem Interesse, da diese dynamischen Organellen an vielen wichtigen zellulären Prozessen beteiligt sind, unter anderem an der Herstellung von ATP, der Calcium-Homöostase und dem programmierten Zelltod. Die Membranarchitektur und die Dynamik von Mitochondrien sind in zahlreichen menschlichen Krankheiten verändert; allerdings konnten die Mechanismen, welche zur Entstehung dieser Krankheiten führen, größtenteils noch nicht geklärt werden. Der *Mitochondrial Contact Site and Cristae Organizing System* (MICOS) Komplex leistet einen entscheidenden Beitrag für die Ausbildung und Erhaltung der mitochondrialen Architektur und trägt insbesondere dazu bei, die Cristae zu stabilisieren. MICOS setzt sich aus verschiedenen Proteinen zusammen und kann große Komplexe im Megadalton-Bereich bilden. In Hefe wurden bisher sechs Komponenten beschrieben, die in zwei Teilkomplexe assemblieren, bestehend aus Mic10-Mic12-Mic26-Mic27 und Mic60-Mic19. Allerdings konnten bisher weder die Architektur noch die exakte Zusammensetzung der Komponenten im MICOS-Komplex entschlüsselt werden.

In dieser Arbeit wurden Kristallstrukturen von zwei Fusionskonstrukten bestimmt, welche die konservierten C-terminalen Domänen von Mic60 und Mic19 aus *Chaetomium thermophilum* enthalten. Aminosäuren, die an der Interaktion zwischen der Mitofilin-Domäne von Mic60 und der CHCH-Domäne von Mic19 beteiligt sind, wurden identifiziert und charakterisiert. Mutationen in der Kontaktfläche konnten die Interaktion stören und führten zu veränderter Membranarchitektur von Hefe-Mitochondrien. Eine zuvor identifizierte Lipidbindestelle von Mic60 ist Teil der Mitofilin-Domäne, welche ein Domänen-übergreifendes Dimer im Kristall ausbildet. Durch strukturbasierte Mutagenese der Dimer- und Membran-Kontaktstellen konnten die molekularen Grundlagen der Membranbindung und -deformation entschlüsselt werden.

Obwohl bereits einige Proteine, welche an der Formgebung der Mitochondrien beteiligt sind, identifiziert wurden, blieben die genauen Mechanismen bisher weitestgehend unerforscht. Die Ergebnisse dieser Arbeit tragen wesentlich zur Charakterisierung des MICOS-Komplexes bei und führen damit zu einem erweiterten molekularen Verständnis der Membran-Deformierung in Mitochondrien und der Entstehung von mitochondrialen Erkrankungen.

3. Introduction

3.1. Mitochondria

3.1.1. Mitochondrial structure and function

Mitochondria are found in nearly all eukaryotic cells and are often described as powerhouses of the cell. They are involved in several vital biological processes including programmed cell death, β-oxidation of fatty acids and the citric acid cycle, but their most prominent role is ATP production by oxidative phosphorylation to supply the cell with metabolic energy (Westermann, 2010). The special mitochondrial architecture is characterized by the presence of two membranes, displaying different shapes and functions, and two aqueous compartments (Sjostrand, 1953; Palade, 1952; see Figure 1).

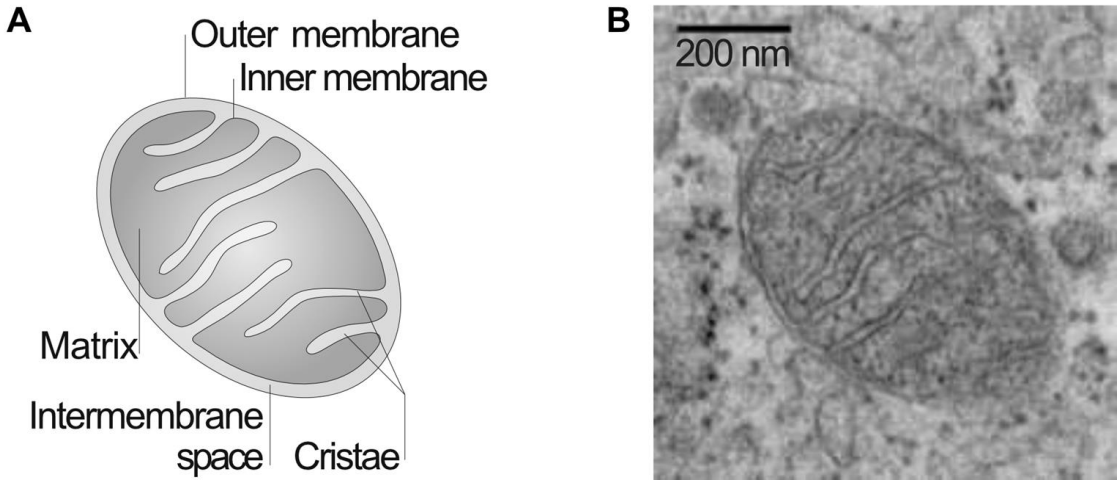

Figure 1: Mitochondrial morphology. **(A)** Schematic structure of mitochondria. **(B)** Transmission electron microscopy image of mitochondria in ultrathin sections of human fibroblast cells (adapted from Westermann, 2010).

The outer mitochondrial membrane (OMM) mediates communication with the cellular environment and functions as a barrier to the cytosol. The OMM is permeable for ions and various small molecules up to approximately 5 kDa, as it comprises channels formed by porins, so called voltage-dependent anion channels (VDAC) (Lemasters,

2007). By contrast, the inner mitochondrial membrane (IMM), which separates the matrix from the intermembrane space (IMS), is highly impermeable to almost all ions and polar molecules. Consequently, special transporters are required for the transport through the IMM (Lemasters, 2007). OMM and IMM are not completely separated due to the formation of numerous contact sites (Reichert and Neupert, 2002). The IMM is several-fold larger than the OMM, and, due to its heterogeneous structure, it can be divided into two distinct domains: the inner boundary membrane and so-called cristae. The inner boundary membrane is located in close proximity to the OMM, while cristae appear as tubular invaginations that protrude into the matrix. These two IMM domains are connected by narrow tubular structures which are termed crista junctions and have diameters of about 12-40 nm (Zick et al., 2009; Perkins et al., 1997; Rabl et al., 2009; Stephan et al., 2020).

Cristae accommodate the components of the oxidative phosphorylation machinery, whereby the V-shaped dimers of F_1F_o-ATP synthase (hydrophilic catalytic unit F_1, membrane domain F_o) are specifically located at the curved cristae edges (Strauss et al., 2008; Davies et al., 2011). In addition to their role in ATP production and apoptosis, mitochondria are involved in several other processes, like biosynthesis of Fe–S clusters and cofactors, calcium homeostasis, autophagy, stress responses and cellular signaling and they can form contact sites with the endoplasmic reticulum (ER) (Figure 2; Pfanner et al., 2021; erratum for Pfanner et al., 2019). Mitochondrial dysfunction is linked to several human diseases including neurodegenerative diseases, cancer and diabetes (Bhatti et al., 2017).

Quantitative analysis of mitochondrial membranes revealed that the mitochondrial outer membrane contains more than twice the amount of lipids (59% lipids and 41% proteins) than the inner membrane (23% lipids and 77% proteins) (Hallermayer and Neupert, 1974). A characteristic lipid of the IMM is cardiolipin, which contains four alkyl groups. Cardiolipin was shown to be important for mitochondrial membrane shaping and function and represents approximately 15% to 20% of all mitochondrial phospholipids (Paradies et al., 2019).

Mitochondria can be considered as semi-autonomous organelles, since they possess their own DNA (mtDNA) coding for different RNAs and proteins, as well as protein synthesis machinery (Westermann, 2010). However, most mitochondrial proteins are synthesized in the cytoplasm and subsequently imported into the mitochondria (see

section 3.1.2.). It is assumed that mitochondria have a common endosymbiotic origin, where α-proteobacteria were integrated into a host cell and became permanent organelles (Roger et al. 2017).

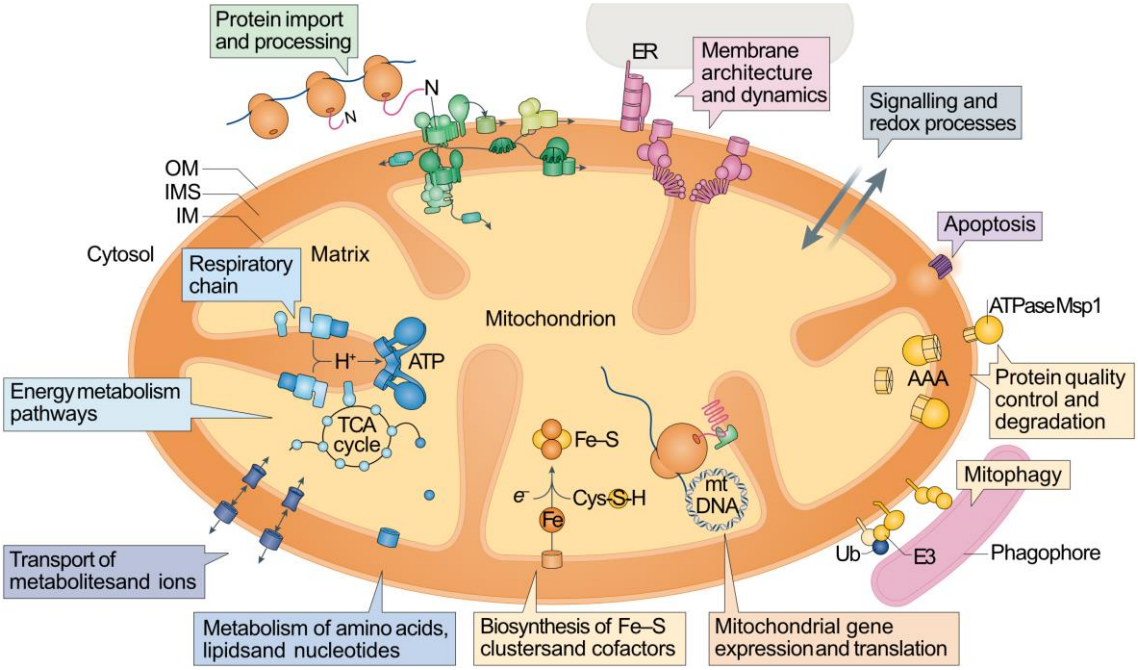

Figure 2: Overview of mitochondria and their functions. The figure indicates the large variety of functions that have been assigned to mitochondrial proteins and protein complexes; OM: outer mitochondrial membrane, IMS: intermembrane space, IM: inner mitochondrial membrane, AAA: ATP-dependent proteases of the inner membrane, E3: ubiquitin-protein ligase, ER: endoplasmic reticulum, mtDNA: mitochondrial DNA, TCA: tricarboxylic acid, Ub: ubiquitin (adapted from Pfanner et al., 2021 erratum for Pfanner et al., 2019).

3.1.2. Protein import into mitochondria

More than 1000 mitochondrial proteins have been described, but almost all of them are encoded by nuclear genes and synthetized in the cytoplasm (Sickmann et al., 2003; Wiedemann and Pfanner, 2017). Consequently, after their synthesis, these proteins have to be translocated into mitochondria via targeting signals. Mitochondrial DNA represents only 0.1% to 2% of the total mammalian DNA (Barchiesi and Vascotto, 2019). Only 1% of mitochondrial proteins, predominantly subunits of the oxidative

phosphorylation machinery, are synthesized by mitochondrial ribosomes in the matrix (Taylor et al., 2003; Horvath et al., 2015).

There are at least five main pathways for protein import into mitochondria, depending on different targeting signals (see Figure 3; Horvath et al., 2015). Most of the proteins require the translocase of the outer membrane (TOM) as entry site (Horvath et al., 2015). The presequence pathway (i) is the classical import pathway, used by the majority of proteins (Vögtle et al., 2009). These preproteins are synthetized with a cleavable N-terminal targeting sequence, which can form an amphipathic α-helix and is recognized by the TOM complex (Roise et al., 1986; Abe et al., 2000). Translocation through the outer mitochondrial membrane occurs via Tom40, a β-barrel protein and voltage-dependent anion channel (Hill et al., 1998; Bayrhuber et al., 2008). After translocation into the intermembrane space, the preproteins are recognized by the translocase of the inner membrane (TIM) 23 complex and transported either into the matrix via the presequence translocase-associated motor (PAM) using ATP or laterally released to the inner membrane (Chacinska et al., 2005; Mokranjac and Neupert, 2010). In both cases, cleavage of the N-terminal targeting sequence, by the mitochondrial processing peptidase (MPP) located in the matrix, generates the mature proteins (Hawlitschek et al., 1988; Taylor et al., 2001). In all other pathways, internal targeting signals are not cleaved after import and remain part of the protein.

Inner membrane proteins possessing multiple transmembrane domains, predominantly carrier proteins, are imported via the carrier pathway (ii) (Figure 3). In contrast to the previously described pathway, after import via the TOM complex, small TIM chaperones located in the intermembrane space transport the carrier proteins to the TIM22 complex, where membrane insertion occurs in a membrane potential-dependent way (Sirrenberg et al., 1996; Koehler et al., 1998; Rehling et al., 2004).

Many IMS proteins, containing a characteristic cysteine motif, are imported by TOM and the mitochondrial intermembrane space import and assembly (MIA) pathway (iii) (Figure 3; Chacinska et al., 2004). After formation of mixed disulfide bonds with Mia40, oxidized proteins are released to the IMS (Herrmann and Riemer, 2012).

There are at least two pathways for insertion of outer mitochondrial membrane proteins (Figure 3). Import and insertion of β-barrel proteins (iv) involves the TOM complex, small TIM IMS chaperones and the sorting and assembly machinery (SAM) complex (Wiedemann et al., 2003; Höhr et al., 2015). Several other outer membrane proteins,

which are anchored by one or more transmembrane helices (for example receptors), are imported via the mitochondrial import (MIM) complex (v), involving Mim1, Mim2 and the TOM complex (Becker et al., 2008; Hulett et al., 2008; Dimmer et al., 2012). The detailed elucidation of this pathway is still ongoing.

However, the import mechanism for many precursor proteins has not been identified yet, and aside from the classical import pathways described above, there are additional pathways as well as combinations of different import and processing pathways (Wiedemann and Pfanner, 2017).

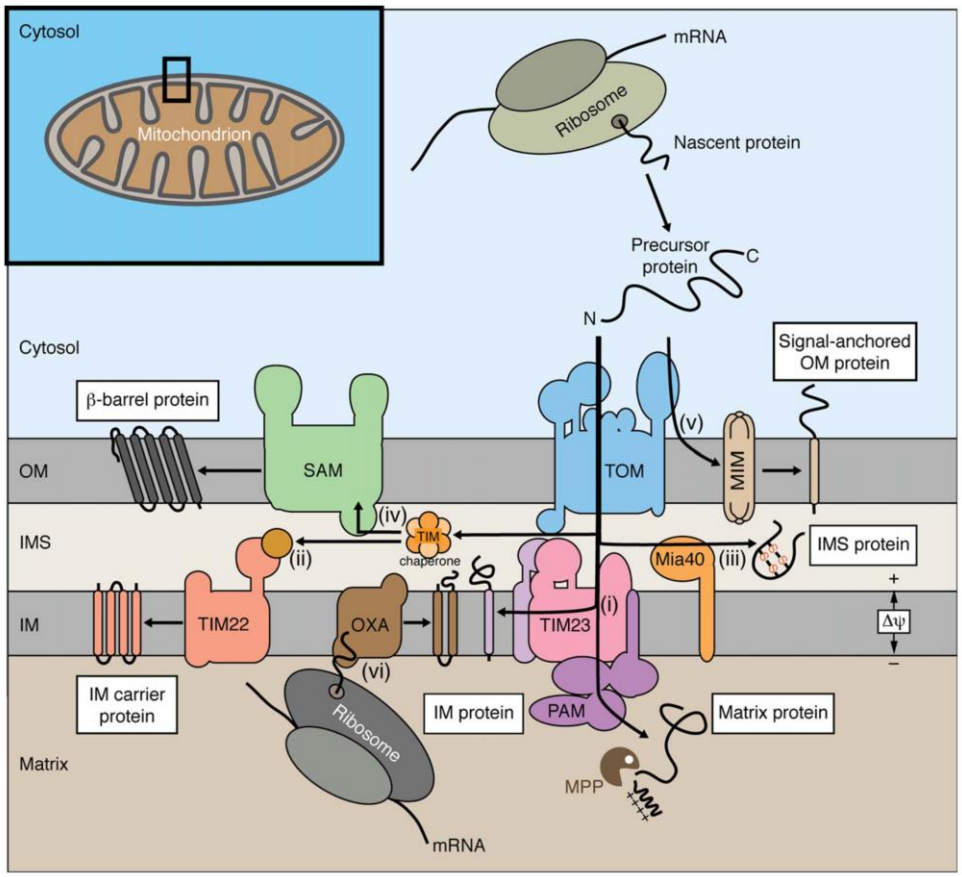

Figure 3: Biogenesis of mitochondrial proteins. Different import pathways for mitochondrial proteins synthesized on cytosolic ribosomes are indicated (i - v). vi: Pathway for hydrophobic proteins synthesized by mitochondrial ribosomes in the matrix; OM: outer mitochondrial membrane, IMS: intermembrane space, IM: inner mitochondrial membrane, TOM: translocase of the outer membrane, TIM: translocase of the inner membrane, PAM: presequence translocase-associated motor, MPP: mitochondrial processing peptidase, MIA: mitochondrial intermembrane space import and assembly, SAM: sorting and assembly machinery, MIM: mitochondrial import complex, mtDNA: mitochondrial DNA, OXA: cytochrome oxidase activity translocase, Δψ: membrane potential across the inner mitochondrial membrane (drives protein import via TIM23 and TIM22) (from Horvath et al., 2015).

3.1.3. Mitochondrial dynamics and membrane shaping

Mitochondria are highly dynamic organelles, which continuously divide and fuse, and defects in mitochondrial dynamics are linked to neurodegenerative diseases such as Parkinson's disease (Westermann, 2010; Deng et al., 2008). Mitochondrial morphology can be quite diverse, since mitochondria can appear as interconnected networks or mitochondrial fragments (Westermann, 2010). A cell type-specific appearance is common to mitochondria: For example, they are densely packed in cortical astrocytes and predominantly isolated from each other in hepatocytes, but even within individual cells, different mitochondrial morphologies have been observed (Collins et al., 2002).

A characteristic feature of mitochondria is the occurrence of two membranes and the formation of cristae and crista junctions, whereby cristae can vary in size and shape (Figure 4; Colina-Tenorio et al., 2020). Moreover, cristae were shown to continuously undergo membrane remodeling cycles at a timescale of seconds, where they can separate and appose (Kondadi et al., 2020). Reversible changes in cristae morphology are connected to the metabolic state of mitochondria, as altering the ADP level shifts the ratio between intracristal space and matrix volume. (Hackenbrock, 1966; Colina-Tenorio et al., 2020). Even within one mitochondrion, individual cristae can be functionally independent displayed by different membrane potentials (Wolf et al., 2019). It was suggested that crista junctions limit the diffusion of ions, certain metabolites, like ADP, and proteins between IMS and intracristal space (Perkins et al., 1997; Mannella, 2006).

The antagonistic processes fusion and fission need to be tightly controlled to keep maintenance of mitochondrial morphology or shift if physiological conditions change (Westermann, 2010). Several proteins are involved in membrane shaping of mitochondria. Interestingly, many of these belong to the dynamin superfamily. Dynamin-like proteins (Dlps) mediate membrane fission of mitochondria in mammals (Dnm1 in yeast), whereas mitofusins and OPA1 mediate fusion of the OMM and IMM, respectively (in yeast: Fzo1 and Mgm1) (Praefcke and McMahon, 2004). OPA1 is also involved in maintenance of the mitochondrial morphology and cristae remodeling, as knockdown results in mitochondrial fragmentation and apoptosis due to cristae reorganization and cytochrome c release (Olichon et al., 2003; Frezza et al., 2006; Yamaguchi et al., 2008; Scorrano et al., 2002). It was reported that the crista junction opening diameter is controlled by OPA1 oligomers, which disassemble during

apoptosis (Frezza et al., 2006; Yamaguchi et al., 2008). Mgm1, the yeast orthologue of human OPA1, seems to be required for cristae maintenance as well (Meeusen et al., 2006; Amutha et al., 2004).

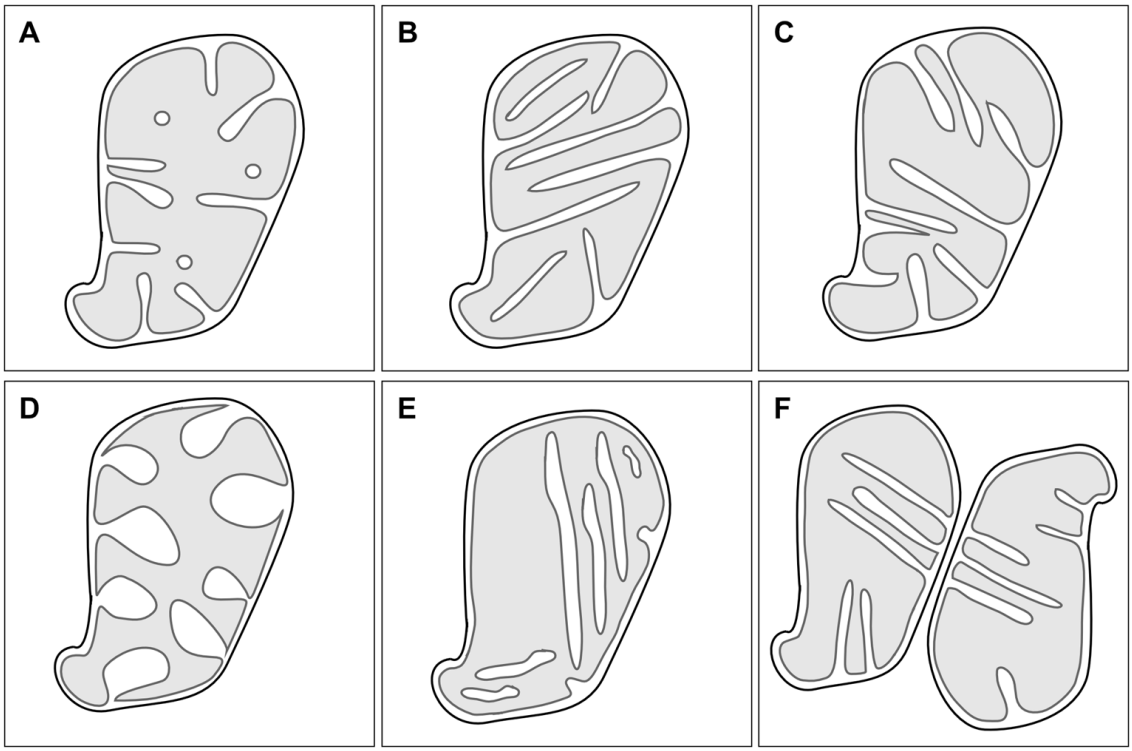

Figure 4: Mitochondrial cristae architecture and dynamics. Mitochondria dynamically change their morphology and different mitochondrial states are indicated. **(A)** Tubular cristae architecture. Cristae are connected to the inner boundary membrane by narrow crista junctions and appear in a circular shape in cross sections. **(B)** Cisternae-like cristae architecture. Cristae are connected to the inner boundary membrane by narrow crista junctions and consist of relatively flat cisternae with strongly curved rims. **(C)** Orthodox state of mitochondrial morphology displayed in the presence of low ADP concentrations and slow respiration. Low cristae volume and expanded matrix are characteristic. **(D)** Condensed state. High ADP concentrations support efficient oxidative phosphorylation. Expanded cristae volume and decreased matrix volume are characteristic. **(E)** Inner membranes accumulate as lamellar stacks. Lack of crista junctions, so that cristae membrane is not connected to the inner boundary membrane. This morphology is characteristic in the absence of a functional mitochondrial contact site and cristae organizing system (MICOS) complex. **(F)** Adjacent mitochondria can be connected by inter-mitochondrial junctions. Outer mitochondrial membrane is depicted in black and inner mitochondrial membrane in dark grey; intermembrane space (including intracristal space) is depicted in white and matrix in light grey (adapted from Colina-Tenorio et al., 2020).

The F_1F_o-ATP synthase is also involved in cristae shaping and stabilization. Deletion of subunits e and g, which are essential for dimerization, but not for its enzymatic activity, resulted in abnormal cristae morphology with absent or balloon-shaped cristae (Paumard et al., 2002; Davies et al., 2012; Arnold et al., 1998; Rabl et al., 2009). As the V-shaped F_1F_o-ATP synthase dimers assemble into rows along highly curved edges of cristae tips, the intrinsic dimer angle is assumed to impose local curvature (Paumard et al., 2002; Strauss et al., 2008; Davies et al., 2012).

The phospholipid cardiolipin is important for mitochondrial function and for instance required for structural integrity and enzymatic function of the oxidative phosphorylation machinery and optimal activity of many mitochondrial carrier proteins (Paradies et al., 2019). Furthermore, cardiolipin was shown to be a crucial factor for mitochondrial membrane organization, as it is involved in fusion, fission and cristae organization, and can induce negative curvature (Ikon and Ryan, 2017).

Another crucial factor for mitochondrial morphology is the mitochondrial contact site and cristae organizing system (MICOS) complex, which is described in detail in the next sections. The MICOS complex is essential for membrane dynamics, as it was shown to control the distribution of crista junctions and trigger the remodeling of pre-existing cristae (Stephan et al., 2020; Kondadi et al., 2020). Moreover, it is reported that OPA1 and F_1F_o-ATP synthase influence the position of the MICOS complex to stabilize crista junctions (Stephan et al., 2020). Thus, the interplay between several proteins seems to mediate mitochondrial shaping, while more and more proteins involved in membrane remodeling and maintenance are still discovered. Further studies are necessary to unravel the molecular details of mitochondrial membrane organization and dynamics.

3.2. MICOS complex

3.2.1. Discovery of the MICOS complex and uniform nomenclature

The mitochondrial contact site and cristae organizing system (MICOS) complex is a large protein complex anchored in the inner mitochondrial membrane (IMM) close to crista junctions and is crucial for mitochondrial membrane architecture (von der

Malsburg et al., 2011; Hoppins et al., 2011; Harner et al., 2011; Jans et al., 2013). Mitochondria lacking the MICOS complex or certain MICOS components show an altered phenotype, where the cristae membrane is detached from the inner boundary membrane and accumulates in large sheet-like stacks or onion-like structures (John et al., 2005; Rabl et al., 2009; von der Malsburg et al., 2011; Hoppins et al., 2011; Harner et al., 2011; Figure 5).

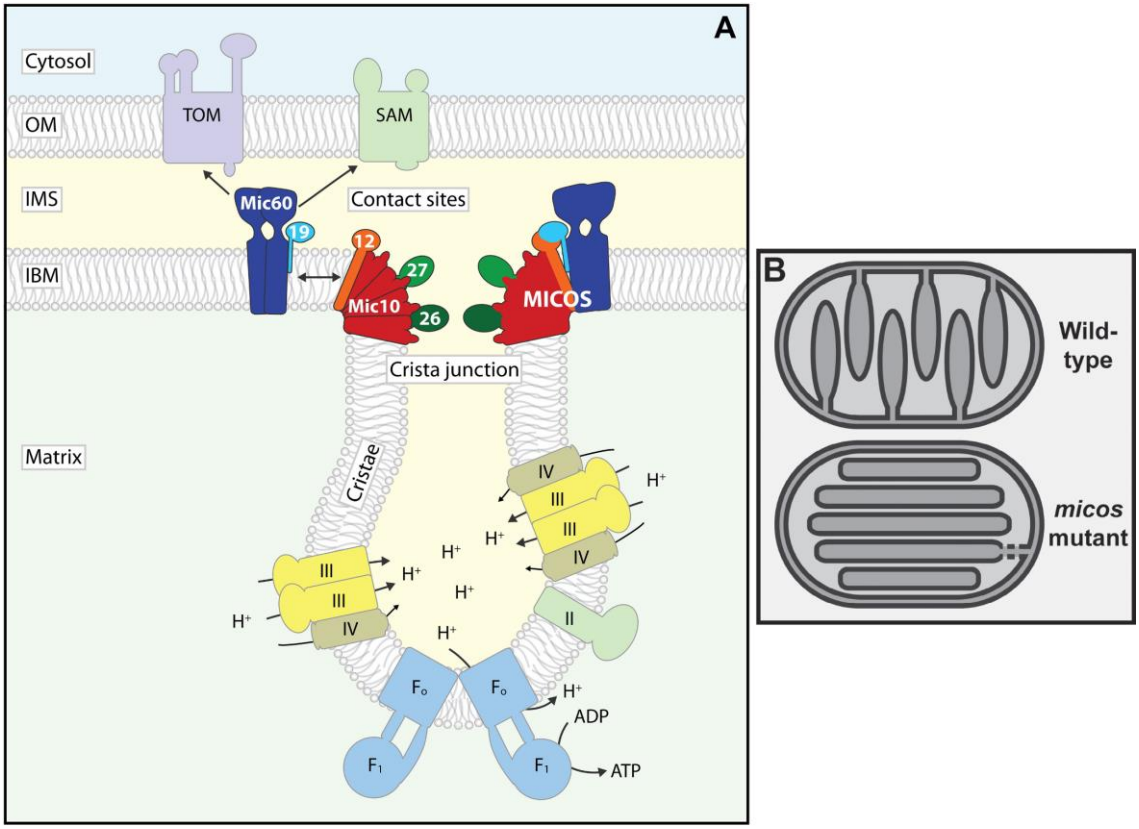

Figure 5: Mitochondrial contact site and cristae organizing system (MICOS) complex in yeast. (A) MICOS is enriched at crista junctions and forms contact sites with several outer membrane proteins via the Mic60 subcomplex. Respiratory chain complexes (II, III, IV) and F_1F_o-ATP synthases are enriched in the cristae membranes. OM: outer mitochondrial membrane, IMS: intermembrane space, IBM: inner boundary membrane (inner mitochondrial membrane), TOM: translocase of the outer membrane, SAM: sorting and assembly machinery. **(B)** Architecture of wild-type and *micos* mutant mitochondria. Cristae are connected to the inner boundary membrane by narrow crista junctions in wild-type mitochondria. In *micos* mutant mitochondria, cristae membranes form internal membrane stacks. Most of cristae membrane is detached from the inner boundary membrane and crista junctions are lacking (adapted from Rampelt et al., 2017b and from Pfanner et al., 2014).

Table 1: MICOS nomenclature (adapted from Pfanner et al., 2014).

Standard name	Former names	References
Complex		
MICOS	MINOS, MitOS, MIB, Mitofilin complex, and Fcj1 complex	Xie et al., 2007; Rabl et al., 2009; Darshi et al., 2011; Harner et al., 2011; Hoppins et al., 2011; von der Malsburg et al., 2011; Alkhaja et al., 2012; An et al., 2012; Bohnert et al., 2012; Ott et al., 2012; Jans et al., 2013; Weber et al., 2013
Subunits		
Mic10	Mcs10, Mio10, Mos1, MINOS1	Harner et al., 2011; Hoppins et al., 2011; von der Malsburg et al., 2011; Alkhaja et al., 2012; Itoh et al., 2013; Jans et al., 2013; Varabyova et al., 2013
Mic12	Aim5, Fmp51, Mcs12, and in metazoa Mic13, QIL1	Hess et al., 2009; Harner et al., 2011; Hoppins et al., 2011; von der Malsburg et al., 2011; Varabyova et al., 2013; Guarani et al., 2015; Huynen et al., 2016
Mic19	Aim13, Mcs19, CHCH-3, CHCHD3, MINOS3	Xie et al., 2007; Hess et al., 2009; Darshi et al., 2011; Head et al., 2011; Alkhaja et al., 2012; Ott et al., 2012; Jans et al., 2013; Varabyova et al., 2013
Mic25 (metazoan Mic19 homologue)	CHCHD6, CHCM1	Xie et al., 2007; An et al., 2012; Huynen et al., 2016
Mic26	Mcs29, Mio27, APOO, Mos2, and Mic23 in metazoa	Harner et al., 2011; Hoppins et al., 2011; von der Malsburg et al., 2011; Koob et al., 2015; Ott et al., 2015; Huynen et al., 2016
Mic27	Aim37, Mcs27, APOOL, MOMA-1, and Mic28 in Saccharomycetales	Hess et al., 2009; Harner et al., 2011; Head et al., 2011; Hoppins et al., 2011; von der Malsburg et al., 2011; Weber et al., 2013; Huynen et al., 2016; Munoz-Gomez et al., 2015
Mic60	Fcj1, Aim28, Fmp13, Mitofilin, HMP, IMMT, MINOS2	Icho et al., 1994; Odgren et al., 1996; Gieffers et al., 1997; John et al., 2005; Wang et al., 2008; Rabl et al., 2009; Rossi et al., 2009; Mun et al., 2010; Park et al., 2010; Körner et al., 2012; Zerbes et al., 2012; Itoh et al., 2013; Varabyova et al., 2013

The MICOS complex was identified in independent studies in parallel (von der Malsburg et al., 2011; Harner et al., 2011; Hoppins et al., 2011; Alkhaja et al., 2012) and afterwards uniformly termed MICOS, as different names were used by these research groups (Pfanner et al., 2014). Single MICOS proteins were already discovered beforehand, for example, yeast Mic60 was identified to localize to mitochondria in 1996 (Odgren et al., 1996). Accordingly, all MICOS components were uniformly named Mic, with the following number displaying the approximate molecular weight (see Table 1; Pfanner et al., 2014). This nomenclature is more or less independent of the species, as the MICOS complex is conserved in eukaryotes, especially the core components (Hoppins et al., 2011; Pfanner et al., 2014; Huynen et al., 2016; Munoz-Gomez et al., 2015).

All MICOS proteins are nucleus-encoded and imported into mitochondria via different mechanisms (Ueda et al., 2019; see also 3.2.2. - 3.2.4.). Mic60 and Mic10 are considered as the core MICOS components, since their lack leads to almost complete dissociation of the complex, inducing loss of crista junctions and abnormal mitochondrial morphology (Figure 5; von der Malsburg et al., 2011; Hoppins et al., 2011; Harner et al., 2011; John et al., 2005; Alkhaja et al., 2012). In comparison, the absence of other Mic proteins results in less severe effects, displaying intermediate phenotypes of mitochondria (between wild-type and Mic60 or Mic10 knockout) (von der Malsburg et al., 2011; Rabl et al., 2009; Hoppins et al., 2011; Harner et al., 2011). MICOS seems to be likewise involved in organization of mtDNA nucleoids, as deletion of Mic60 or Mic10 results in nucleoid aggregation (Itoh et al., 2013; Li et al., 2016). The importance of MICOS integrity is further emphasized by several observations, which show that lack of MICOS proteins resulted in fragmentation of the mitochondrial network and impaired respiration (Darshi et al., 2011; Zerbes et al., 2012; Weber et al., 2013; Koob et al., 2015; Guarani et al., 2015; Anand et al., 2020).

MICOS was shown to form large complexes in the MDa range, but the exact composition and stoichiometry has not been clarified yet (von der Malsburg et al., 2011; Harner et al., 2011). This hetero-oligomeric complex can be divided into the two subcomplexes Mic10-Mic12-Mic26-Mic27 and Mic60-Mic19 (additionally Mic25 in mammals), which independently localize to crista junctions (Bohnert et al., 2015; Guarani et al., 2015; Friedman et al., 2015; Anand et al., 2016; Tirrell et al., 2020). Several studies reported that Mic12 mediates the connection of both subcomplexes

(Guarani et al., 2015; Anand et al., 2016; Zerbes et al., 2016). The Mic60 subcomplex seems to be involved in the formation of contact sites between the IMM and OMM and protein import, as it interacts with proteins of the OMM (von der Malsburg et al., 2011; Xie et al., 2007; Ott et al., 2012; Körner et al., 2012; Zerbes et al., 2016). In addition, the membrane deforming activity of the Mic10 subcomplex is crucial for membrane shaping at crista junctions (Bohnert et al., 2015; Barbot et al., 2015; Guarani et al., 2015; Anand et al., 2016).

3.2.2. Mic60

Mic60 was first described in 1994 and termed HMP (heart muscle protein) due to the strong expression in heart muscle cells, but its function remained unclear (Icho et al., 1994). Human Mic60 was later renamed mitofilin, as it was specifically localized to mitochondria and expressed in different tested human cell types (Odgren et al., 1996). Furthermore, Mic60 was shown to be anchored in the IMM exposing most of the protein to the IMS (Odgren et al., 1996; Gieffers et al., 1997; Figure 6). Several years later, Mic60 was found to be enriched at crista junctions, prior to the discovery of the MICOS complex (John et al., 2005; Rabl et al., 2009). Down regulation of Mic60 in HeLa cells resulted in altered mitochondrial membrane organization, as well as slightly increased apoptosis and reduced proliferation, indicating a function of Mic60 in cristae morphology (John et al., 2005). Deletion of Mic60 in yeast (termed Fcj1) or *C. elegans* (termed IMMT) led to similar alterations of mitochondrial ultrastructure, with stacked or onion-like cristae and a decreased number of crista junctions (Rabl et al., 2009; Mun et al., 2010; John et al., 2005). These observations point to a conserved function of Mic60 in the formation of crista junctions in mitochondria, despite the low sequence identity of yeast Mic60 with *C. elegans* (24% and 27% for the two homolog genes) or human mitofilin (13%) (Mun et al., 2010; Rabl et al., 2009). Independent studies reported different effects of Mic60 down-regulation on mitochondrial dynamics: mitochondrial fusion and fission was not affected in general (John et al., 2005) or significantly decreased (Li et al., 2016).

Mic60 is imported into mitochondria by the classical presequence pathway (see 3.1.2.) via its N-terminal mitochondrial targeting sequence, which is cleaved afterwards (Gieffers et al., 1997). The domain architecture of Mic60 was elucidated stepwise,

showing that Mic60 consists of an N-terminal mitochondrial targeting sequence, followed by a single transmembrane (TM) helix (Odgren et al., 1996; Gieffers et al., 1997), a coiled-coil domain (Icho et al., 1994; Odgren et al., 1996) and a conserved mitofilin domain at the C-terminus (Rabl et al., 2009; von der Malsburg et al., 2011; Körner et al., 2012; Zerbes et al., 2012). Furthermore, a lipid binding site was located before the assigned mitofilin domain (Hessenberger et al., 2017; Tarasenko et al., 2017). Although the domains of Mic60 are functionally conserved, the overall size of Mic60 differs between distinct species, due to varying lengths of the coiled-coil domain. For example, the yeast Mic60 protein has a predicted mass of 61 kDa, human Mic60 84 kDa and the two homologues of *C. elegans* Mic60 76 kDa and 73 kDa. Mitochondria containing a Mic60 variant without the mitofilin domain show similar cristae morphology as mitochondria lacking Mic60 completely, while deletion of the coiled-coil domain generates an intermediate phenotype, revealing the importance of the mitofilin domain for proper function (Zerbes et al., 2012; Körner et al., 2012).
Overexpression of Mic60 increases the number of crista junctions, as well as the appearance of branched cristae (Rabl et al., 2009). Moreover, it seems that an antagonism between Mic60 and F_1F_o-ATP synthase controls membrane curvature (Rabl et al., 2009).

Mic60 is also able to homo-oligomerize and was shown to be present in a large multimeric protein complex (John et al., 2005; Rabl et al., 2009). In addition to Mic60, this complex contains Mic19, Mic25, Sam50, metaxin 1, metaxin 2 and DnaJC11 in human mitochondria (Xie et al., 2007).
The mitofilin domain seems to be crucial for the integrity of the MICOS complex, as a Mic60 construct lacking the mitofilin domain was unable to co-isolate other MICOS components in considerable amounts (Zerbes et al., 2012). In comparison, deletion of the Mic60 coiled-coil domain impaired primarily the co-isolation of Mic19 and Mic12 (Zerbes et al., 2012). In pull-down experiments, the purified mitofilin domain (yeast) bound to full-length Mic60 (derived from mitochondrial lysate), pointing to a function of the mitofilin domain in Mic60 homo-oligomer formation (Körner et al., 2012). Furthermore, the mitofilin domain was shown to be involved in the interaction with TOM and SAM complex (Körner et al., 2012; Zerbes et al., 2012).

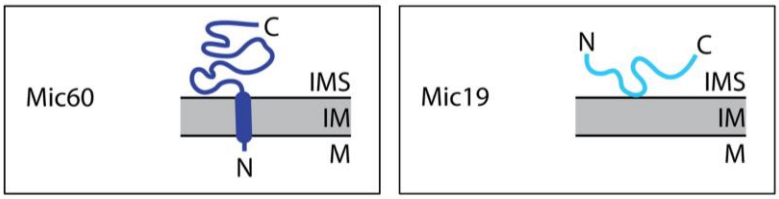

Figure 6: Predicted topology of Mic60 and Mic19. N: N-terminus, C: C-terminus, IMS: intermembrane space, IM: inner mitochondrial membrane, M: matrix. Proteins are colored as in Figure 5 (adapted from Rampelt et al., 2017b).

3.2.3. Mic19

Mouse Mic19 (earlier termed CHCH domain-containing protein 3/CHCHD3) was identified as a mitochondrial protein in 2004, and later described as a substrate for cAMP-dependent Protein Kinase (PKA) (Fukada et al., 2004; Schauble et al., 2007). Within mammals, Mic19 is highly conserved exhibiting a sequence similarity of 92% between human and mouse (Darshi et al., 2011). Independently, *S. cerevisiae* Mic19 (Aim13), together with Mic12 (Aim5) and Mic27 (Aim37), were identified in a screen for proteins that influence mitochondrial biogenesis and inheritance, and therefore named Aim: altered inheritance of mitochondria (Hess et al., 2009; von der Malsburg et al., 2011).

Mic19 was shown to be important for crista integrity as knockdown in HeLa cells resulted in altered ultrastructure (from lamellar to tubular profiles) and mitochondrial fragmentation (Darshi et al., 2011). Subsequently, several studies have demonstrated the interaction between Mic60 and Mic19 in different species and their function on mitochondrial morphology (Head et al., 2011; Darshi et al., 2012; Ding et al., 2015; Ott et al., 2015; von der Malsburg et al., 2011; Hoppins et al., 2011; Harner et al., 2011). Mic25 (CHCHD6) shares similar domain architecture with Mic19 and was also shown to interact with Mic60 (An et al., 2012; Ding et al., 2015). Mic19 knockdown seems to have no effect on stability of Mic25 (Li et al., 2016).

Mic19 and Mic25 are peripheral proteins of the intermembrane space, and the only MICOS components that do not contain a transmembrane domain, yet appear to be membrane-associated (von der Malsburg et al., 2011; Hoppins et al., 2011; Harner et

al., 2011; Darshi et al., 2011; An et al., 2012; Figure 6). Mic19 contains two predicted domains: A central predicted coiled-coil domain, which is also termed DUF737 domain (domain of unknown function), and a conserved CHCH (coiled-coil-helix-coiled-coil-helix) domain at the C-terminus (Schauble et al., 2007; Darshi et al., 2011; von der Malsburg et al., 2011).

Mic19 was shown to be myristoylated at the N-terminus, which is an important feature for interaction with the SAM complex (Darshi et al., 2011; Utsumi et al., 2018). The CHCH domain of human Mic19 contains four conserved cysteine residues arranged in a twin Cys-X_9-Cys motif, while yeast Mic19 contains only two conserved cysteine residues showing a single Cys-X_{10}-Cys motif (Darshi et al., 2011; Sakowska et al., 2015). These cysteine residues are essential for proper folding of Mic19 (Darshi et al., 2012). Mic19 is imported into mitochondria via the MIA pathway (see 3.1.2.), with the involvement of the CHCH domain and the N-terminal myristoyl group (Darshi et al., 2012; Sakowska et al., 2015; Utsumi et al., 2018; Ueda et al., 2019). In mitochondria, yeast and human Mic19 are predominantly present in the oxidized form, characterized by one (yeast) or two (human) intramolecular disulfide bonds present in the CHCH domain (Sakowska et al., 2015). Furthermore, the oxidized form of Mic19 was found in the MICOS complex and seems to be important for the stability and function of the complex; even though Mic19 mutants with mutated cysteine residues were still able to interact with Mic60, albeit less efficiently (Sakowska et al., 2015; Darshi et al., 2012).

Steady-state protein levels of Mic60 and Mic19 are mutually dependent, as knockdown of Mic60 resulted in strong reduction or complete loss of Mic19, while lack of Mic19 leads to a moderate Mic60 reduction (von der Malsburg et al., 2011; Harner et al., 2011; Hoppins et al., 2011; Li et al., 2016; Ott et al., 2015; Darshi et al., 2011; Sakowska et al., 2015). A potential reason for this interplay represents the finding that Mic60 is a substrate of mitochondrial i-AAA protease Yme1L, while binding of Mic19 seems to cover the Yme1L recognition site (Li et al., 2016). Moreover, deletion of either the coiled-coil or the mitofilin domain of Mic60 resulted in considerably lower amounts of Mic19 (Zerbes et al., 2012). The Mic60-Mic19 interaction occurs predominantly via the mitofilin and the CHCH domain (Hessenberger et al., 2017; Darshi et al., 2011), while another interface involving Mic19 and coiled-coil domain of Mic60 was also described (Li et al., 2016).

3.2.4. Mic10 subcomplex

The Mic10 subcomplex comprises Mic10, Mic12, Mic26 and Mic27 (Bohnert et al., 2015; Guarani et al., 2015; Friedman et al., 2015; Anand et al., 2016). Most of the species contain only Mic26 or Mic27, and human Mic12 is also termed Mic13 or QIL1 (see 3.2.5; Huynen et al. 2016; Munoz-Gomez et al., 2015). Prior to the discovery of the MICOS complex, *C. elegans* Mic27 (MOMA-1) was already described to control cristae morphology together with Mic60 (and Mic19) (Head et al., 2011).

The central MICOS component Mic10 contains two transmembrane helices, whereby both termini are exposed to the IMS (von der Malsburg et al., 2011; Hoppins et al., 2011; Alkhaja et al., 2012; Bohnert et al., 2015; Barbot et al., 2015; Figure 7). In contrast to Mic60, Mic10 does not possess a cleavable mitochondrial targeting sequence, but a conserved positive stretch of three residues between both transmembrane segments, which is important for targeting of Mic10 to the inner mitochondrial membrane (Bohnert et al., 2015). Each of the transmembrane segments comprises a conserved glycine motif (GxGxGxG) and both motifs are crucial for Mic10 homo-oligomerization and crista junction formation (Bohnert et al., 2015; Barbot et al., 2015). F_1F_o-ATP synthase subunit c was also shown to homo-oligomerize through such a motif (Vonck et al., 2002; Alavian et al., 2014). Mic10 is able to form large oligomers and induce membrane curvature (Barbot et al., 2015; Bohnert et al., 2015). Membrane curvature might be generated by an asymmetric wedge shape of Mic10 (Barbot et al., 2015). In line with this idea, Mic10 seems to be more abundant within the MICOS complex than other components (Harner et al., 2011; Bohnert et al., 2015).

Mic12 is anchored in the inner mitochondrial membrane by a single transmembrane segment (von der Malsburg et al., 2011; Hoppins et al., 2011; Harner et al., 2011; Guarani et al., 2015; Anand et al., 2016; Figure 7). While yeast Mic12 was already known to be part of the MICOS complex in 2011, human Mic12 (Mic13, QIL1) was discovered some years later (Guarani et al., 2015; Anand et al., 2016). Mic12 is thought to couple both MICOS subcomplexes, since Mic12 deletion impairs MICOS assembly (approx. 700 kDa), resulting in Mic60 subcomplex accumulation (approx. 500 kDa), and cross-linking of Mic10 and Mic60 is strongly reduced (Guarani et al., 2015; Anand et al., 2016; Zerbes et al., 2016).

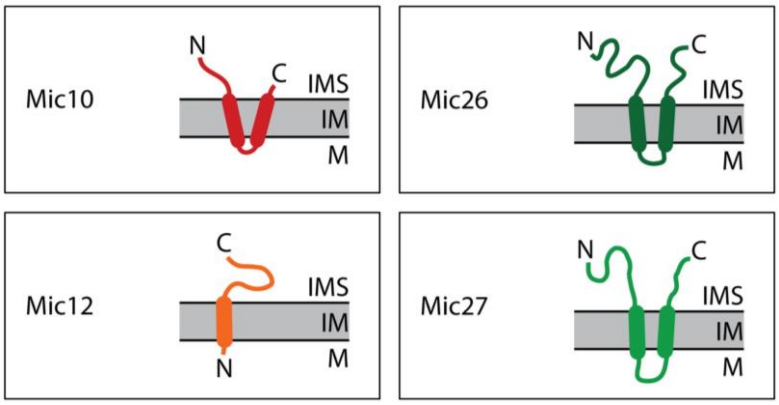

Figure 7: Predicted topology of Mic10, Mic12, Mic26 and Mic27. N: N-terminus, C: C-terminus, IMS: intermembrane space, IM: inner mitochondrial membrane, M: matrix. Proteins are colored as in Figure 5 (adapted from Rampelt et al., 2017b).

Mic26 and Mic27 contain two predicted transmembrane helices (von der Malsburg et al., 2011; Hoppins et al., 2011; Harner et al., 2011; Weber et al., 2013; Figure 7). Both human homologs, Mic26 (APOO) and Mic27 (APOOL), were identified as important MICOS components and contain a predicted mitochondrial targeting signal at the N-terminus (Weber et al., 2013; Koob et al., 2015; Ott et al., 2015). Human Mic26 can be glycosylated, but only the non-glycosylated form is targeted to mitochondria and integrated into the MICOS complex (Koob et al., 2015; Ott et al., 2015; Turkieh et al., 2014). Yeast Mic27 was shown to exert a stabilizing effect on Mic10 oligomers, but Mic10 oligomerization occurs independently of Mic27 (Bohnert et al., 2015; Zerbes et al., 2016). Furthermore, yeast Mic26 and Mic27 seem to exhibit antagonistic functions, as Mic26 was reported to destabilize Mic10 oligomers (Rampelt et al., 2018). In contrast to the Mic60 subcomplex, the Mic10 subcomplex was reported to be dependent on cardiolipin, which stabilizes Mic10 oligomers (Friedman et al., 2015; Rampelt et al., 2018). In line with this, human Mic27 was demonstrated to bind cardiolipin, while deletion of Mic26 and Mic27 lead to reduced cardiolipin levels in mitochondria (Weber et al., 2013; Anand et al., 2020).

Deletion of one MICOS component influences the steady-state level of other members of the complex, but there seem to be some differences in various cell types (von der Malsburg et al., 2011; Darshi et al., 2011; Hoppins et al., 2011; Harner et al., 2011; Sakowska et al., 2015; Ott et al., 2015; Li et al., 2016). For example, in yeast

mitochondria lacking Mic10, Mic27 was strongly reduced or not detectable, while Mic26 and Mic12 levels were moderately diminished (von der Malsburg et al., 2011; Hoppins et al., 2011; Sakowska et al., 2015). Interestingly, deletion of Mic60 not only resulted in a dramatic reduction of Mic19, but also a moderate reduction of the steady-state levels of Mic12, Mic26 and Mic27 (von der Malsburg et al., 2011; Sakowska et al., 2015).

3.2.5. Evolution of the MICOS complex

The MICOS complex was identified in different organisms due to its common and crucial function, hence, the extent of conservation and distribution are highly interesting (Pfanner et al., 2014). The evolution of MICOS components has been analyzed in detail by Huynen et al. (2016) and Munoz-Gomez et al. (2015) (Figure 8).
Given their essential functions for cristae morphology (see 3.2.1), it is not surprising that Mic60 and Mic10 are the most conserved components of the MICOS complex (Huynen et al., 2016; Munoz-Gomez et al., 2015). The conserved glycine-rich motif of Mic10 and the mitofilin domain of Mic60, which are essential for their function, are conserved among eukaryotes (Bohnert et al., 2015; Rabl et al., 2009; Körner et al., 2012; Huynen et al., 2016; Munoz-Gomez et al., 2015). Both proteins were consistently found in every major lineage of eukaryotes, where Mic10 seems to be the most widespread MICOS component and Mic60 the oldest (Huynen et al., 2016; Munoz-Gomez et al., 2015). Mic60 homologues were even found in α-proteobacteria, which share a conserved domain architecture (TM domain, coiled-coil domain and mitofilin domain), pointing to a conserved function (Munoz-Gomez et al., 2015). In line with this, α-proteobacteria can exhibit intracytoplasmic membrane structures, including vesicular, tubular or plate-like structures (Drews and Golecki, 1995; Tucker et al., 2010; Munoz-Gomez et al., 2015). The loss of MICOS components (especially Mic60 and/or Mic10) in different eukaryotic species, for example to adapt to low-oxygen environments, seems to correlate with the type of mitochondria and cristae morphology (reduced cristae or loss of cristae and the respiratory chain) (Munoz-Gomez et al., 2015; Huynen et al., 2016; Embley, 2006).

Mic19 is widespread in animals, fungi and plants pointing to the presence of Mic19 before the radiation of eukaryotes (Huynen et al., 2016). In addition, presumable orthologous genes were found, for instance, in amoebozoa (*Dictoystelium*), chromists

(*Phytoptora*) and excavates (*Naegleria*) (Huynen et al., 2016; Munoz-Gomez et al., 2015). Vertebrates possess Mic19 and Mic25, which contain a CHCH domain and show an overall sequence identity of 36% (Cavallaro, 2010; An et al., 2012). Both proteins are likely paralogues, originating from gene duplication at the root of vertebrates from an ancestral Mic19 gene (Huynen et al., 2016; Munoz-Gomez et al., 2015).

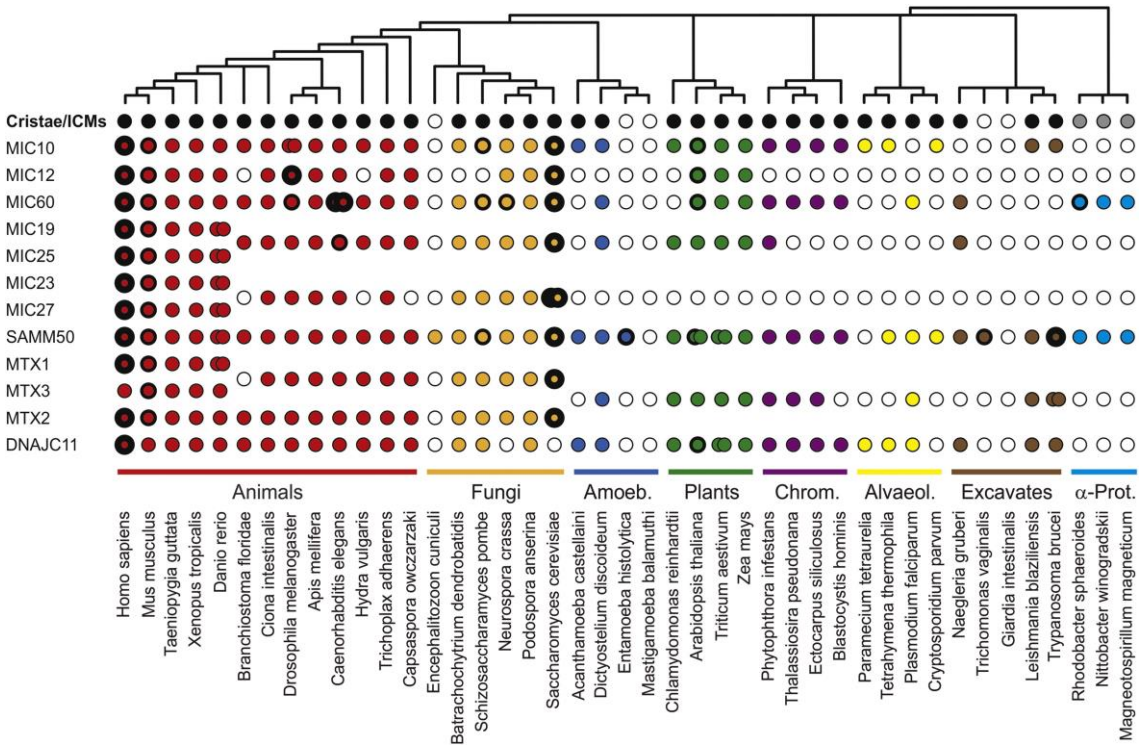

Figure 8: Phylogenetic distribution of MICOS and mitochondrial intermembrane space bridging (MIB) subunits. Eukaryotes displaying cristae are depicted in black and alphaproteobacteria (α-Prot.) with intracellular cytoplasmic membranes (ICM) are grey. The absence of an ortholog from the sequenced genome is indicated by empty circles. Colored circles show the presence of an orthologous gene, whereby thick rims denote that the protein functions in mitochondria (experimental evidence), while medium rims indicate that the protein is present in a mitochondrial or ICM fraction. The presence of two or more genes (taxon-specific duplication) is denoted by double circles. Amoeb.: Amoebozoa, Chrom.: chromists, Alvaeol.: Alveolata (from Huynen et al., 2016).

Mic12 was first described as a part of the yeast MICOS complex (Harner et al., 2011; Hoppins et al., 2011; von der Malsburg et al., 2011) with no homologs outside of fungi (Zerbes et al., 2012; Munoz-Gomez et al., 2015). Improved homology detection

identified members of the Mic12 family in metazoa, plants and algae in addition to fungi, including human Mic12 (Huynen et al., 2016). Human Mic12 is also called Mic13 or QIL1 and was described as a novel member of the human MICOS complex in 2015 (Guarani et al., 2015). Furthermore, both yeast and human orthologues were shown to be important for the connection of the MICOS subcomplexes, emphasizing their homology (Guarani et al., 2015; Anand et al., 2016; Zerbes et al., 2016). An alignment of the Mic12 family demonstrates that only the predicted transmembrane region and a WN motif, containing a predicted amphipathic helix, are conserved in sequence (Huynen et al., 2016).

Mic26 (in vertebrates also termed Mic23) and Mic27 (in *S. cerevisiae* also termed Aim37) are apolipoproteins and seem to have different functions within the MICOS complex (Bohnert et al., 2015; Zerbes et al., 2016; Rampelt et al., 2018). Vertebrata and Saccharomycetales possess both Mic26 and Mic27, while all other fungi contain only one of them (Huynen et al., 2016; Munoz-Gomez et al., 2015; Pfanner et al., 2014). Phylogenetic analysis revealed that *Saccharomyces cerevisiae* (sc) Mic27 (Aim37) is not orthologous to Mic27 of vertebrata, demonstrating that indipendent duplication of Mic26 occurred in Vertebrata and Saccharomycetales (Munoz-Gomez et al., 2015). *S. cerevisiae* Mic26 and Mic27, for example, share 17.4% sequence identity and 41.3% similarity (von der Malsburg et al., 2011). Mic26 and Mic27 seem to be the youngest MICOS components, as homologues could be only detected in metazoa and fungi (Huynen et al., 2016; Munoz-Gomez et al., 2015).

3.2.6. MICOS interaction partners

Multiple interactions of the MICOS complex with proteins of the inner and outer mitochondrial membrane, predominantly via Mic60, have been reported, including the SAM complex (Xie et al., 2007; Darshi et al., 2011; Harner et al., 2011; Darshi et al., 2012; Ott et al., 2012; Zerbes et al., 2012; Körner et al., 2012), the TOM complex (von der Malsburg et al., 2011), Mia40 (von der Malsburg et al., 2011; Varabyova et al., 2013), porin/VDAC (Hoppins et al., 2011), Ugo1 (Harner et al., 2011) and OPA1 (Darshi et al., 2011; Ding et al., 2015) (Figure 9). Interactions of MICOS with the SAM and the TOM complex seem to occur independently and are not coupled (Bohnert et al., 2012).

Furthermore, it was reported that human MICOS is able to form a large protein complex with Sam50, metaxin 1, metaxin 2, metaxin 3 and DnaJC11, which was termed mitochondrial intermembrane space bridging (MIB) complex (Ott et al., 2012; Xie et al., 2007; Huynen et al., 2016; Guarani et al., 2015; Alkhaja et al., 2012). The interaction between MICOS and the SAM complex is mediated through N-myristoylation of Mic19 and the POTRA domain of Sam50 (Darshi et al., 2011; Bohnert et al., 2012; Utsumi et al., 2018). In response to certain physiological stresses, this interaction can be disrupted by the protease OMA1 via N-terminal cleavage of Mic19 (Tang et al., 2020). In addition, deletion of Sam50 was reported to cause cristae changes as well (Ott et al., 2012).

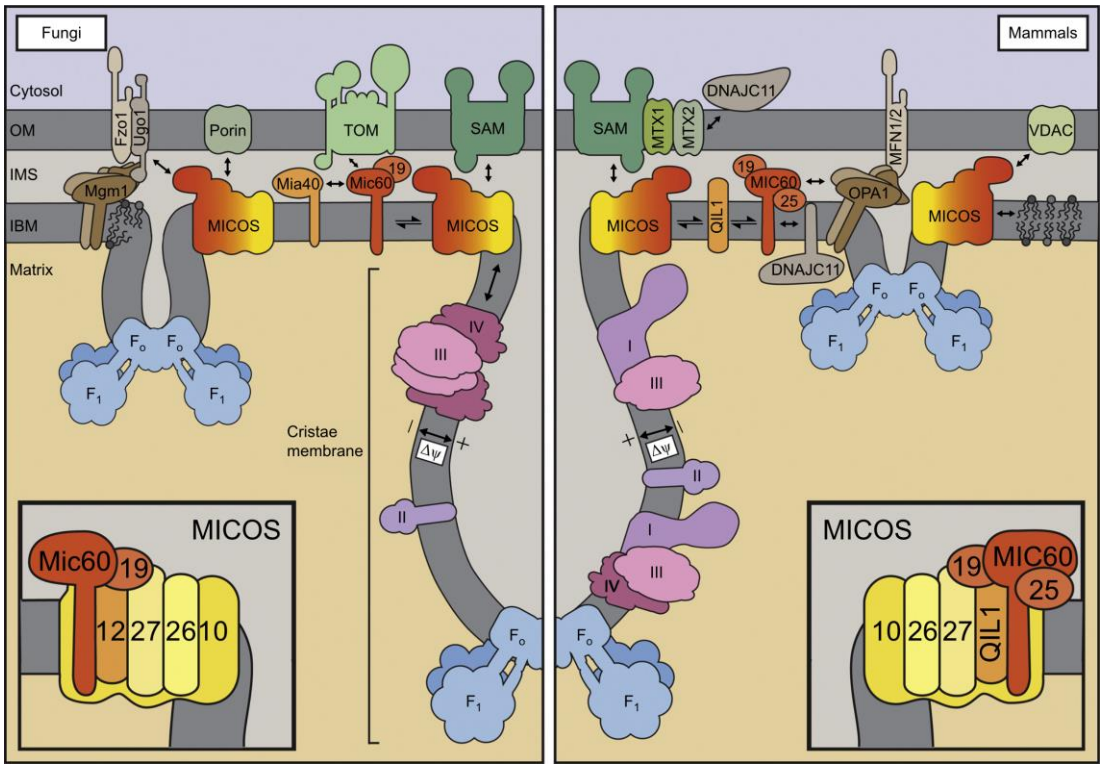

Figure 9: The MICOS network in fungal and mammalian mitochondria. Many factors are directly or indirectly involved in the development and maintenance of the typical cristae morphology, including the MICOS complex (especially the core components Mic60 and Mic10), OPA1/Mgm1, phospholipid cardiolipin (indicated by four acyl chains) and oligomeric forms of the F_1F_o-ATP synthase. MICOS is enriched at crista junctions. The Mic60 subcomplex forms contact sites with several outer membrane proteins. Components of yeast and mammalian MICOS complex are depicted at the bottom. Respiratory chain complexes (I, II, III, IV) and F_1F_o-ATP synthase dimers are enriched at cristae membranes. OM: outer mitochondrial membrane, IMS: intermembrane space, IBM: inner boundary membrane (inner mitochondrial membrane), TOM: translocase of the outer membrane, SAM: sorting and assembly machinery, MTX1/2: metaxins 1/2 (subunits of SAM), Δψ: membrane potential (from van der Laan et al., 2016).

Several studies reported interactions between F_1F_o-ATP synthase and the Mic10 subcomplex, which are necessary for F_1F_o-ATP synthase stability and oligomerization (Rampelt et al., 2017a; Alkhaja et al., 2012; Eydt et al., 2017; Anand et al., 2020). A fraction of Mic10 might also interact with F_1F_o-ATP synthase independently of the MICOS complex (Rampelt et al., 2017a).

Aim24 (Altered Inheritance of Mitochondria Protein 24) was found simultaneously with Mic12, Mic19 and Mic27 in a screen for proteins influencing mitochondrial biogenesis and inheritance (Hess et al., 2009). Subsequently, Aim24 was shown to interact with Mic10 and to be important for the integrity of the MICOS complex (Harner et al., 2014). Another relevant factor for MICOS integrity seems to be Cox17, which interacts with MICOS, and at the same time functions as a copper chaperone for the respiratory complex IV (cytochrome c oxidase) (Chojnacka et al., 2015; Horng et al., 2004).
There are several more described MICOS interaction partners, like Disrupted-in-schizophrenia 1 (DISC1) (An et al., 2012; Park et al., 2010), armadillo repeat-containing protein 1 (ArmC1) (Guarani et al., 2015; Wagner et al., 2019), and TMEM11 (Guarani et al., 2015). Their number is continuously rising, but additional experiments are necessary to unravel the molecular details and physiological roles of the interactions.

3.2.7. Diseases related to MICOS

Mitochondrial diseases are often characterized by deficiencies in cellular energy production, due to defects in oxidative phosphorylation (OXPHOS) (Niyazov et al., 2016). For example, several mutations of the OXPHOS machinery are associated with Leigh syndrome, a severe encephalopathy with respiratory difficulties (Leigh, 1951; Ruhoy and Saneto, 2014). In addition to its role in ATP production, OXPHOS complex V (F_1F_o-ATP synthase) seems to stabilize cristae membrane curvature (Paumard et al., 2002; Strauss et al., 2008).

Cristae biogenesis is poorly understood and several proteins including the MICOS complex are involved in maintenance of mitochondrial ultrastructure, as described in chapter 3.1.3. Defects in mitochondrial dynamics and altered cristae morphology are

linked to various diseases, including neurodegenerative and metabolic diseases (Zick et al., 2009).

Disruption of the MICOS complex resulted in abnormal mitochondrial ultrastructure (Figure 5), associated with impaired respiration (von der Malsburg et al., 2011; Darshi et al., 2011; Weber et al., 2013). Mic12 (also termed Mic13 or QIL1 in human) was shown to connect both MICOS subcomplexes (Guarani et al., 2015; Anand et al., 2016; Zerbes et al., 2016). Mutations in human MIC13, corresponding to a functionally null allele or abnormal and shortened splice products, lead to fatal mitochondrial encephalopathy with liver disease, including abnormal cristae morphology and defects in respiratory chain function (Guarani et al., 2016; Zeharia et al., 2016; Godiker et al., 2018).

Decreased or increased Mic60 levels were described in several diseases, emphasizing Mic60's central role in Parkinson's disease (Van Laar et al., 2008; Van Laar et al., 2018), down syndrome (Bernert et al., 2002; Myung et al., 2003), neurodegeneration (Wishart et al., 2007; Wang et al., 2008) and diabetic cardiomyopathy (Baseler et al., 2011). Altered Mic60 levels could be cause or consequence of these diseases. In diabetes mellitus, abnormal levels of Mic19 (Hwang et al., 2010) and Mic26 (Lamant et al., 2006) have been described; likewise patients suffering from acute coronary syndrome show increased Mic26 levels (Yu et al., 2012).

Human diseases are also associated with MICOS interaction partners, as dysfunction of DISC1 can cause mental illness like schizophrenia, bipolar affective disorders and recurrent major depression (St Clair et al., 1990; Brandon and Sawa, 2011; An et al., 2012; Park et al., 2010; Pinero-Martos et al., 2016). Mutations in PINK1, which phosphorylates Mic60 (Tsai et al., 2018), are linked to Parkinson's disease (Valente et al., 2004; Weihofen et al., 2009).

Perturbations in mitochondrial dynamics can lead to neuronal dysfunction (Chen and Chan, 2009). Optic atrophy, a human autosomal dominant eye-blinding disease, characterized by retinal ganglion cell degeneration (Johnston et al., 1979; Votruba et al., 1998), is associated with mutations in OPA1 (Alexander et al., 2000; Delettre et al., 2000). The dynamin-like GTPase OPA1 mediates fusion of the inner mitochondrial membrane (Praefcke and McMahon, 2004), and human OPA1 has been identified as a MICOS interaction partner (Darshi et al., 2011; Ding et al., 2015). Other proteins involved in fusion and fission of mitochondria are also linked to human diseases: for

example, fission factor dynamin-related protein 1 (DRP1) and mitofusin 2 (MFN2) (Westermann, 2010). Mutations of mitofusin 2 are found in Charcot-Marie-Tooth disease type 2A, a peripheral neuropathy (Züchner et al., 2004).
Taken together, mutation or dysfunction of mitochondrial proteins can lead to several severe or even lethal disorders, due to the diverse and tightly regulated functions of mitochondria.

3.3. Objectives of this work

Mitochondrial structure and dynamics have been intensively studied over the last years. However, the mechanisms, which lead to the formation of crista junctions and membrane remodeling, are not completely understood. The MICOS complex was shown to be crucial for mitochondrial membrane architecture and ensures that the cristae membrane remains attached to the inner boundary membrane. Several human diseases show disrupted mitochondrial dynamics and structural alterations leading to mitochondrial dysfunction and apoptosis, emphasizing the significance of mitochondrial integrity for human health. To reveal the mechanisms underlying these diseases, it is important to understand the function and regulation of proteins involved in maintenance of mitochondrial ultrastructure. Several studies have contributed comprehensive knowledge on the localization, domain architecture and function of MICOS components, but until now, no structural information about MICOS is available and details about its mechanisms have remained unclear.
The aim of this thesis was the structural and biochemical characterization of the *Chaetomium thermophilum* MICOS Mic60-Mic19 subcomplex and the determination of the mechanism by which MICOS contributes to the formation of crista junctions. To this end, the structure of a fusion construct, containing parts of the interacting C-terminal domains of Mic60 and Mic19, was obtained by X-ray crystallography. Subsequently, structure-based mutagenesis was used to biochemically analyze the interaction interface. The crystal structure of a second construct revealed additional information about the structural arrangement of the conserved C-terminal part of Mic60 and enabled insights into the question how Mic60 binds and remodels mitochondrial membranes.

4. Materials and Methods

4.1. Materials

4.1.1. Instruments

ÄKTApurifier chromatography systems HiLoad 16/600 Superdex 75 pg column HiLoad 16/600 Superdex 200 pg column Superdex 75 10/300 GL column	GE Healthcare Life Sciences (Chicago, USA) now Cytiva
1290 Infinity II LC System 6230B LC/MS TOF system	Agilent Technologies, Inc. (Santa Clara, USA)
MicroCal PEAQ-ITC Viscotek 270 dual detector Viscotek VE 3580 refractive index detector	Malvern Panalytical GmbH (Malvern, United Kingdom)
M-110L Microfluidizer	Microfluidics (Westwood, USA)
Biophotometer 6131 NanoDrop One spectrophotometer NanoDrop 2000 spectrophotometer	Eppendorf AG (Hamburg, Germany) Thermo Fisher Scientific Inc. (Waltham, USA)
Avanti® J-26XP centrifuge J-LITE® JLA-8.1000 rotor	Beckman Coulter Inc. (Brea, USA)
Optima™ L-100K Ultracentrifuge Type 45 Ti rotor	Beckman Coulter Inc. (Brea, USA)
Optima™ Max-XP Tabletop Ultracentrifuge TLA-100 Fixed-Angle Rotor	Beckman Coulter Inc. (Brea, USA)
Centrifuge 5810 R Centrifuge 5424 R	Eppendorf AG (Hamburg, Germany) Eppendorf AG (Hamburg, Germany)
Crystal Gryphon	ARI - Art Robbins Instruments (Sunnyvale, USA)
FORMULATOR® liquid dispensing system Rock Imager® 1000 protein crystallization imager and storage system	FORMULATRIX (Bedford, USA) FORMULATRIX (Bedford, USA)

B 6120 incubator	Heraeus (Hanau, Germany)
New Brunswick™ Excella® E24	Eppendorf AG (Hamburg, Germany)
New Brunswick™ Innova® 44	Eppendorf AG (Hamburg, Germany)
MHR 13 heating thermoshaker	Hettich Benelux (Geldermalsen, NL)
C1000 Touch™ Thermal Cycler	Bio-Rad Laboratories, Inc. (Hercules, USA)
Leica WILD M3C stereo microscope	Leica Microsystems (Wetzlar, Germany)
Leica UC7 ultramicrotome	Leica Microsystems (Wetzlar, Germany)
Zeiss transmission electron microscope	Carl Zeiss AG (Oberkochen, Germany)
EM910 and 11M Quemesa CCD camera	Carl Zeiss AG (Oberkochen, Germany)
Biometra Compact XS/S	Analytik Jena GmbH (Jena, Germany)
PowerPac™ 300 Basic Power Supply	Bio-Rad Laboratories, Inc. (Hercules, USA)
Gel Doc™ XR+ Gel Documentation System	
XCell SureLock Mini-Cell Electrophoresis System	Thermo Fisher Scientific Inc. (Waltham, USA)
VWR™ Power Source™ 300V	VWR International, LLC (Radnor, USA)
LPC-213 precision balance	
Eppendorf Research® plus pipette	Eppendorf AG (Hamburg, Germany)
Gilson™ PIPETMAN Classic™	Gilson Inc. (Middleton, USA)
Milli-Q® Direct Water Purification System	Merck KGaA (Darmstadt, Germany)
FiveEasy pH meter	Mettler-Toledo (Greifensee, CHE)
Magnetic stirrers RCT/RH basic	IKA®-Werke GmbH & Co. KG (Staufen, Germany)
Diaphragm vacuum pump type MD 4C	VACUUBRAND GMBH + CO KG (Wertheim, Germany)
Desiccator DURAN®	DWK Life Sciences (Wertheim, Germany)
Peristaltic pump REGLO *Analog*	Ismatec, Cole-Parmer GmbH (Wertheim, Germany)
Chromatography Column Econo-Pac®	Bio-Rad Laboratories, Inc. (Hercules, USA)

4.1.2. Chemicals

Chemicals were purchased from the following companies: Carl Roth GmbH + Co. KG (Karlsruhe, Germany), Sigma-Aldrich (St. Louis, Missouri, USA), Merck KGaA (Darmstadt, Germany), AppliChem GmbH (Darmstadt, Germany), Bioline, Meridian Bioscience (Cincinnati, Ohio, USA), Fisher Scientific GmbH (Schwerte, Germany), Melford Laboratories Ltd. (Ipswich, United Kingdom), SERVA Electrophoresis GmbH (Heidelberg, Germany), Th. Geyer GmbH & Co. KG (Renningen, Germany). The list is given in Appendix B.

4.1.3. Enzymes

*Bam*HI-HF (G↓G A T C C)	New England Biolabs Inc. (Ipswich, USA)
CIP (Alkaline Phosphatase, Calf Intestinal)	New England Biolabs Inc. (Ipswich, USA)
Quick CIP	New England Biolabs Inc. (Ipswich, USA)
DNase I (grade II, from bovine pancreas)	Roche Diagnostics GmbH (Mannheim, Germany)
*Dpn*I	New England Biolabs Inc. (Ipswich, USA)
HRV-3C protease (His-tagged)	Produced in-house
Phusion® High-Fidelity DNA Polymerase	New England Biolabs Inc. (Ipswich, USA)
Pfu DNA polymerase	Roboklon (Berlin, Germany)
T4 DNA Ligase	New England Biolabs Inc. (Ipswich, USA)
T4 Polynucleotide Kinase	New England Biolabs Inc. (Ipswich, USA)
Trypsin (from bovine pancreas)	Sigma-Aldrich (St. Louis, USA)
*Xho*I (C↓T C G A G)	New England Biolabs Inc. (Ipswich, USA)

4.1.4. Kits and consumables

innuPREP Plasmid Mini Kit 2.0	Analytik Jena GmbH (Jena, Germany)
QIAquick Gel Extraction Kit	Qiagen (Hilden, Germany)
2-Log DNA Ladder	New England Biolabs Inc. (Ipswich, USA)
1 kb Plus DNA Ladder	New England Biolabs Inc. (Ipswich, USA)

Additive Screen JBScreen Plus HTS	Jena Bioscience GmbH (Jena, Germany)
Additive Screen Silver Bullets HR2-096	Hampton Research (Aliso Viejo, USA)
Amicon® Ultra-15 Centrifugal Filter Units (3 kDa, 10 kDa, 30 kDa MWCO)	Merck KGaA (Darmstadt, Germany)
Circular Cover Slides, siliconized, 22 mm thick	Jena Bioscience GmbH (Jena, Germany)
Classics II Suite, pH Clear Suite, Protein Complex Suite	Qiagen (Hilden, Germany)
CrystalQuick™ LP Plates, 96 Well (609171)	Greiner Bio-One GmbH (Frickenhausen, Germany)
Glass vials (C4013-1)	Thermo Fisher Scientific Inc. (Waltham, USA)
JBScreen JCSG++ HTS, Basic HTS	Jena Bioscience (Jena, Germany)
Morpheus Screen	Molecular Dimensions Limited (Sheffield, UK)
Mounted CryoLoop™ - 20 micron (0.05-0.1 mm, 0.1-0.2 mm loops)	Hampton Research (Aliso Viejo, USA)
NativePAGE™ 4 to 16%, Bis-Tris, protein gels, 10 well NativePAGE™ Cathode Buffer Additive (20X) NativePAGE™ Running Buffer (20X) NativePAGE™ Sample Buffer (4X) NativeMark™ Unstained Protein Standard	Invitrogen™, Thermo Fisher Scientific Inc. (Waltham, USA)
NuPAGE™ 4-12% Bis-Tris protein gels, 10 well and 15 well NuPAGE™ MES and MOPS SDS Running Buffer (20X)	Invitrogen™, Thermo Fisher Scientific Inc. (Waltham, USA)
Ni Sepharose High Performance	GE Healthcare Bio-Sciences AB (Uppsala, Sweden)
PageRuler™ Plus Prestained Protein Ladder	Thermo Fisher Scientific Inc. (Waltham, USA)
Pierce™ Unstained Protein MW Marker	Thermo Fisher Scientific Inc. (Waltham, USA)
Seed Bead™ HR2-320	Hampton Research (Aliso Viejo, USA)
VDX™ Plate with sealant (24 well)	Hampton Research (Aliso Viejo, USA)
Whatman™ Sterile Mixed Cellulose Ester Membranes, d = 47 mm, pore size: 0.2 µm or 0.45 µm	GE Healthcare Life Sciences (Chicago, USA) now Cytiva
ZelluTrans/Roth dialysis membrane 12K and 3.5K MWCO	Carl Roth GmbH + Co. KG (Karlsruhe, Germany)

4.1.5. Plasmids

pETDuet™-1

5420 bp, ampicillin resistance, two multiple cloning sites, N-terminal His_6-tag, C-terminal S-tag (Novagen, Merck KGaA, Darmstadt, Germany)

pSKB_LNB, modified pET28a(+)

5345 bp, kanamycin resistance, N-terminal His_6-tag, HRV-3C protease cleavage site, recognition sequences: *Apa*I, *Nde*I, *Bam*HI, *Eco*RI, *Sac*I, *Sal*I, *Hind*III, *Not*I, *Xho*I (Novagen, Merck KGaA, Darmstadt, Germany; cloned by D. Kühlmann, MPI Dortmund)

4.1.6. Bacteria strains

E. coli BL21(DE3)	Competent cells produced in-house (Novagen)
E. coli DH5α	Competent cells produced in-house (gift from Stephen Marino)

4.1.7. Buffers

Lysis buffer	50 mM HEPES, pH 7.5, 500 mM NaCl, 20 mM imidazole
Elution buffer	50 mM HEPES, pH 7.5, 500 mM NaCl, 300 mM imidazole
Dialysis buffer	50 mM HEPES, pH 7.5, 500 mM NaCl
SEC buffer	20 mM HEPES, pH 7.5, 150 mM NaCl
TAE buffer	40 mM Tris, 20 mM acetic acid, 1 mM EDTA
TBE buffer	89 mM Tris, pH 8, 89 mM boric acid, 2.5 mM EDTA

pH was adjusted using NaOH or HCl.

CutSmart® Buffer	New England Biolabs Inc. (Ipswich, USA)
Phusion® HF Buffer	New England Biolabs Inc. (Ipswich, USA)
Pfu Buffer	Roboklon (Berlin, Germany)
T4 DNA Ligase Buffer	New England Biolabs Inc. (Ipswich, USA)

4.1.8. Media and antibiotics

LB medium: 10 g/l tryptone/peptone, 10 g/l NaCl, 5 g/l yeast extract, pH 7 (NaOH)
for LB Agar plates: mix LB medium and 15 g/l agar agar

TB medium: 12 g/l casein digest peptone, 24 g/l yeast extract, 9.4 g/l K_2HPO_4, 2.2 g/l KH_2PO_4 (Terrific Broth, granulated), 4 ml/l glycerol

Ampicillin: 100 mg/ml in ddH_2O, working solution 100 µg/ml

Carbenicillin: 100 mg/ml in ddH_2O, working solution 100 µg/ml

Kanamycin: 50 mg/ml in ddH_2O, working solution 50 µg/ml

4.2. Molecular biology methods

4.2.1. Polymerase chain reaction (PCR)

Amplification of DNA fragments was performed using Phusion® High-Fidelity DNA Polymerase (New England Biolabs Inc.) according to manufacturer's instructions. The composition of the PCR reaction and the program are detailed in Table 2 and Table 3, respectively. Amplified DNA fragments were separated by agarose gel electrophoresis. Fusion constructs were generated using overlap extension PCR running two separate PCRs. For this, DNA bands were excised from agarose gels, purified (see 4.2.3.), combined and amplified by PCR (Ho et al., 1989; Reddy Chichili et al., 2013).

Table 2: **Reaction solution composition for PCR using Phusion® High-Fidelity DNA Polymerase.**

Volume	Component	Final concentration
8.0 µl	5x HF buffer for Phusion	1×
4.0 µl	dNTPs (2 mM)	0.2 mM
1.2 µl	DMSO	3%
2.0 µl	5' primer (10 µM)	0.5 µM
2.0 µl	3' primer (10 µM)	0.5 µM
1.0 µl	DNA template (50 ng/µl)	50 ng/40 µl
0.4 µl	Phusion HF DNA Polymerase (2 U/µl)	0.8 U/40 µl
21.4 µl	ddH_2O (ad 40 µl)	

Table 3: **PCR program for Phusion® High-Fidelity DNA Polymerase.**

Process	Temperature	Time	Cycles
Initialization	98°C	30 s	1
Denaturation	98°C	10 s	
Annealing	50-72°C	20 s	35
Extension	72°C	15-30 s/1000 bp	
Extension	72°C	10 min	1

4.2.2. Agarose gel electrophoresis

Agarose gels were prepared and run according to the standard procedures (Sambrook et al., 1989) using 1x TBE buffer or 1x TAE buffer and 0.3 µg/ml ethidium bromide. DNA fragments or plasmids were visualized by UV light and excised from the gel.

4.2.3. DNA purification

DNA bands, excised from agarose gels, or digested DNA, was purified using QIAquick Gel Extraction Kit (Qiagen) according to the manufacturer's protocol. Elution was performed with 30-50 µl ddH_2O.

4.2.4. DNA digestion

Amplified DNA fragments were digested at 37 °C for 1-2 h with restriction enzymes *Bam*HI-HF and *Xho*I (New England Biolabs Inc.) in CutSmart® Buffer according to manufacturer's protocol. Vectors were digested similarly, but the digestion mix was supplemented with CIP or Quick CIP (both New England Biolabs Inc.) to carry out digestion and dephosphorylation simultaneously. Digested vectors and DNA fragments were purified using QIAquick Gel Extraction Kit (Qiagen) according to the manufacturer's protocol. Subsequently, DNA fragments were treated with T4 Polynucleotide Kinase (New England Biolabs Inc.) according to manufacturer's protocol to add 5´-phosphates. In variation from this, T4 ligase buffer was used instead

of PNK buffer and ATP. DNA fragments were again purified with QIAquick Gel Extraction Kit (Qiagen) and eluted using 30 µl ddH_2O.

4.2.5. DNA ligation

After digestion, vector and DNA insert were ligated at room temperature for 2-3 h using T4 DNA Ligase (New England Biolabs Inc.) according to manufacturer's protocol. Ligations were performed using a molar ratio of approx. 1:7 vector to insert and *NEBioCalculator* (Online tool, New England Biolabs Inc.) was used to calculate molar ratios.

4.2.6. Transformation

Transformation of *E. coli* cells was carried out using the heat shock method. After ligation or *Dpn*I digestion (4.2.9.), DNA (5-10 µl) was transformed in *E. coli* DH5α or *E. coli* BL21(DE3). For protein expression, isolated plasmids (1-20 ng) were transformed in *E. coli* BL21(DE3). DNA and chemically competent cells were mixed and incubated for 10 min on ice, followed by a heat shock at 42 °C for 45 s. After 5 min incubation on ice and addition of 200 µl LB medium, the cell suspension was incubated for 1 h at 37 °C and 800 rpm. Subsequently, cells were centrifuged at 1000 x g for 2 min, resuspended in 70 µl LB medium and plated on LB agar plates containing the required antibiotic.

4.2.7. Preparation of chemically competent *E. coli* cells

200 ml LB medium was inoculated with 1 ml overnight-culture and grown at 37 °C until an OD_{600} of 0.6 to 0.8. Afterwards, the bacteria suspension was transferred to two 50 ml falcon tubes, incubated for 10 min on ice and centrifuged for 10 min at 2500 x g (4 °C). Cells were resuspended in 10 ml ice-cold 0.1 M $CaCl_2$/10% glycerol and incubated 15 min on ice. After a second centrifugation step (10 min, 2500 x g, 4 °C), the cells were resuspended in 1 ml ice-cold 0.1 M $CaCl_2$/10% glycerol and aliquots were stored at -80 °C (flash-frozen in liquid nitrogen).

4.2.8. Bacteria storage

Bacterial overnight cultures were supplemented with glycerol to 28% (v/v) and stored at -80 °C.

4.2.9. Site-directed mutagenesis

Site-directed mutagenesis was used to generate single-point mutations. For this, the whole plasmid was amplified via PCR using Pfu DNA polymerase (Roboklon) and primers containing the desired mutation. The composition of the reaction mix and the PCR program are detailed in Table 4 and Table 5, respectively. Subsequently, the PCR reaction was incubated with *Dpn*I (1 U/20 µl; New England Biolabs Inc.) for 1-2 h at 37 °C to digest the methylated template, and transformed in *E. coli* DH5α or *E. coli* BL21(DE3).

Table 4: **Reaction mixture for site-directed mutagenesis using Pfu DNA polymerase.**

Volume	Component	Final concentration
2.0 µl	10x Pfu buffer	1×
4.0 µl	dNTPs (2 mM)	0.4 mM
2.0 µl	5’ primer (10 µM)	1.0 µM
2.0 µl	3’ primer (10 µM)	1.0 µM
1.0 µl	DNA template (25-50 ng/µl)	25-50 ng/20 µl
0.5 µl	Pfu (5 U/µl)	2.5 U/20 µl
8.5 µl	ddH_2O (ad 20 µl)	

Table 5: **PCR program for site-directed mutagenesis with Pfu DNA polymerase.**

Process	Temperature	Time	Cycles
Initialization	95 °C	5 min	1
Denaturation	95 °C	30 s	18
Annealing	53-68 °C	1 min	
Extension	68 °C	2 min/1000 bp	
Extension	68 °C	10 min	1

4.2.10. Isolation of plasmid DNA

Isolation of plasmid DNA (from bacterial lysates) was performed using innuPREP Plasmid Mini Kit 2.0 (Analytik Jena GmbH) according to the manufacturer's protocol. In variation from this, elution was carried out with 30-50 µl ddH_2O.

4.2.11. DNA sequencing

Sequencing of isolated DNA was done by LGC Genomics GmbH (Berlin) or Source BioScience (Berlin) by means of Sanger sequencing. To analyze sequenced DNA, sequences were aligned using *MultAlin* (Corpet, 1988).

4.2.12. Constructs

Genes coding for *Chaetomium thermophilum* Mic60 (UniProtID: G0SHY5) and Mic19 (UniProtID: G0S140) were codon-optimized for *E. coli* and synthesized by Eurofins Genomics (Germany) and have been provided by Manuel Hessenberger (M.H.). The constructs used in this thesis are listed in Table 6. All constructs were expressed with a HRV-3C protease-cleavable, N-terminal His_6-tag. The HRV-3C cleavage site was introduced via the forward primer if constructs were cloned into pETDuet-1 vector (MGSSHHHHHHSQDPLEVLFQGP).

Table 6: **Used constructs.** Constructs labelled with M.H. have been provided by Manuel Hessenberger.

Construct	Remark	Vector
Mic60_208-691	$Mic60_{sol}$, provided by M.H.	pSKB_LNB
Mic60_208-691_Q674A	$Mic60_{sol}$_Q674A	pSKB_LNB
Mic60_208-691_V678D	$Mic60_{sol}$_V678D	pSKB_LNB
Mic60_208-691_L685D	$Mic60_{sol}$_L685D	pSKB_LNB
Mic60_208-691_R574D/R575D	$Mic60_{sol}$_R574D/R575D	pSKB_LNB
Mic60_208-691_R581D/K582D	$Mic60_{sol}$_R581D/K582D	pSKB_LNB
Mic60_208-691_R631D	$Mic60_{sol}$_R631D	pSKB_LNB
Mic19_1-164	Mic19, provided by M.H.	pSKB_LNB
Mic19_1-164_R126A	Mic19_R126A	pSKB_LNB
Mic19_1-164_V129D	Mic19_V129D	pSKB_LNB
Mic19_1-164_L133D	Mic19_L133D	pSKB_LNB
Mic19_1-164_F150D	Mic19_F150D	pSKB_LNB
Mic60_623-691-GSGS-Mic19_116-164	Provided by M.H.	pSKB_LNB
Mic60_624-691-GSGS-Mic19_116-164	Mitofilin_C-CHCH	pETDuet-1
Mic60_565-586-622-691-GSGS-Mic19_116-164	Mitofilin-CHCH_1	pETDuet-1
Mic60_565-586-GS-622-691-GSGS-Mic19_116-164	Mitofilin-CHCH_2	pETDuet-1
Mitofilin-CHCH_2_W662D	Mitofilin-CHCH_2_W662D	pETDuet-1
Mitofilin-CHCH_2_V666D	Mitofilin-CHCH_2_V666D	pETDuet-1
Mitofilin-CHCH_2_L676D	Mitofilin-CHCH_2_L676D	pETDuet-1
Mic60_565-586-GSGS-622-691-GSGS-Mic19_116-164	Mitofilin-CHCH_3	pETDuet-1
Mic60_565-607-622-691-GSGS-Mic19_116-164	Mitofilin-CHCH_4	pETDuet-1
Mic60_565-607-GS-622-691-GSGS-Mic19_116-164	Mitofilin-CHCH_5	pETDuet-1
Mic60_565-607-GSGS-622-691-GSGS-Mic19_116-164	Mitofilin-CHCH_6	pETDuet-1
Mic60_565-691-GSGS-Mic19_116-164	Mitofilin-CHCH_7	pETDuet-1

4.3. Biochemical methods

4.3.1. Sequence alignment

To analyze conservation, sequences were aligned using *Clustal Omega* (Sievers et al., 2011) and manually refined.

4.3.2. SDS-PAGE

Separation of proteins of different molecular weight (MW) was performed via denaturing sodium dodecyl sulfate polyacrylamide gel electrophoresis (SDS-PAGE) using NuPAGE™ 4-12% Bis-Tris protein gels (Invitrogen™, Thermo Fisher Scientific Inc.) and MES or MOPS running buffer. Samples were prepared by mixing with sample buffer (50 mM Tris-HCl pH 6.8, 2% (w/v) SDS, 10% glycerol, 1% β-mercaptoethanol, 0.02% (w/v) bromophenol blue) and 5 min incubation at 95 °C. Gels were stained with Coomassie Brilliant Blue R-250 (45% ethanol, 10% acetic acid, 0.3% (w/v) Coomassie Brilliant Blue R-250). Destaining solution contained 45% ethanol, 10% acetic acid.

4.3.3. Blue native PAGE

Blue native PAGE was done with NativePAGE™ 4-16% Bis-Tris protein gels (10 well, Invitrogen™) according to NativePAGE™ Bis-Tris Gel protocol 2013 (Thermo Fisher Scientific Inc.). 5 µg protein was applied to the gel. To analyze Mic60-Mic19 complex formation and oligomerization, 5 µg Mic60 and 2 µg Mic19 were incubated for 15 min and subsequently applied to the gel.

4.3.4. Protein over-expression in *E. coli*

Protein over-expression was performed by transformation of *E. coli* BL21(DE3) with the isolated plasmid. 50 ml LB pre-culture, containing the respective antibiotics, was grown overnight at 37 °C and 180 rpm. The next day, 10 ml of the pre-culture was used to inoculate 1 l TB medium (with antibiotics) and cells were grown to an OD_{600} of 0.6 - 0.8

at 37 °C under shaking conditions (80 rpm). Protein expression was induced by addition of 200 µM isopropyl β-D-1-thiogalactopyranoside (IPTG; Carl Roth GmbH + Co. KG). Then temperature was shifted to 18 °C and cultures were grown for another 18 h. Bacteria were pelleted at 4000 x g for 20 min, resuspended in 30 ml lysis buffer (50 mM HEPES, pH 7.5, 500 mM NaCl, 20 mM imidazole) and stored at -20 °C.

4.3.5. Cell disruption

Cells were thawed on ice, and 0.02 mg/ml DNase I (Roche) and a spade point protease inhibitor AEBSF Hydrochloride BioChemica (Panreac AppliChem) were added to the resuspended pellet (in 30 ml 50 mM HEPES, pH 7.5, 500 mM NaCl, 20 mM imidazole). The bacteria suspension was passed twice through a fluidizer and insoluble material was removed by centrifuging at 100,000 x g for 45 min (4 °C). The supernatant was filtered (0.45 µm) and used for further purification.

4.3.6. Protein purification

His-tagged proteins were purified using immobilized metal ion affinity chromatography (IMAC) and size-exclusion chromatography (SEC) at 4 °C.

The filtered supernatant (see 4.3.5.) was applied onto a 3 ml packed Ni Sepharose High Performance (GE Healthcare) chromatography column (Econo-Pac® Chromatography Columns, Bio-Rad), equilibrated with lysis buffer (50 mM HEPES, pH 7.5, 500 mM NaCl, 20 mM imidazole), using a peristaltic pump with a constant flow of 1 ml/min. To remove unspecifically bound proteins, the column was washed twice with six column volumes of lysis buffer containing low imidazole concentration (20 mM). Bound proteins were eluted with approx. 15 ml elution buffer (50 mM HEPES, pH 7.5, 500 mM NaCl, 300 mM imidazole) and dialyzed overnight at 4 °C against dialysis buffer (50 mM HEPES, pH 7.5, 500 mM NaCl) in the presence of His-tagged HRV-3C protease (1:50) to cleave the N-terminal His_6-tag. After protein elution, the column material was washed with 1 M imidazole and H_2O (10-15 column volumes each) and equilibrated with lysis buffer again.

The next day, the dialyzed protein sample was re-applied to the Ni-NTA column (equilibrated with lysis buffer) to separate cleaved from non-cleaved proteins. Cleaved

protein was collected during loading of dialysis solution and/or eluted with 20 ml lysis buffer. Fractions containing untagged protein were pooled and concentrated to final concentrations of 10-30 mg/ml, if possible.
Finally, protein was purified using an ÄKTApurifier chromatography system (GE Healthcare) at 4°C, connected to a Superdex 75 or Superdex 200 column equilibrated in SEC buffer (20 mM HEPES, pH 7.5, 150 mM NaCl). 1 ml fractions were collected and peak fractions, containing the protein of interest, were pooled, concentrated, flash-frozen in liquid nitrogen and stored at -80°C.
All fractions collected during the protein purification were analyzed using SDS-PAGE. Stripping and recharging of Ni Sepharose High Performance (GE Healthcare) was performed according to the manufacturer's protocol.

4.3.7. Protein concentration

Protein solutions were concentrated using Amicon® Ultra 15 mL Centrifugal Filters (Merck Millipore) with appropriate cutoffs. Subsequently, protein concentrations were determined using NanoDrop One or NanoDrop 2000 spectrophotometer (Thermo Scientific). Molecular weights and extinction coefficients were calculated with ProtParam, ExPASy Server (Gasteiger et al., 2005).

4.3.8. Mass spectrometry

Mass spectrometry analysis was performed using liquid chromatography-electrospray ionization-quadrupole-time of flight-mass spectrometry (LC-ESI-Q-TOF-MS) at the Protein Production & Characterization Platform at the Max-Delbrück-Centrum (MDC), supported by Anja Schütz.
Protein intact mass analyses were conducted on an Agilent 1290 Infinity II UHPLC system coupled to an Agilent 6230B time-of-flight (TOF) LC/MS instrument equipped with an AJS (Agilent Jet Stream Technology) ion source operated in positive ion mode (denaturing conditions). Protein samples were desalted using a Zorbax 300SB-C3 guard column (2.1 × 12.5 mm, 5 µm). Protein solutions were diluted in 0.1% formic acid (in H_2O) to approx. 0.06 mg/ml (estimated for Mitofilin_C-CHCH after trypsin digestion). Approximately 0.3 µg of sample was injected for each analysis. LC/MS parameters

were adapted from Chalk, 2017. The ion source was operated with the capillary voltage at 4000 V, nebulizer pressure at 50 psi, drying and sheath gas at 350 °C, and drying and sheath gas flow rate at 12 and 11 l/min, respectively. The instrument ion optic voltages were as follows: fragmentor 250 V, skimmer 65 V, and octopole RF 750 V. Mass spectrometry data were analyzed using the Protein Deconvolution feature of the MassHunter BioConfirm Version 10.0 software (Agilent) that uses the Maximum Entropy algorithm for accurate molecular mass calculation. Deconvolution was performed between mass range of 800 to 2,500 m/z (mass-to-charge ratio), using peaks with a ratio of signal to noise greater than 30:1. The deconvoluted mass range was set at 5 to 25 kDa and the step mass was 1 Da.

4.3.9. Right-angle light scattering (RALS)

Size exclusion chromatography coupled to right-angle light scattering (SEC-RALS) was carried out using an ÄKTApurifier chromatography system (GE Healthcare) at 4 °C, coupled to a RALS-refractive index detector (Malvern). 100 µl of a 3 mg/ml protein solution were applied on a Superdex 75 10/300 column (GE Healthcare). The running buffer contained 20 mM HEPES, pH 7.5, 150 mM NaCl, and a flow rate of 0.5 ml/min was used. Data were analyzed with OmniSec software v5.00 (Malvern).

4.3.10. Isothermal titration calorimetry (ITC)

ITC experiments were performed at 10 °C using a MicroCal PEAQ-ITC system (Malvern) according to the manufacturer's protocol, using the standard program with 13 injections (DP = 10 µcal/s). Proteins were dialyzed against SEC buffer (20 mM HEPES, pH 7.5, 150 mM NaCl) overnight at 4 °C prior to ITC experiments. Mic60 constructs were placed in the sample cell (44 µM – 50 µM) and Mic19 constructs in the syringe (391 µM - 809 µM). Protein concentrations were adapted to the respective reaction. MicroCal PEAQ-ITC Analysis Software (Malvern) was used to analyze the data and calculate binding parameters.

4.3.11. Limited proteolysis

Mitofilin_C-CHCH was partially digested, using trypsin from bovine pancreas (Sigma-Aldrich) dissolved in 1 mM HCl and 2 mM $CaCl_2$ (1 mg/ml stock concentration). In test experiments, the protein was supplemented with 1% trypsin (w/w) and incubated at room temperature (approx. 20 °C) for 90 min. Samples were taken every 10 min, starting with 20 min, and analyzed by SDS-PAGE. Prior to mass spectrometry, Mitofilin_C-CHCH was incubated with 3% (w/w) trypsin for 5 h or overnight at room temperature. In crystallization trials, Mitofilin_C-CHCH was mixed with 0.1% or 1% trypsin (w/w) and incubated for 10 min at 4 °C (see 4.4.1.).

4.3.12. Folch liposome preparation

For Folch liposome preparation, 3 ml chloroform was mixed with 0.9 ml methanol. 100 µl of this mixture was filled into a glass tube and 500 µg lipids (Brain extract from bovine brain, type I, Folch fraction I, Sigma-Aldrich) were added. Lipids were dried under argon stream and stored overnight in an exhausted desiccator. Subsequently, dried lipids were dissolved in 333 µl SEC buffer (20 mM HEPES, pH 7.5, 150 mM NaCl) to a final concentration of 1.5 mg/ml. After overnight-incubation at 4°C, the glass tube was sonicated for 15 min in an ultrasonic bath to obtain unilamellar liposomes (see also https://www2.mrc-lmb.cam.ac.uk/groups/hmm/techniqs/Liposome.html).
Tobias Bock-Bierbaum (MDC) optimized $Mic60_{sol}$ binding to liposomes and observed the highest binding level if liposomes were incubated for 15 min in the ultrasonic bath.

4.3.13. Liposome co-sedimentation assay

5 µM purified protein (or 5 µM Mic60 and 5 µM Mic19) was incubated with 0.6 mg/ml prepared liposomes (see 4.3.12.) for 30 min at room temperature in 40 µl reaction volume (filled with SEC buffer). After centrifugation at 200,000 × g for 16 min at 20 °C, pellet and supernatant fractions were analyzed via SDS-PAGE. Quantification was done using *ImageJ* (Version 1.50i; Schneider et al., 2012). Control experiments were performed without liposomes. The standard deviations were calculated based on the entire population given as arguments.

4.3.14. Yeast strains and plasmids

Cloning of yeast constructs, and protein level analyses were performed by Florian Wollweber, Janina Laborenz and Sibylle Jungbluth (Universität des Saarlandes, 66421 Homburg). *Saccharomyces cerevisiae* strains used in this study are derivates of YPH499 (Sikorski and Hieter, 1989), and yeast expression plasmids are derived from pRS426-Mic60 and pRS426-Mic19 (Bohnert et al., 2015). The inserts, including the open reading frames, as well as the up- and downstream regions were cloned into the centromeric plasmid pRS416. Mutations were introduced by site-directed mutagenesis. Plasmids were then transformed into YPH499 *mic60*Δ or *mic19*Δ (von der Malsburg et al., 2011).

For analysis of protein levels, yeast were grown to mid-logarithmic phase in defined minimal (-URA) medium containing 3% (v/v) glycerol as carbon source and mitochondria were isolated at a small scale (Faelber et al., 2019) by differential centrifugation. Protein levels were determined by Bradford assay, equal amounts of mitochondria were solubilized in Laemmli buffer and incubated at 65 °C for 10 min. Subsequently, samples were analyzed by SDS-PAGE and Western blotting with polyclonal antibodies against MICOS subunits, and Atp2 as sample processing control.

4.3.15. Electron microscopy of yeast mitochondria

The following protocol was performed by Elisa Lisicki at the MDC, supported by the Electron Microscopy Technology Platform of MDC (Séverine Kunz, Bettina Purfürst, Christina Schiel).

Yeast cells were grown in SD-Ura medium lacking uracil (0.67% (w/v) yeast nitrogen base without amino acids (BD Difco), 0.07% (w/v) CSM-URA amino acid mixture without uracil (MP Biomedicals)) mixed with 2% (w/v) glucose for 24 h at 30 °C. After dilution in SD-Ura medium supplemented with 3% (w/v) glycerol, cells were grown overnight (until the early log phase). Sample preparation was performed as previously described (Slot and Geuze, 2007) and stained using the Tokuyasu method (Tokuyasu, 1973). Yeast cells were fixed for 3 h with 4% (w/v) paraformaldehyde and 0.5% (v/v) GA in 0.1 M citrate buffer (freshly prepared, pH and temperature adjusted to growth conditions) and washed with 0.1 M citrate buffer. The cells were treated with 1% (w/v) sodium metaperiodate for 1 h at 4 °C to permeabilize, and washed with 0.1 M

phosphate buffer. Subsequently, yeast cells were embedded in 12% (w/v) gelatin (10 min incubation at 37 °C, followed by centrifugation of the yeast cells at 3000 x g for 3 min and cooling the warm gelatin in ice). Samples of 1 mm^3 were cut, infiltrated with 2.3 M sucrose overnight and frozen in liquid nitrogen.

Ultrathin sections were cut at -110 °C (UC7 ultramicrotome, Leica) and collected on formvar/carbon-coated copper grids (Plano). Sections were stained with 3% (w/v) tungstosilicic acid hydrate in 2.8% (w/v) polyvinyl alcohol (Sigma-Aldrich) (Kärgel et al., 1996) followed by washing with phosphate buffered saline at 37 °C and water to remove the gelatin. Dried grids were imaged with an EM910 transmission electron microscope (Zeiss) at 80 kV and acquisition was done on a Quemesa CCD camera with the iTEM software (Emsis) at 10,000 x magnification.

All data are presented as the mean together with the standard deviation and value differences were compared statistically. Data analysis and plotting was carried out using the statistic program R. Normal distribution was tested using Kolmogorov-Smirnov test as well as the Q-Q plot.

The two-sided Wilcoxon-Rank-sum test for independent samples with continuity correction was used, as data were not normal distributed. n = 100 mitochondrial cross sections were analyzed for all groups. Differences of $p \leq 0.05$ were considered significant ($p \leq 0.05$*, $p \leq 0.01$**, $p \leq 0.001$***) and the test statistic W is reported.

4.3.16. Analytical ultracentrifugation (AUC)

Analytical ultracentrifugation (AUC) experiments were performed by Dr. Hauke Lilie at the Martin-Luther-Universität Halle-Wittenberg using my purified proteins.

The measurements were performed in 20 mM HEPES, pH 7.5, 150 mM NaCl at 20 °C using a Beckman Optima XL-I centrifuge and an An50Ti rotor equipped with double sector cells. Sedimentation equilibrium runs were performed at 16,000 rpm using protein concentrations of 0.05 – 1 mg/ml. The protein distribution in the cell was monitored at 230 or 280 nm and the data were analyzed using the software *SedFit* (Schuck, 2000). No concentration-dependent assembly was observed in the applied concentration range.

4.4. Crystallographic methods

4.4.1. Crystallization of Mitofilin_C-CHCH

Crystallization trials were carried out using the sitting drop vapor diffusion method in 96 well crystallization plates using an automated dispensing robot (Crystal Gryphon, Art Robbins Instruments). The frozen protein was thawed on ice and diluted in SEC buffer (20 mM HEPES, pH 7.5, 150 mM NaCl) to 17-20 mg/ml, if possible. 0.2 µl protein solution and 0.2 µl of reservoir solution were mixed (80 µl total reservoir volume) and incubated at 4 °C or 20 °C in cabinets, which store and image crystallization plates (Rock Imager 1000, Formulatrix). Thin crystal needles were obtained at 20 °C in conditions containing 10% (w/v) PEG 6000 and 0.1 M HEPES, pH 7.0 (pH Clear Suite (Qiagen) and JBScreen JCSG++ HTS (Jena Bioscience)). Crystals grew within 24-72 h. To optimize crystal size, several approaches were performed, including variation of protein concentration, pH, growth temperature, precipitant concentration or drop volume ratio. Furthermore, several additives like DTT or glycerol, as well as *Additive Screens* (JBScreen Plus HTS (Jena Bioscience) or Silver Bullets (Hampton Research)) were used. The liquid dispensing system FORMULATOR® (Formulatrix) was used to prepare new 96 well fine screens. Moreover, crystallization trials were carried out in 24 well crystallization plates in hanging drop format by manual preparation. Different volumes of protein solution and reservoir solution were mixed (0.5-3.0 µl) and placed above 100-1000 µl reservoir solution.

Limited proteolysis, prior to protein crystallization, was used as a further attempt. For this purpose, trypsin from bovine pancreas (Sigma-Aldrich) was dissolved in 1 mM HCl and 2 mM $CaCl_2$ to 1 mg/ml. Mitofilin_C-CHCH (17-20 mg/ml) was incubated with 0.1% to 1% (w/w) trypsin for 10 min on ice, followed by automated dispensing to 96 well crystallization plate, as described above. As a result, small plate-shaped crystals were obtained using 1% trypsin at 20 °C with two conditions of the commercial screen JBScreen JCSG++ HTS (Jena Bioscience) containing 40% (v/v) MPD, 5% (w/v) PEG 8000, 0.1 M MES, pH 6.5 or 30% (v/v) Jeffamine® M-600, 0.1 M HEPES, pH 7.0. Using the first condition, crystals appeared after ten days and grew for four more days, while crystals grew within three days using the second condition. Both conditions were fine screened (1% trypsin, 20 °C) and the latter condition yielded improved crystal size and thickness. As crystals grew together, many crystals were tested, which seem to be single or showed only a small overlap. Tobias Bock-Bierbaum (MDC) fished the

crystals and transferred them directly into liquid nitrogen. The best-diffracting crystal appeared between day 3 to day 7 and reached its final size until day 9, with a reservoir solution containing 33% (v/v) Jeffamine M-600, 0.1 M HEPES, pH 7.2.

4.4.2. Crystallization of Mitofilin-CHCH_2 and Mitofilin-CHCH_3

Initial crystallization trials for constructs containing LBS, mitofilin domain and CHCH domain, including Mitofilin-CHCH_2 and Mitofilin-CHCH_3, were performed as described for Mitofilin_C-CHCH (4.4.1) using the sitting drop vapor diffusion method in 96 well crystallization plates and an automated dispensing robot (Crystal Gryphon, Art Robbins Instruments). Different screens were applied: JBScreen JCSG++ HTS, JBScreen Basic HTS (both Jena Bioscience), Morpheus Screen (Molecular Dimensions Limited), Classics II Suite, pH Clear Suite, Protein Complex Suite (all Qiagen). Crystals were obtained using 18 mg/ml Mitofilin-CHCH_3 or 15 mg/ml Mitofilin-CHCH_2 at 20 °C with reservoir solution 20% (w/v) PEG MME 2000, 0.1 M TRIS, pH 8.5, 0.2 M TMANO (JBScreen JCSG++ HTS). Plate-shaped crystals of Mitofilin-CHCH_2 grew within the first three days. Cubic or plate-shaped crystals of Mitofilin-CHCH_3 appeared after two days and grew until day 10. Due to the high amount of protein precipitate in the crystal drop, crystallization trials were repeated using half the protein concentration (diluted with SEC buffer) and JBScreen JCSG++ HTS screen. As a result, crystals were obtained in two additional conditions: 30% (w/v) Jeffamine ED-2001, 0.1 M HEPES, pH 7.0 (Mitofilin-CHCH_2) and 2.1 M di-sodium DL malate, pH 7.0 (Mitofilin-CHCH_3). As plates grew together, they were broken apart to fish single pieces. Crystal fishing was carried out by Tobias Bock-Bierbaum (MDC). The best diffraction was obtained by a plate of Mitofilin-CHCH_2. The corresponding crystal appeared after three days and was fished at the following day. It was obtained using 7.5 mg/ml protein and a reservoir solution containing 30% (w/v) Jeffamine ED-2001, 0.1 M HEPES, pH 7.0.

4.4.3. Data collection and processing

All diffraction data were collected at the BESSY II electron storage ring operated by the Helmholtz-Zentrum Berlin (Berlin-Adlershof, Germany) (Mueller et al., 2015; Gerlach et al., 2016). The final data sets of Mitofilin_C-CHCH and Mitofilin-CHCH_2 were obtained at beamline BL14.1 equipped with a Pilatus 6M pixel-detector (DECTRIS, Switzerland) at a wavelength of 0.91840 Å (13.5 keV) at -173 °C (100 K). For Mitofilin_C-CHCH, 800 images were collected using 1.5 s exposure time (31.21% transmission), 293.456 mm detector distance and an oscillation increment of 0.3 °. 700 images were collected for Mitofilin-CHCH_2 using 1 s exposure time (100% transmission), 423.800 mm detector distance and oscillation increment of 0.3 °. Diffraction data were indexed, integrated and scaled with *XDSAPP* (Sparta et al., 2016), performed by Yvette Roske (MDC).
Matthews coefficient and solvent content were calculated using the *MATTPROB* online tool (Weichenberger and Rupp, 2014; Kantardjieff and Rupp, 2003; Matthews, 1968).

4.4.4. Phase determination and refinement

As there were no structural information for Mic60 or Mic19, the phase problem of Mitofilin_C-CHCH was solved by molecular replacement using *AMPLE* from the *CCP4* software package (Winn et al., 2011; Bibby et al., 2012; Thomas et al., 2015) by placement of three ideal α-helices, consisting of 30 alanine residues. Subsequently, *Phaser-MR* (McCoy et al., 2007) from the *PHENIX* software suite (Adams et al., 2010; Liebschner et al., 2019) was used to place additional helices. The structure of Mitofilin_C-CHCH was finally solved by using *SHELXE* (Thorn and Sheldrick, 2013; Sheldrick, 2008) and *AutoBuild* (Terwilliger et al., 2008) from the *PHENIX* suite by expansion of the polyalanine helices and automated model-building. The structure of Mitofilin-CHCH_2 was solved by molecular replacement with *Phaser-MR* using the structure of Mitofilin_C-CHCH as search model.
The initial models of Mitofilin_C-CHCH and Mitofilin-CHCH_2 were refined using *phenix.refine* (Afonine et al., 2012) from the *PHENIX* suite and iterative steps of manual model building in *Coot* (Emsley et al., 2010). Maximum likelihood refinement with individual B-factors, NCS (Non-crystallographic symmetry), TLS (Translation-

Libration-Screw) and secondary structure restraints were used. Generation of ligand restraints was carried out by eLBOW (Moriarty et al., 2009) from the *PHENIX* suite.

4.4.5. Structure analysis and figure preparation

Final protein structures were validated using *MolProbity* (Williams et al., 2018; Chen et al., 2010) from the *PHENIX* software suite (Adams et al., 2010; Liebschner et al., 2019). Data collection and refinement statistics are presented in Table 7, Table 8, Table 10 and Table 11. Data will be deposited in the *Protein Data Bank* (PDB).

PDBePISA ('Protein interfaces, surfaces and assemblies' service PISA at the European Bioinformatics Institute; http://www.ebi.ac.uk/pdbe/prot_int/pistart.html*)* web server (Krissinel and Henrick, 2007) was used to calculate the interface area between the mitofilin domain and the CHCH domain of Mitofilin_C-CHCH (Chain A).

Figures of protein structures were prepared using *PyMOL* (The PyMOL Molecular Graphics System, Version 1.8.2.3 Schrödinger, LLC). The *align* function was used for superposition of the structures and calculation of root-mean-square deviations.

Electrostatic surface potential was generated using the APBS electrostatics plugin (method: PDB2PQR; Jurrus et al., 2018) of *PyMOL* (The PyMOL Molecular Graphics System, Version 2.0.3 Schrödinger, LLC).

Surface conservation plot was generated using the *ConSurf* server (Ashkenazy et al., 2016; Landau et al., 2005) and figures were prepared in *PyMOL* (The PyMOL Molecular Graphics System, Version 1.8.2.3 Schrödinger, LLC). Multiple sequence alignments for surface conservation plots were performed by the *ConSurf* server using the standard settings (Homolog search algorithm: HMMER; Number of iterations: 1; E-value cutoff: 0.001; protein database: UNIREF-90). The mitofilin domain (including LBS1) and the CHCH domain were analyzed independently. Homologs for *ConSurf* analysis were automatically selected (150 sequences, maximal 95% sequence identity between sequences; minimal 35% sequence identity for homologs; MAFFT-L-INS-I alignment method). Bayesian calculation method was used for the rate of evolution at

each site in the multiple sequence alignment (Evolutionary substitution model: best model).

The *EVolutionary Couplings Server* (Monomer pipeline, version 1; Hopf et al., 2019), was used for structure predictions by Jeffrey Noel (MDC). Structure predictions of ctMic60_557-685 could be obtained using the input sequence ctMic60_550-693 (bitscore 0.1). The highest scoring folding candidate is shown (Figure 30).

The model of Mic60 and Mic19 in crista junctions (Figure 45) was created and prepared by Dr. Erik Werner (2021), RNS Berlin (www.rns.berlin). The model comprises the crystal structures of the coiled-coil domain of *Lachancea thermotolerans* Mic60 (235-382) of Tobias Bock-Bierbaum (MDC) and the *Chaetomium thermophilum* Mitofilin-CHCH_2 dimer (chains C and D) of this work, whereby the sequence of *Lachancea thermotolerans* Mic60 was used as template. All other parts of Mic60 were modeled as unstructured regions. A crista junction diameter of 17.5 nm was used. The model was generated using the Maya® software from Autodesk, Inc. (https://www.autodesk.com/products/maya/) and *Modeling kit* and *Rigging kit* of the plugin *Molecular Maya (mMaya)* from Digizyme, Inc. (https://clarafi.com/tools/mmaya/).

5. Results

5.1. Protein expression and purification of the Mic60-Mic19 fusion construct

The MICOS complex can be divided into two subcomplexes, one of them comprising Mic60 and Mic19. Manuel Hessenberger, a former PhD student of the Daumke lab (MDC), analyzed the interaction between Mic60 and Mic19 in detail and found that the mitofilin domain of Mic60 and the CHCH domain of Mic19 from the thermophilic fungus *Chaetomium thermophilum* (ct) are crucial for the Mic60-Mic19 interaction (Hessenberger et al., 2017). The domain architecture of these proteins is shown in Figure 10. Many crystallization trials with different Mic60 and Mic19 constructs (including different species) were previously performed without success. However, a fusion construct of the mitofilin domain and the CHCH domain (Figure 10) could be crystallized as small, thin needles.

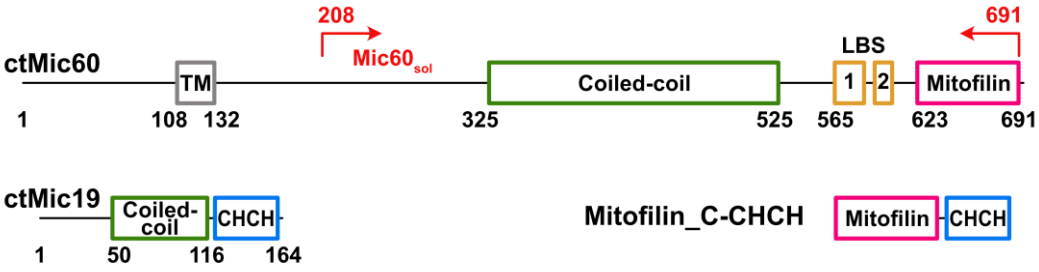

Figure 10: Schematic representation of the domain structure of *Chaetomium thermophilum* (ct) Mic60, Mic19 and fusion construct Mitofilin_C-CHCH used in this study, based on secondary structure prediction *PSIPRED* (Buchan and Jones, 2019; Jones, 1999; see also Appendix C); TM: transmembrane helix, Coiled-coil: coiled-coil domain, LBS: lipid binding site, Mitofilin: mitofilin domain, CHCH: coiled-coil-helix-coiled-coil-helix (CHCH) domain; numbers show the amino acid position; in this study a soluble Mic60 construct $Mic60_{sol}$ was used instead of full-length Mic60, construct borders are indicated. Construct Mitofilin_C-CHCH: ctMic60_624-691-GSGS-ctMic19_116-164; G: glycine, S: serine.

In order to obtain detailed insights into the interaction of Mic60 and Mic19, I continued working on this Mitofilin_C-CHCH construct and cloned it into a different vector (see 4.2.12). Mitofilin_C-CHCH was recombinantly expressed in *E. coli* BL21(DE3) with an

N-terminal His_6-tag (see 4.3.4). A specific band with the corresponding molecular mass was observed on SDS-PAGE gel of the induced sample (Figure 11 A). To obtain highly concentrated and pure protein for crystallization trials, Mitofilin_C-CHCH was purified using immobilized metal ion affinity chromatography (IMAC) and size-exclusion chromatography (SEC) according to the established protocol (see 4.3.6.). Following cleavage of the His_6-tag, the protein was eluted with low concentration of imidazole from the Ni-NTA column (Figure 11 B, FT1, FT2). Protein was pooled, concentrated and further purified using SEC (Figure 12).
Typical yields of 15-50 mg protein per liter bacteria culture were obtained.

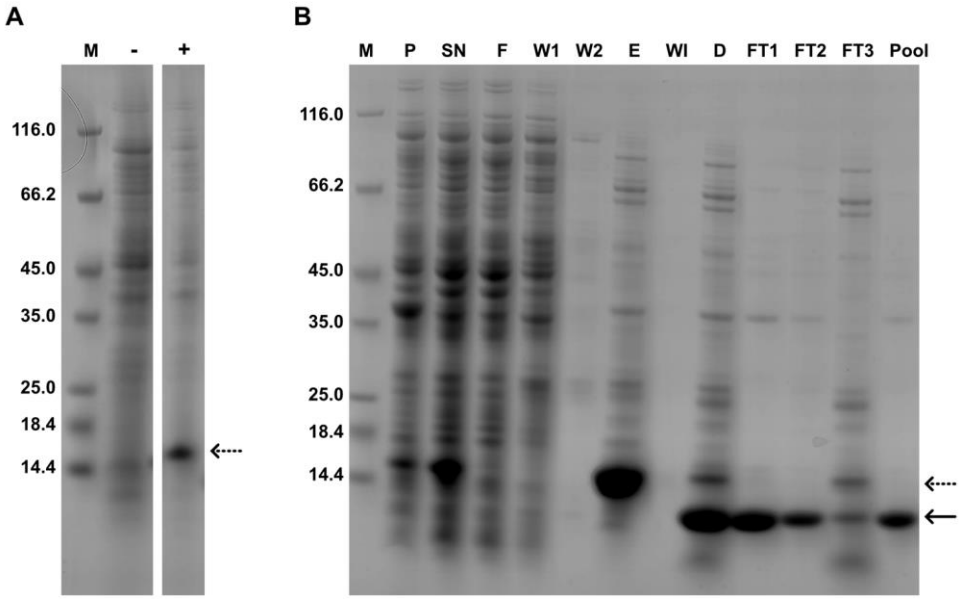

Figure 11: Mitofilin_C-CHCH expression and IMAC purification. 4-12% SDS-PAGE gels stained with Coomassie Brilliant Blue. **(A)** Expression: M: marker: Unstained Protein MW Marker (Thermo Fisher Scientific); numbers indicate the molecular weight (MW) in kDa; samples before (-) and after (+) IPTG addition. **(B)** IMAC purification: P: pellet after cell disruption and centrifugation, dissolved in 8 M urea; SN: supernatant after cell disruption and centrifugation; F: collected flow-through during loading of supernatant to the column; W1, W2, WI: collected wash fractions (20 mM, 1 M imidazole); E: elution after the first IMAC; D: protein solution after dialysis; FT1: collected flow-through during loading of dialysis solution to the column; FT2: collected fraction during elution with buffer containing 20 mM imidazole to elute protein after the second IMAC; FT3: collected fraction during elution with buffer containing 300 mM imidazole; Pool: pooled sample (FT1 and FT2); dashed arrow shows His-tagged Mitofilin_C-CHCH; arrow shows Mitofilin_C-CHCH construct after cleavage of the His-tag.

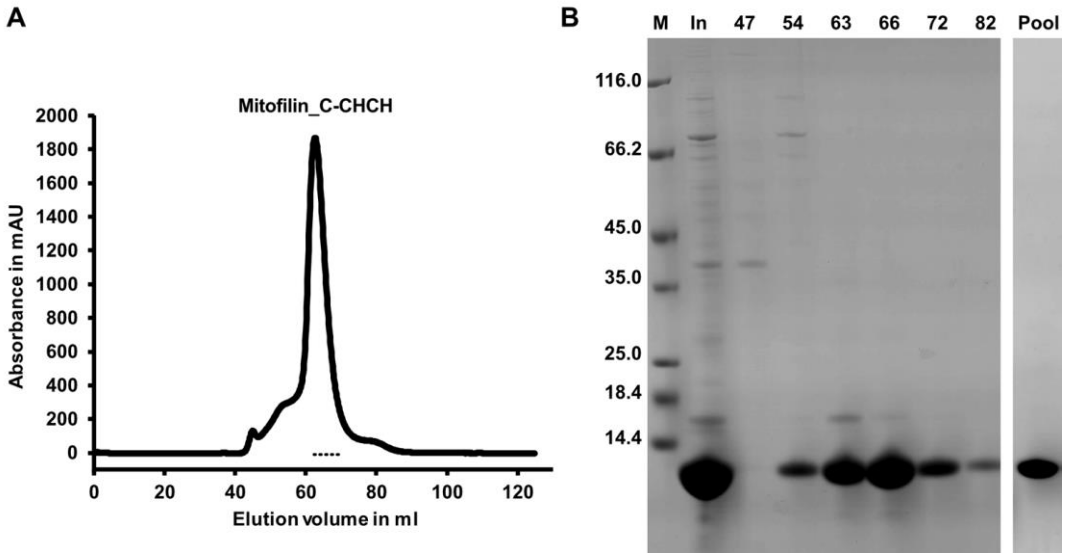

Figure 12: Mitofilin_C-CHCH SEC purification. (A) SEC purification chromatogram: An ÄKTApurifier chromatography system connected to a HiLoad 16/600 Superdex 75 pg column (GE Healthcare) was used. Absorption was measured at 280 nm. 1 ml fractions were collected. The dashed line shows pooled fractions. **(B)** 4-12% SDS-PAGE gel from SEC purification stained with Coomassie Brilliant Blue; M: marker: Unstained Protein MW Marker (Thermo Fisher Scientific); numbers at the left side of the marker indicate the MW in kDa; In: injected protein solution; Pool: pooled sample; numbers above the gel show retention volumes of selected peak fractions in ml.

5.2. Crystallization and structure determination of the Mic60-Mic19 fusion construct

In order to gain structural insights into Mitofilin_C-CHCH, and in particular the Mic60-Mic19 interaction interface, crystallization trials were performed (see details in 4.4.1.). The previously described needles could be reproduced (Figure 13 A, B). In order to improve the needles in size, several approaches were used: Protein concentration, precipitant concentration, pH, growing temperature and drop ratio were varied, or certain additives like DTT, glycerol or citrate added, and different crystallization methods used. None of them resulted in increased crystal size.

Flexible regions within the constructs might disturb crystallization, but are accessible for proteases. Therefore, limited proteolysis was performed using trypsin to improve crystal packing (see 4.4.1 for details), resulting in crystals of a different shape

(Figure 13 C, D). Fine screening of the latter condition improved the crystal size and thickness (Figure 13 E, F).

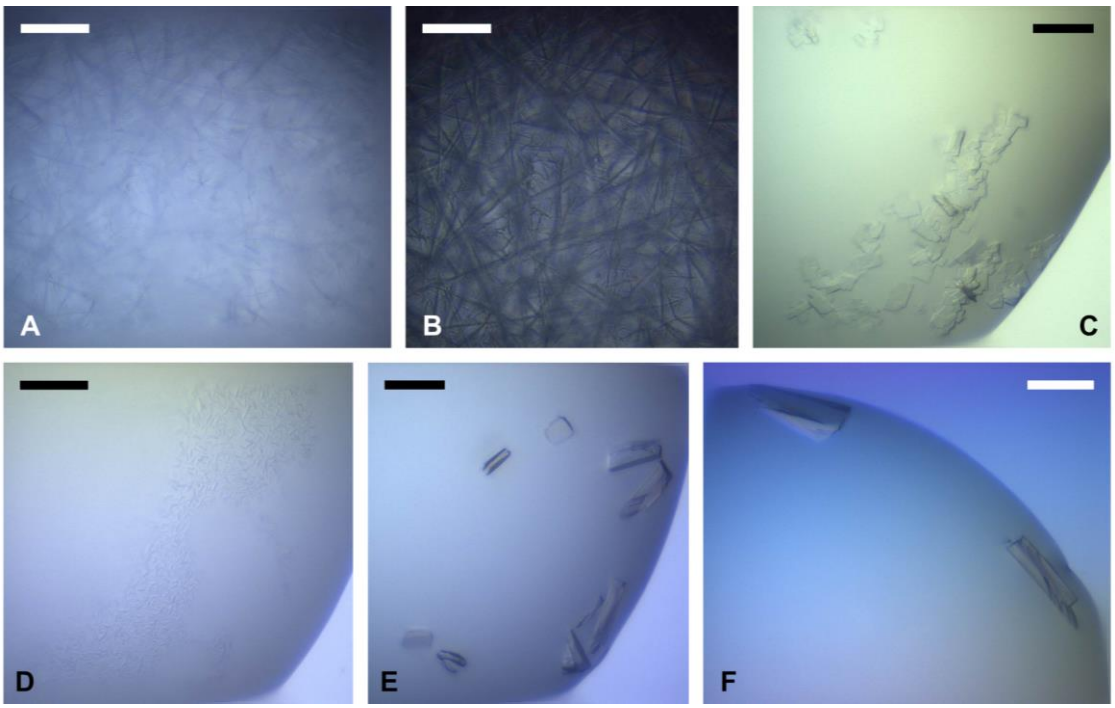

Figure 13: Images of Mitofilin_C-CHCH crystals. The scale bar (white or black) indicates 100 µm. **(A)** Initial crystals (needles) of Mitofilin_C-CHCH obtained in screening condition 10% (w/v) PEG 6000 and 0.1 M HEPES, pH 7.0. **(B)** Same crystals as in (A) using Vis-Condenser 75%. **(C)**, **(D)** Initial crystals (plates) of Mitofilin_C-CHCH after limited proteolysis using trypsin in condition 40% (v/v) MPD, 5% (w/v) PEG 8000, 0.1 M MES, pH 6.5 (C) or 30% (v/v) Jeffamine M-600, 0.1 M HEPES, pH 7.0 (D). **(E)** Optimized crystals of (D). **(F)** Optimized crystals of (D) and (E). Crystals grew in a crystallization solution containing 33% (v/v) Jeffamine M-600, 0.1 M HEPES, pH 7.2. The crystal at the top reached a size of approximately 150 µm x 50 µm and showed diffraction to a resolution of 2.15 Å.

Mass spectrometry analysis was performed to identify the size of the trypsin-digested product (Figure 14; see 4.3.8.). Untreated Mitofilin_C-CHCH showed a molecular mass of 14.138 kDa, whereas the calculated molecular mass was 14.140 kDa. The difference of 2 Da may confirm the presence of a disulfide bond in the CHCH domain, in line with previous predictions (Darshi et al., 2011; Sakowska et al., 2015).

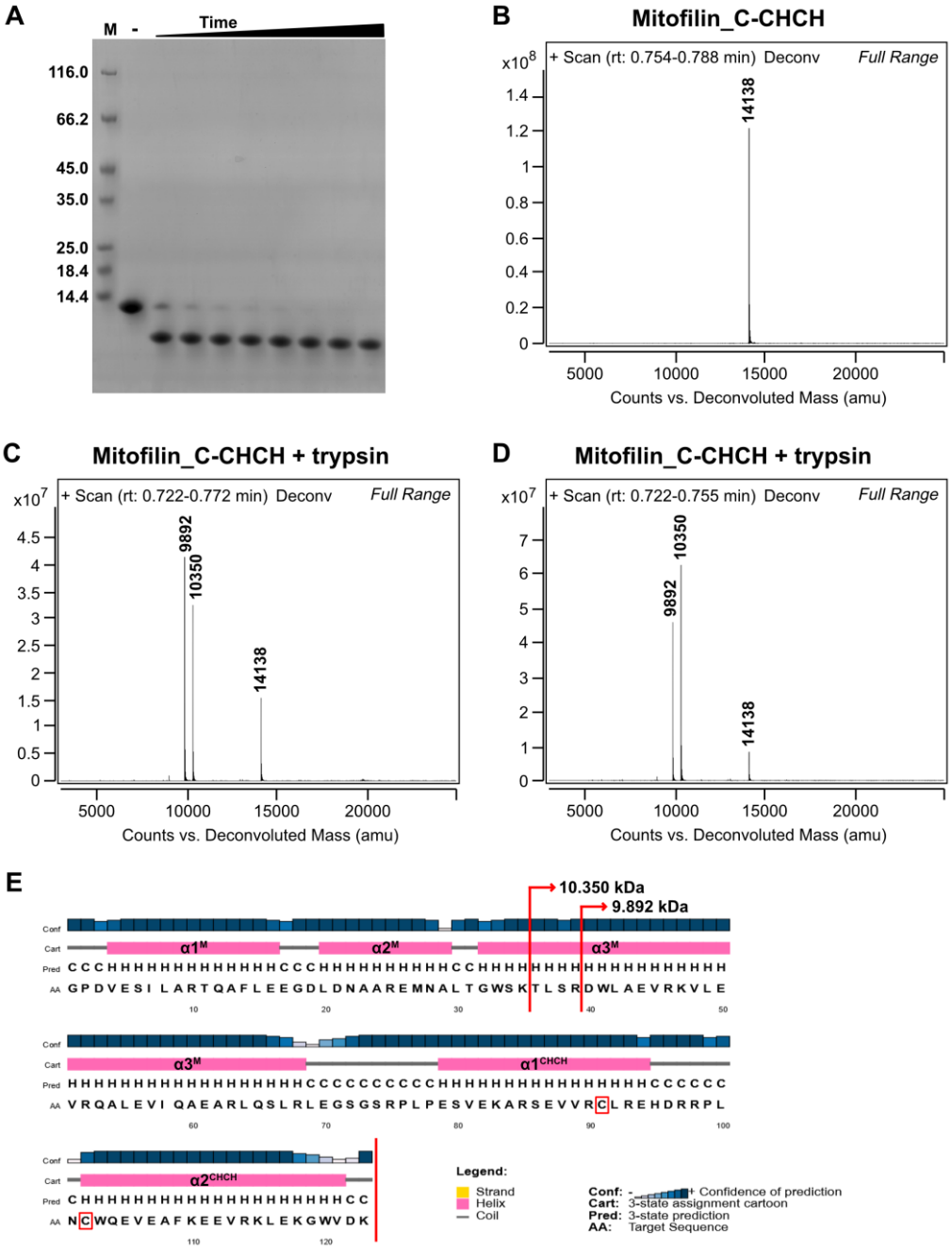

Figure 14: Limited proteolysis of Mitofilin_C-CHCH and mass spectrometry analysis. **(A)** 4-12% SDS-PAGE gel stained with Coomassie Brilliant Blue; M: marker: Unstained Protein MW Marker (Thermo Fisher Scientific); numbers indicate MW in kDa; the untreated protein sample is marked with a minus (-); the bar indicates the incubation time after addition of 1% trypsin (w/w), samples were taken every 10 min starting with 20 min incubation time. **(B)**, **(C)**, **(D)** Mass spectrometry (LC-ESI-Q-TOF-MS) deconvoluted spectra. The numbers above the peaks show the molecular mass in Da. (B) Mitofilin_C-CHCH before addition of trypsin. (C) Mitofilin_C-CHCH after 5 h incubation with 3% trypsin (w/w). (D) Mitofilin_C-CHCH after 15 h incubation with 3% trypsin (w/w); independent of (C). **(E)** Secondary structure prediction of Mitofilin_C-CHCH using *PSIPRED* (Buchan and Jones, 2019; Jones, 1999). α-helices are labelled, M: mitofilin domain, CHCH: CHCH domain. Arrows indicate the two stable fragments obtained after limited proteolysis confirming that the disulfide bond is formed; cysteines are labelled with red frames.

Trypsin digestion of Mitofilin_C-CHCH led to a stable degradation band (Figure 14 A). Surprisingly, two stable fragments of 10.350 kDa and 9.892 kDa were observed in mass spectrometry, which appeared as one band on SDS-PAGE (Figure 14 C, D). Since trypsin cleaves C-terminal to arginine and lysine residues (Olsen et al., 2004), the two fragments were identified as N-terminal truncations corresponding to Mitofilin$^{aa\text{-}657\text{-}691}$-CHCH and Mitofilin$^{aa\text{-}661\text{-}691}$-CHCH (Figure 14 E). Both proteins contain the complete CHCH domain of Mic19 and approximately half of the mitofilin domain of Mic60.

X-ray data of the optimized native crystals containing trypsin-digested Mitofilin_C-CHCH (Figure 13 F) were collected at BESSY II in Berlin (see 4.4.3). The best diffracting crystal reached a maximal resolution of 2.15 Å and belonged to space group P1. Data collection statistics are summarized in Table 7.

Table 7: **Data collection statistics of Mitofilin_C-CHCH.** Values in parentheses are for highest-resolution shell.

Data collection	
Space group	P1 (1)
Cell dimensions	
a, b, *c* (Å)	43.82, 48.52, 70.74
α, β, γ (°)	82.70, 79.14, 72.41
Resolution (Å)	46.12 – 2.15 (2.28 – 2.15)
R_{meas} (%)	9.0 (111.5)
I/σI	8.28 (0.92)
Completeness (%)	91.8 (92.3)
Multiplicity	2.5 (2.5)
$CC_{1/2}$ (%)	99.8 (52.9)

Assuming a molecular mass of the digested product of 10 kDa (Figure 14), the unit cell parameters indicate a high probability for six molecules per asymmetric unit and a Matthews coefficient of 2.3 Å^3/Da, corresponding to a solvent content of 47% (see 4.4.3; Weichenberger and Rupp, 2014; Kantardjieff and Rupp, 2003; Matthews, 1968).

Although no prior structural information on either Mic60 or Mic19 was available, the structure was solved by molecular replacement using three ideal α-helices as template (see details in 4.4.4.). The resulting model was improved by several rounds of refinement (see 4.4.4). The final model has six molecules in the asymmetric unit, and R_{work} and R_{free} values of 24.0% and 26.8% (Table 8).

Table 8: **Refinement statistics of Mitofilin_C-CHCH.** Values in parentheses are for highest-resolution shell.

Refinement	
Resolution (Å)	46.12 – 2.15
Total no. of reflections	68,282 (11,094)
R_{work} / R_{free} (%)	24.0 / 26.8
No. of atoms	
Protein	3,815
Ligand	333
Water	19
B-factors (Å^2)	
Protein	68.13
Ligand	94.65
Water	44.25
RMS deviations	
Bond lengths (Å)	0.007
Bond angles (°)	0.73
Ramachandran plot	
Favored (%)	99.07
Allowed (%)	0.93
Outliers (%)	0.00
Rotamer outliers (%)	0.25
Clashscore	4.34

In addition to the protein, 19 water molecules and five ligands were included in the model. 99% of the residues were in the favored region of the Ramachandran plot and no Ramachandran outliers could be detected (Table 8). A clashscore of 4.34, with only 0.25% rotamer outliers, points to a well refined model.

5.3. Structural analysis of the mitofilin domain and the CHCH domain

In solution, Mitofilin_C-CHCH appears as a mixture of monomers and dimers, as observed in analytical size exclusion chromatography coupled to right-angle light scattering (SEC-RALS) experiments (Appendix D). SEC-RALS analysis of Mitofilin_C-CHCH after limited proteolysis resulted in many peaks in size exclusion chromatography, precluding a detailed analysis. Based on these data, it was a surprising observation that six molecules of Mitofilin_C-CHCH are present in the asymmetric unit, which are arranged as two trimers (Figure 15). Chain A and B within one trimer extend in parallel, whereas chain C is antiparallel to chain A and chain B. The second trimer has the same architecture.

All six chains are well defined in the electron density. 79 of 88 amino acids of the longest stable fragment (after trypsin digestion) could be modelled in at least one chain (Figure 16 A). Electron density of the remaining residues is missing due to flexibility. Amino acids missing electron density for side chains were modelled as alanines.
Each protein chain comprises a part of the mitofilin domain (residues 661-691) of Mic60 and the complete CHCH domain (residues 118-159) of Mic19 (Figure 16), which is in agreement with the mass spectrometry data of trypsin-digested Mitofilin_C-CHCH (Figure 14). Also in line with the mass spectrometry analysis (Figure 14 E), the crystal seems to consist of longer and shorter fragments, which differ by four residues on the N-terminus: Chains B and E represent the smaller fragment, while the antiparallel chains C and F represent the bigger fragment. Due to ambiguous electron density, chains A and D cannot be classified.

Chains A-F could be well superimposed, with root-mean-square deviations (RMSDs) from 0.220-0.495 Å for 53-64 Cα, indicating a highly related fold. Exceptions are the N- and C-termini and the connection between mitofilin domain and CHCH domain, including the non-natural GSGS linker, which appears to be more flexible and adapts several conformations in the crystal lattice (Figure 16 C).

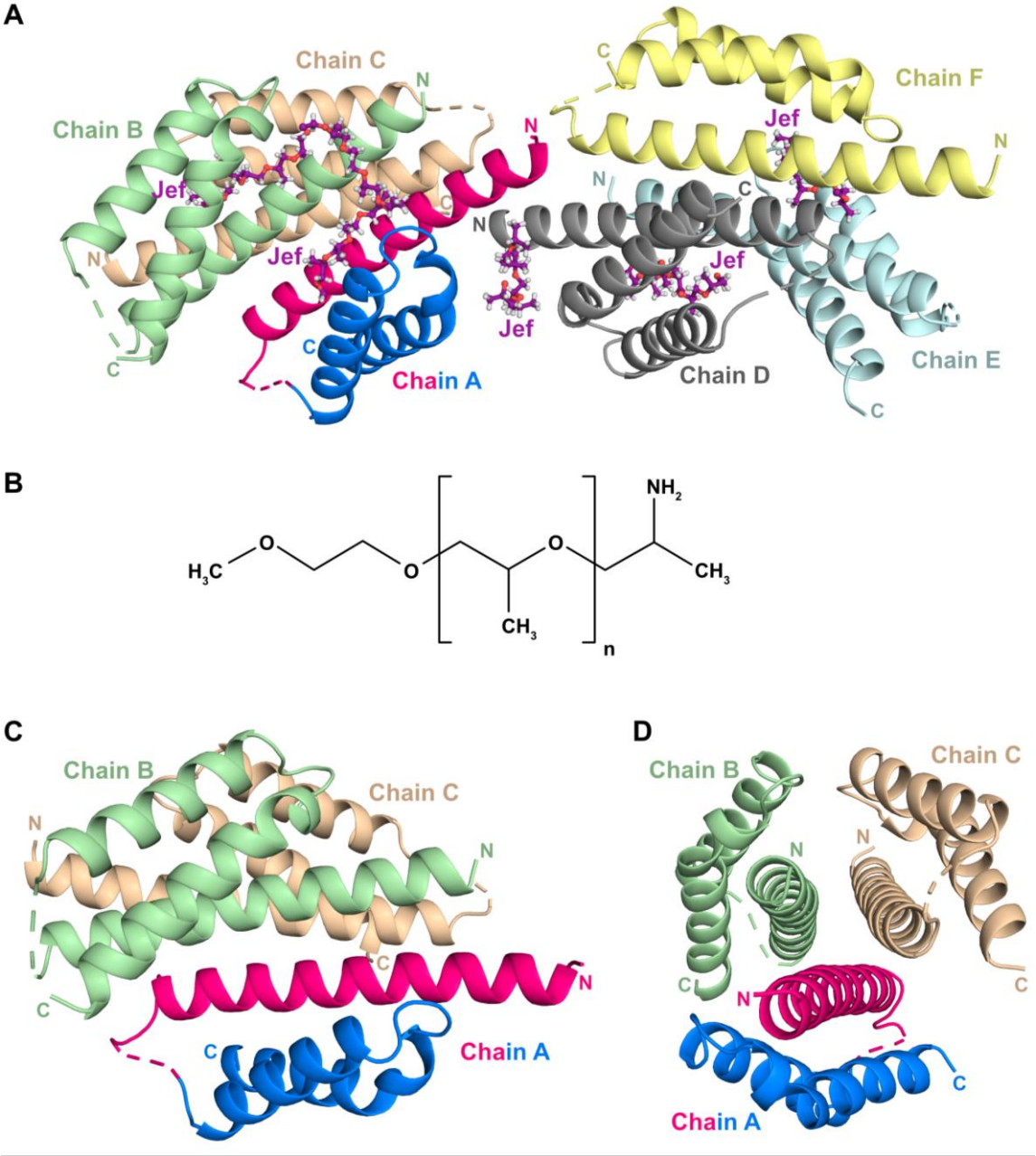

Figure 15: Crystal structure of Mitofilin_C-CHCH fusion construct after limited proteolysis. (A) The asymmetric unit contains six molecules, arranged as two trimers. Chains are colored individually and shown in ribbon representation. Chain A: pink (mitofilin domain) and blue (CHCH domain), chain B: green, chain C: beige, chain D: grey, chain E: cyan, chain F: yellow. N- and C-termini are labelled with N or C. The linker region is not resolved in the crystal structure and indicated by a dashed line. Five molecules Jeffamine M-600 (Jef) were built (different lengths), colored in purple. **(B)** Structural formula of Jeffamine M-600 (O-(2-Aminopropyl)-O'-(2-methoxyethyl) polypropylene glycol or polypropylene glycol 500 mono-2-aminoethyl mono-2-methoxyethyl ether), derived from JBScreen JCSG++ HTS (Jena Bioscience), average MW ~600, n = 8. **(C)**, **(D)** Trimer composed of chains A, B and C without Jeffamine M-600.

During the process of model building, I found several regions with elongated, unexplained difference electron density. Based on the buffer conditions, I assigned them as Jeffamine M-600 (Jef) molecules or fragments therefore (Figure 15 A). As shown in Figure 15 B, a feature of Jeffamine M-600 is its hydrophobic surface. Thereby, it can fill up large hydrophobic pockets and thus improve crystal packing. Jeffamine M-600 molecules were modelled in between chain A and B, A and D, B and C, D and E, E and F. However, their exact register was difficult to define, due to ambiguous electron density. Furthermore, there might be several different conformations within different asymmetric units of the crystal.

A monomer of Mitofilin_C-CHCH is composed of three α-helices: a long helix from the mitofilin domain ($\alpha3^{M}$) and two shorter helices forming the Mic19 CHCH domain ($\alpha1^{CHCH}$ and $\alpha2^{CHCH}$) (Figure 16). Interestingly, the first two predicted helices of the mitofilin domain were cleaved by limited proteolysis. In agreement with mass spectrometry data (Figure 14), the CHCH domain contains a disulfide bond, which is visible in all chains and leads to the formation of a 3_{10}-helix at the beginning of the second CHCH domain helix ($\alpha2^{CHCH}$). As a result, helix $\alpha2^{CHCH}$ appears to be partially bent. The CHCH domain folds back onto the mitofilin domain helix, which may protect the protein from further digestion. The monomers within the asymmetric unit interact with each other via the mitofilin domain and hydrophobic contacts. Overall, this topology is in accordance with the secondary structure prediction (Figure 14 E).

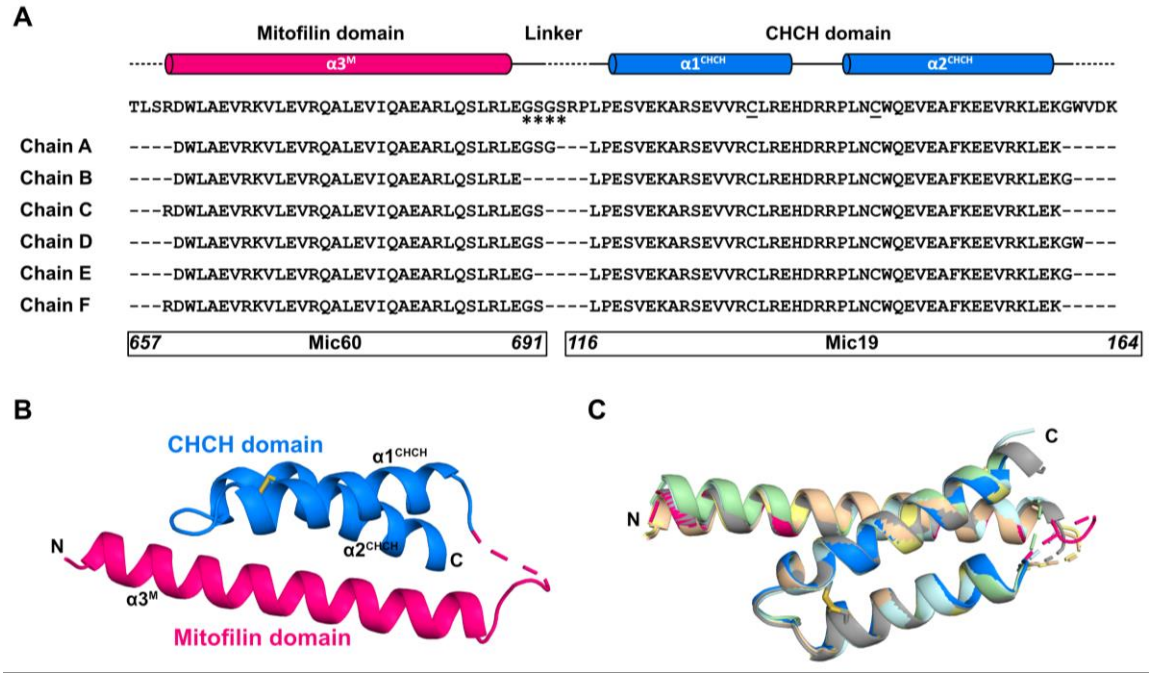

Figure 16: Monomer structure of Mitofilin_C-CHCH and alignment. (A) Sequence alignment and overview of all chains of the asymmetric unit. Domains are colored in pink (mitofilin domain) and blue (CHCH domain). The non-natural GSGS linker is marked with asterisks and the cysteine residues forming a disulfide bond are underlined. Strokes within the sequence represent amino acids, which could not be modelled. Cursive numbers at the bottom display the nomenclature according to Mic60 or Mic19. α-helices are labelled and numbered according to Mitofilin_C-CHCH (before limited proteolysis); two helices were cleaved by trypsin; M: mitofilin domain, CHCH: CHCH domain. **(B)** Monomer (chain A) of Mitofilin_C-CHCH fusion construct after limited proteolysis shown in ribbon representation. Domains are labelled and colored as in (A); termini and helices are labelled. The linker region is not resolved in the crystal structure and indicated by a dashed line. The disulfide bond is depicted in orange. **(C)** Monomer as in (B) 120 ° turned counter-clockwise (x-axis) and aligned with the five additional monomers of the asymmetric unit (see Figure 15). Chains B - F are colored individually, chain B: green, chain C: beige, chain D: grey, chain E: cyan, chain F: yellow.

5.4. Identification of the Mic60-Mic19 interaction interface

The structure of the mitofilin domain of Mic60 and the complete CHCH domain of Mic19 allowed for a detailed analysis of the respective interaction surface (Figure 17). Since the CHCH domain folds back onto the mitofilin domain, all three helices are involved in the interaction. Within the crystal, surface-exposed side chains of amino acids may adopt different conformations in different protein chains, for instance due to crystal packing. However, residues involved in the interaction may be stabilized in a functionally relevant orientation. Such amino acid side chains in the interaction interface, showing similar conformation in all protein chains, are depicted in Figure 17.

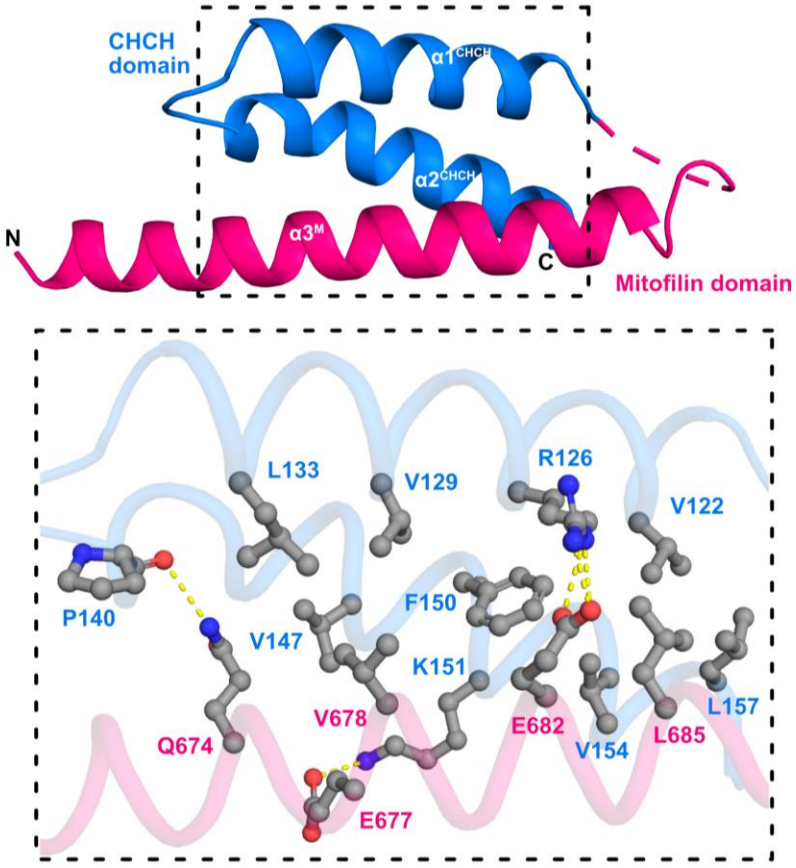

Figure 17: Monomer structure of Mitofilin_C-CHCH and interaction interface. Monomer (chain A) after limited proteolysis shown in ribbon representation. Domains are colored individually and termini are labelled. The linker region is not resolved in the crystal structure and indicated by a dashed line (pink). α-helices are labelled and numbered according to Mitofilin_C-CHCH (before limited proteolysis). Black dashed rectangle indicates Mic60-Mic19 interface shown in detail. Selected residues involved in the interaction are shown and labelled (color according to domain affiliation).

The interaction interface consists of a hydrophobic core surrounded by polar interactions. Residues in the hydrophobic core include V678, L685 in the mitofilin domain, and V122, V129, L133, V147, F150, V154, L157 in the CHCH domain. The two helices of the CHCH domain are also stabilized by hydrophobic interactions, where the aromatic residue F150 seems to be in a central position. Furthermore, the interaction between the mitofilin domain and the CHCH domain is stabilized by a sidechain-backbone interaction between Mic60_Q674 and Mic19_P140, as well as salt-bridges involving residues Mic60_E682-Mic19_R126 and Mic60_E677-Mic19_K151, flanking the hydrophobic core. The plethora of residues involved in the interaction accounts for an interface area of 688.2 $Å^2$, which may enable the previously determined high affinity interaction in the high nanomolar range of the two domains (Hessenberger et al., 2017).

5.5. *In vitro* characterization of the Mic60-Mic19 interaction

5.5.1. Protein expression and purification of Mic60-Mic19 interface mutants

The above described crystal structure describes a Mic60-Mic19 interaction interface. However, this structure was derived from a fusion construct, in which the mitofilin domain of Mic60 and the CHCH domain of Mic19 were directly connected and expressed as one protein. To confirm that the same interface is used in full-length or almost full-length Mic19 and Mic60, respectively, I used a structure-based mutagenesis approach, using previously established constructs. Interface mutations were introduced into $Mic60_{sol}$ (amino acids 208-691) or Mic19, and the interaction of the proteins was tested. Hydrophobic residues were mutated to aspartate, whereas other amino acids were mutated to alanine.

The resulting mutants (including $Mic60_{sol}$ and Mic19) were purified via IMAC and SEC (see 5.1.) (Figure 18), in accordance with previous results.

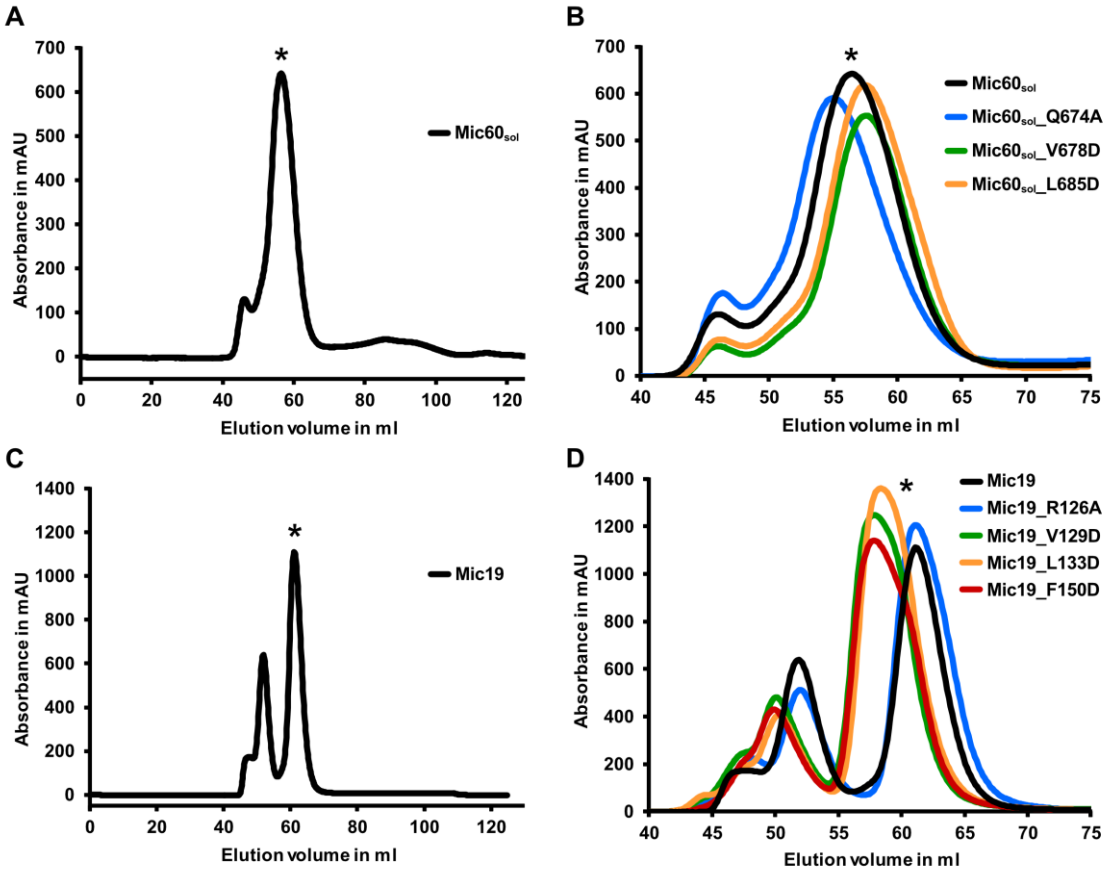

Figure 18: SEC purification chromatograms of $Mic60_{sol}$, Mic19 and interaction interface mutants. An ÄKTApurifier chromatography system connected to a HiLoad 16/600 Superdex 200 pg column or HiLoad 16/600 Superdex 75 pg column (GE Healthcare) was used. Absorption was measured at 280 nm. 1 ml fractions were collected. Asterisks show pooled peaks. **(A)**, **(B)** HiLoad 16/600 Superdex 200 pg column. **(C)**, **(D)** HiLoad 16/600 Superdex 75 pg column.

As previously described, the SEC profile of Mic19 shows a separation into monomers, containing an internal cysteine bond in the CHCH domain, and dimers containing an artificial intermolecular disulfide bridge (Figure 18 C; Hessenberger et al., 2017). Only the monomer peak was pooled and used for further characterization. The overlay of the SEC profiles for the main peak area is shown in Figure 18 B and Figure 18 D. All $Mic60_{sol}$ mutants displayed a similar peak profile as $Mic60_{sol}$, where the peak was slightly shifted to higher or lower elution volume (approx. ±1 ml). Mic19 mutants showed a monomer dimer distribution (Figure 18 D). The SEC profile of Mic19_R126A superimposes well with that of Mic19. The peaks of the other mutants are slightly shifted to lower elution volume (approx. 3 ml) demonstrating a higher hydrodynamic radius. Mass spectrometry analysis (Appendix E) showed that the disulfide bond within

the CHCH domain is formed in Mic19, as the calculated and the measured molecular mass show a difference of exactly 2 Da. Interestingly, these results also reveal that the disulfide bond is formed in all Mic19 mutants.

Thus, $Mic60_{sol}$ and Mic19 constructs were successfully expressed and purified and were used for further analysis.

5.5.2. Biochemical characterization of the Mic60-Mic19 interface

To get an initial impression of the Mic60-Mic19 interaction of the mutants, blue native PAGE analysis was performed (see 4.3.3). Mic19 (19.6 kDa) ran as smear between 20 kDa and 66 kDa (Figure 19 A), although only the monomer peak was pooled after SEC. $Mic60_{sol}$ (54.4 kDa) ran predominantly as a dimer on blue native PAGE, even though additional bands likely referring to a tetramer and octamer could also be observed (Figure 19 A, Hessenberger et al., 2017). After incubation of $Mic60_{sol}$ and Mic19, they form a complex, resulting in the formation of higher-order oligomers; at least three different $Mic60_{sol}$-Mic19 complexes could be observed (Figure 19 A): C1 may constitute a 2:2 Mic60-Mic19 dimer, the predominant C2 a 4:4 Mic60-Mic19 tetramer and C3 an even higher oligomer. As Mic19 was added in slight excess, a small portion of Mic19 oligomers is still present on the gel in the low molecular mass range, not involved in complex formation.

In the same way, the mutants were incubated with either $Mic60_{sol}$ or Mic19 and analyzed using blue native PAGE (Figure 19 B, Figure 20). Complexes containing $Mic60_{sol}$_Q674A or Mic19_R126A oligomerize similarly to wild-type $Mic60_{sol}$-Mic19. Interestingly, hydrophobic mutants ($Mic60_{sol}$_V678D, $Mic60_{sol}$_L685D, Mic19_V129D, Mic19_L133D, Mic19_F150D) show a different oligomerization pattern: Most of the protein bands refer to $Mic60_{sol}$ (three prominent bands) and Mic19, which are not involved in complex formation. Furthermore, only a small portion of protein appears as high molecular weight complex 2 and 3 (Figure 19).

It can be concluded that in particular mutations in the hydrophobic interface lead to disturbance of complex formation between Mic60 and Mic19. Furthermore, these data support the assumption that the Mic60-Mic19 interface observed in the Mitofilin_C-CHCH domain construct represents the interface also in the full-length proteins.

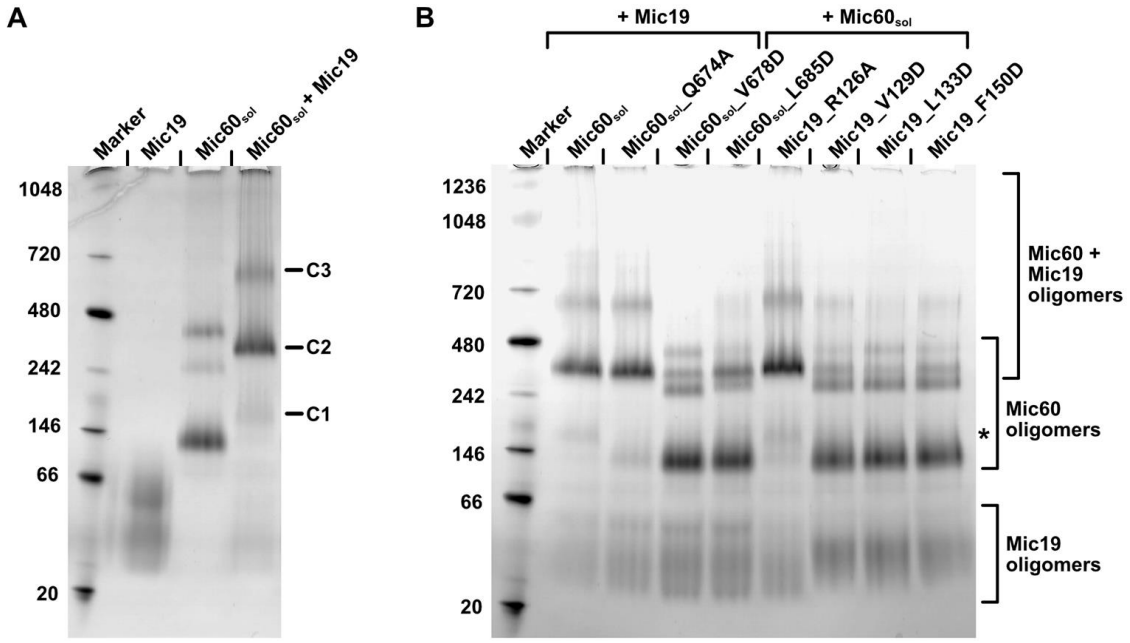

Figure 19: Blue native PAGE analysis of Mic60$_{sol}$ and Mic19 constructs. 4-16% Bis-Tris gels stained with Coomassie Brilliant Blue; Marker: NativeMark™ Unstained Protein Standard. Numbers next to marker indicate the MW in kDa. **(A)** Mic19, Mic60$_{sol}$ and complex formation. C1: complex 1 (likely 2x Mic60, 2x Mic19), C2: complex 2 (likely 4x Mic60, 4x Mic19), C3: complex 3. **(B)** Complex formation of Mic19, Mic60$_{sol}$ and interaction interface mutants. The asterisk indicates the position of C1.

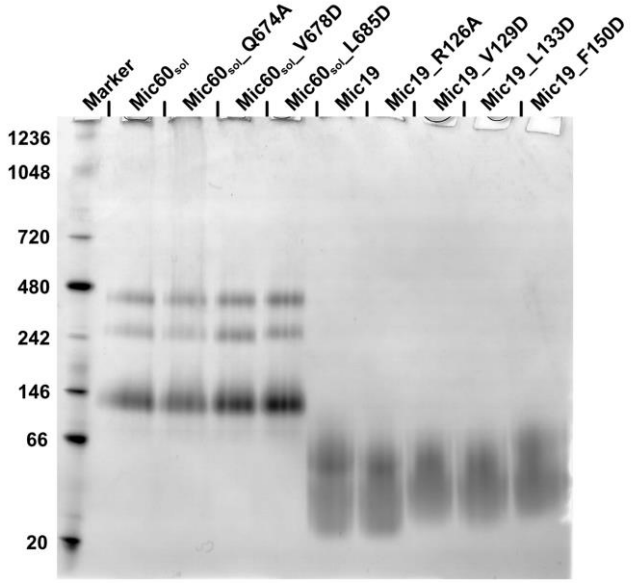

Figure 20: Blue native PAGE analysis of single Mic60$_{sol}$ and Mic19 constructs. 4-16% Bis-Tris gels stained with Coomassie Brilliant Blue; Marker: NativeMark™ Unstained Protein Standard. Numbers next to the marker indicate the MW in kDa. MW of Mic60$_{sol}$: 54.4 kDa, and Mic19: 19.6 kDa.

To obtain quantitative data, the $Mic60_{sol}$-Mic19 interaction was analysed by isothermal titration calorimetry (ITC), where Mic60 was placed in the sample cell and Mic19 in the syringe (details in 4.3.10.). In agreement with Hessenberger et al. (2017) a K_D value of 190 nM ± 20 nM was obtained for wild-type protein, demonstrating a high affinity interaction (Figure 21 A). The binding number of 0.73 indicated that only 73% of $Mic60_{sol}$ interacted with Mic19.

Analogous to the wild-type proteins, the different mutants of $Mic60_{sol}$ and Mic19 were analyzed in ITC experiments, and the results are shown in Figure 21 and Figure 22. Protein concentrations of mutants were adapted according to the ITC signal. Interestingly, $Mic60_{sol}$_Q674A + Mic19 and Mic19_R126A + $Mic60_{sol}$ showed moderately reduced K_D values (approx. 10x reduced K_D), although the oligomerization on blue native PAGE was similar to wild-type $Mic60_{sol}$-Mic19 (compare Figure 19 B and Figure 21). In agreement with blue native PAGE analysis, only a very weak signal was obtained for $Mic60_{sol}$_V678D, leading to a K_D of 11000 nM ± 5000 nM (Figure 21 D). This is 60x reduced in comparison to wild-type. Furthermore, the reaction shows exothermic behaviour, while wild-type, $Mic60_{sol}$_Q674A and Mic19_R126A showed a predominantly endothermic reaction.
For the mutants Mic19_V129D, Mic19_L133D, Mic19_F150D and $Mic60_{sol}$_L685D, no binding could be detected via ITC (Figure 22), although formation of higher-order complexes was observed to a small degree using blue native PAGE (Figure 19 B).

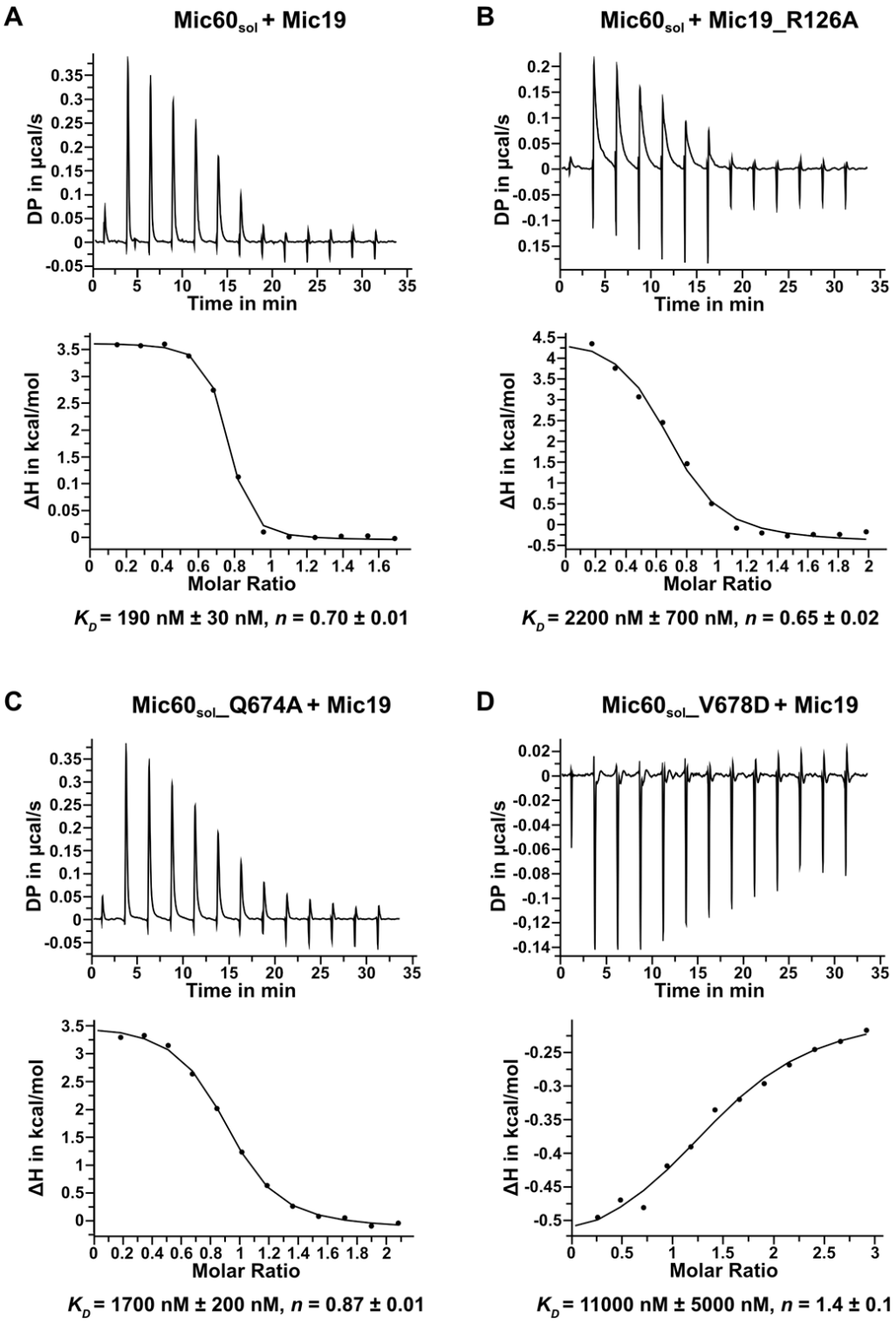

Figure 21: ITC experiments using Mic60$_{sol}$, Mic19 and mutants showing reduced binding. Mic19 (or mutant) was titrated into Mic60$_{sol}$ (or mutant) at 10 °C, and resulting heat changes were monitored. Molar Ratios indicate Mic19/Mic60. **(A)** 45 µM Mic60$_{sol}$, 391 µM Mic19, fitted values: K_D = 190 nM ± 30 nM, binding number n = 0.70 ± 0.01. **(B)** 46 µM Mic60$_{sol,}$ 475 µM Mic19_R126A, K_D = 2200 nM ± 700 nM, n = 0.65 ± 0.02. **(C)** 45 µM Mic60$_{sol}$_Q674A, 488 µM Mic19, K_D = 1700 nM ± 200 nM, n = 0.87 ± 0.01. **(D)** 44 µM Mic60$_{sol}$_V678D, 658 µM Mic19, K_D = 11000 nM ± 5000 nM, binding number n = 1.4 ± 0.1.

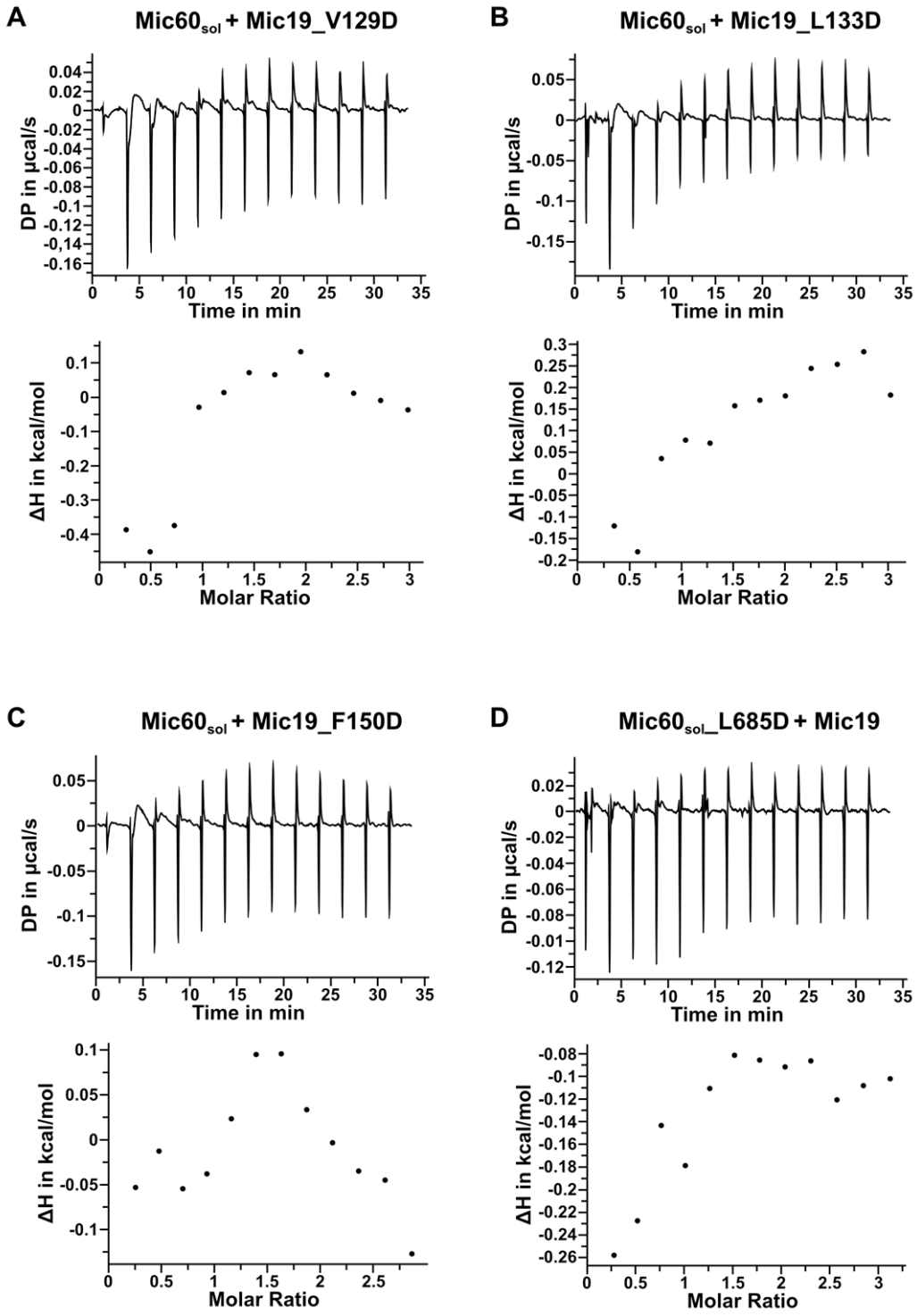

Figure 22: ITC experiments using $Mic60_{sol}$, Mic19 and mutants showing no binding. Mic19 (or mutant) was titrated into $Mic60_{sol}$ (or mutant) at 10 °C, and the resulting heat changes were monitored. Molar Ratios indicate Mic19/Mic60. **(A)** 45 µM $Mic60_{sol}$, 700 µM Mic19_V129D. **(B)** 45 µM $Mic60_{sol}$, 683 µM Mic19_L133D. **(C)** 45 µM $Mic60_{sol}$, 673 µM Mic19_F150D. **(D)** 50 µM $Mic60_{sol}$_L685D, 809 µM Mic19.

In a third approach, a liposome co-sedimentation assay was used to analyze the Mic60-Mic19 interaction. $Mic60_{sol}$ was shown to bind to liposomes *in vitro*, while Mic19 does not co-sediment with liposomes (Hessenberger et al., 2017). However, after $Mic60_{sol}$-Mic19 complex formation, Mic19 co-sediments with liposomes due to binding to Mic60.

According to an optimized protocol (see 4.3.12), Folch lipids from bovine brain were used and prepared. Mic60 and Mic19 were incubated with liposomes and co-sedimented by ultracentrifugation (details in 4.3.13.). Subsequently, protein content obtained in the supernatant (SN) and the pellet (P) fractions was quantified. Only hydrophobic mutants were considered for further analysis.

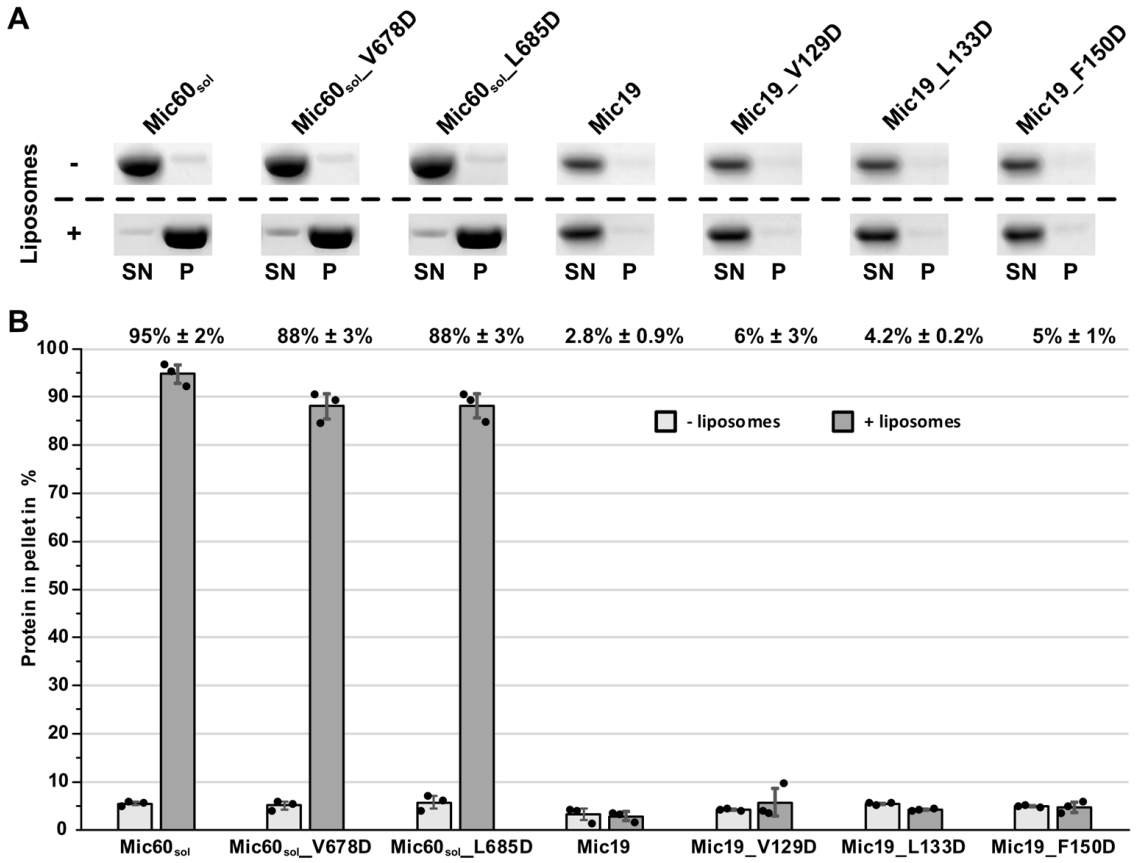

Figure 23: Liposome co-sedimentation assays using $Mic60_{sol}$, Mic19 and mutants of both. (A) 4-12% SDS-PAGE gel cuttings stained with Coomassie Brilliant Blue. Experiments were performed in the absence (-) or presence (+) of liposomes. SN: supernatant after centrifugation; P: pellet. **(B)** Quantification of liposome co-sedimentation assays using *ImageJ* (Schneider et al., 2012). The bars indicate the average percentage of protein in P with respect of the total protein applied on the gel (SN + P = 100%). The calculated standard deviations are shown. Dots represent the results of three independent experiments. The numbers above the bars show the calculated values for pellet fractions in presence of liposomes.

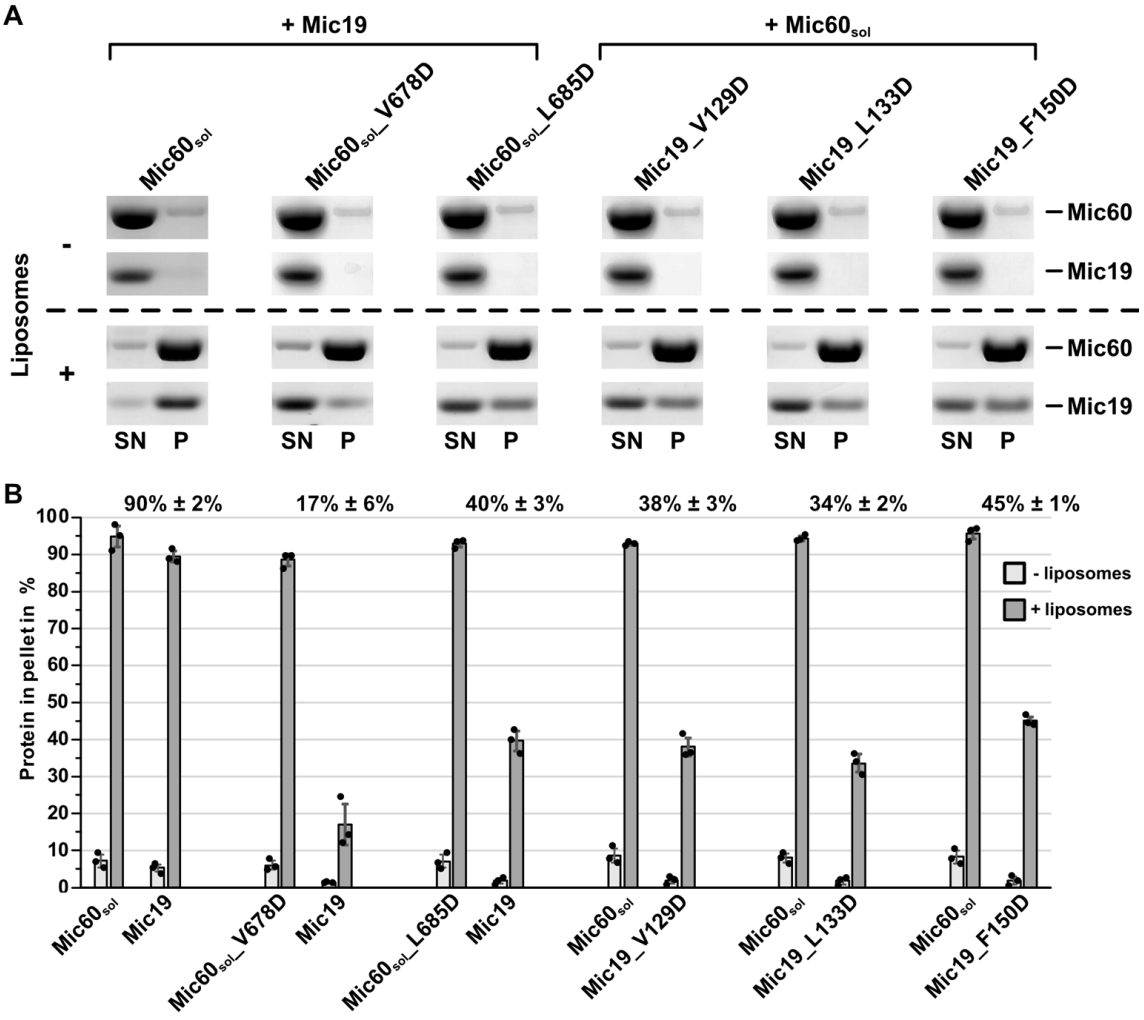

Figure 24: Liposome co-sedimentation assays to analyze co-sedimentation of Mic19 and mutants of both. (A) 4-12% SDS-PAGE gel cuttings stained with Coomassie Brilliant Blue. $Mic60_{sol}$ and Mic19 constructs were incubated in the absence (-) or presence (+) of liposomes. SN: supernatant after centrifugation; P: pellet. **(B)** Quantification of liposome co-sedimentation assays using *ImageJ* (Schneider et al., 2012). The bars indicate the average percentage of protein found in the pellet with respect of the total protein applied on the gel (SN + P = 100%). The calculated standard deviations are shown and the dots represent the results of three independent experiments. The numbers above the bars show the calculated values for the pellet fraction of the respective Mic19 construct in presence of liposomes.

In agreement with Hessenberger et al., 2017, $Mic60_{sol}$ efficiently co-sedimented with liposomes (Figure 23). In contrast, Mic19 on its own and Mic19 mutants do not co-sediment with liposomes (Figure 23). When both proteins were co-incubated with liposomes, Mic60 dragged Mic19 into the pellet (Figure 24).

$Mic60_{sol}$_V678D and $Mic60_{sol}$_L685D showed efficient similar liposome binding to $Mic60_{sol}$ (Figure 23). However, the mutants did not efficiently recruit Mic19 to the pellet

fraction (Figure 24). Also the Mic19 mutations in V129, L133 and F150 led to reduced co-sedimentation with Mic60.

These results reveal the importance of the hydrophobic residues V678, L685 from Mic60 and V129, L133, F150 from Mic19 in the Mic60-Mic19 interaction. Notably, these residues are highly conserved in higher eukaryotes (Figure 25).

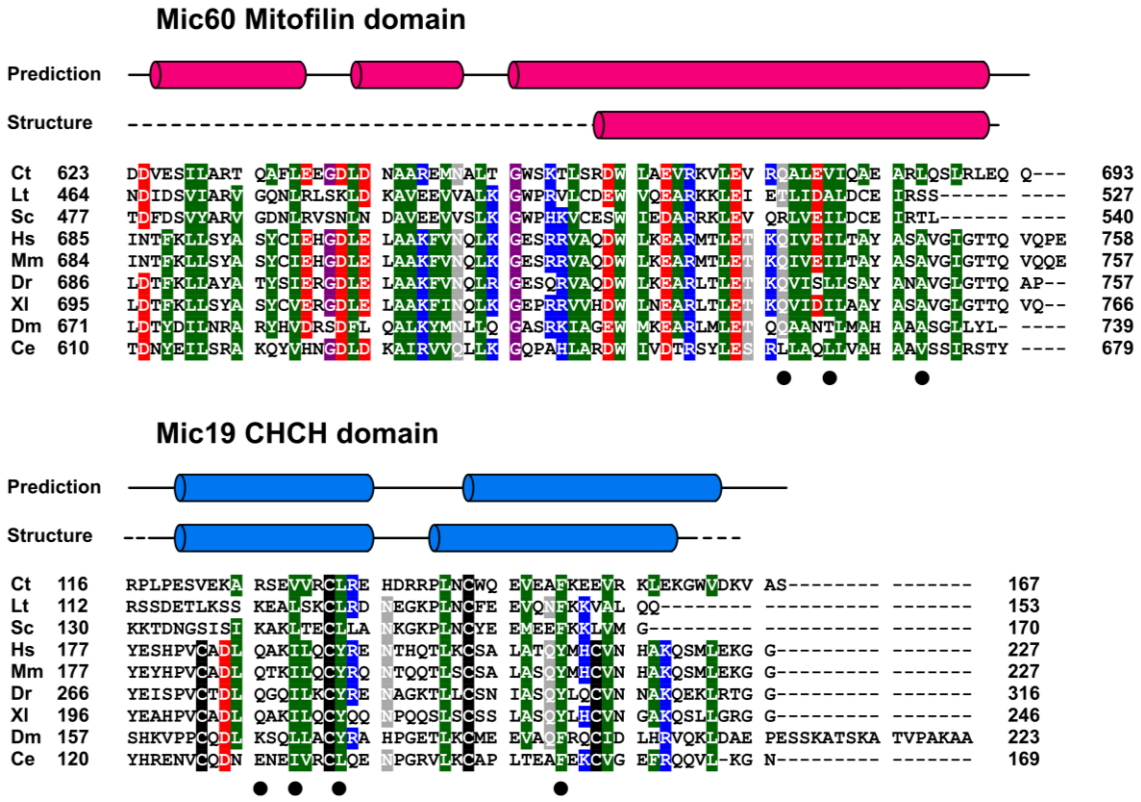

Figure 25: Secondary structure of mitofilin and CHCH domain and sequence alignment. Secondary structure of mitofilin and CHCH domain is depicted according to the crystal structure of Mitofilin_C-CHCH and *PSIPRED* prediction (Buchan and Jones, 2019; see Appendix C). Cylinders represent α-helices and a dashed line indicates that residues could not be modeled in the crystal structure. Mic60 and Mic19 from different species were aligned using *Clustal Omega* (Sievers et al., 2011) and manually refined; UniProtID in parentheses; Ct: *C. thermophilum*, Mic60 (G0SHY5), Mic19 (G0S140); Lt: *Lacchancea thermotolerans*, Mic60 (C5E325), Mic19 (C5E3G4); Sc: *Saccharomyces cerevisiae*, Mic60 (P36112), Mic19 (P43594); Hs: *Homo sapiens*, Mic60 (Q16891), Mic19 (Q9NX63); Mm: *Mus musculus*, Mic60 (Q8CAQ8), Mic19 (Q9CRB9); Dr: *Danio rerio*, Mic60 (Q6PFS4), Mic19 (Q502T3); Xl: *Xenopus laevis*, Mic60 (A0A1L8HT59), Mic19 (Q6GQ87); Dm: *Drosophila melanogaster*, Mic60 (P91928), Mic19 (Q24269); Ce: *Caenorhabditis elegans*, Mic60, (Q22505), Mic19 (Q21551). Numbers represent borders of mitofilin or CHCH domain. A lack of the corresponding residue is indicated by a stroke. Residues with a conservation greater than 66% (6/9) are colored in red (D, E), blue (H, K, R), green (A, F, I, L, M, V, W, Y), purple (G, P), black (C) or grey (N, Q, S, T). The dots below the sequences indicate residues, which were mutated in this study.

Altogether, a detailed biochemical analysis using a combination of blue native PAGE, ITC and liposome co-sedimentation assays led to the identification of several residues critical for the integrity of the Mic60-Mic19 complex, emphasizing the importance of hydrophobic contacts.

5.6. *In vivo* characterization of the Mic60-Mic19 interaction

To investigate the physiological effect of the Mic60-Mic19 interaction on mitochondrial membrane architecture, *Saccharomyces cerevisiae* (sc) strains expressing the corresponding scMic60 or scMic19 single-point mutants were generated:
ctMic60_V678D: scMic60_I532D,
ctMic60_L685D: scMic60_T539D,
ctMic19_V129D: scMic19_L143D,
ctMic19_L133D: scMic19_L147D,
ctMic19_F150D: scMic19_F164D.

This analysis took advantage of the fact that most of the mutated residues are conserved within different species (Figure 25).

Cloning of yeast constructs and protein level analysis were performed by Florian Wollweber, Janina Laborenz and Sibylle Jungbluth (Universität des Saarlandes). scMic60 or scMic19 knockout strains (*mic60*Δ or *mic19*Δ) were rescued by over-expression of wild-type or mutant scMic60 or scMic19 constructs from a plasmid. Mitochondrial ultrastructures of wild-type, rescue and mutant strains were analyzed by electron microscopy by Elisa Lisicki at the MDC. Representative electron micrographs of mutant yeast and their mitochondria are shown in Figure 26. Crista junctions per mitochondrial section were quantified as shown in Figure 27 (n = 100 mitochondrial cross sections).

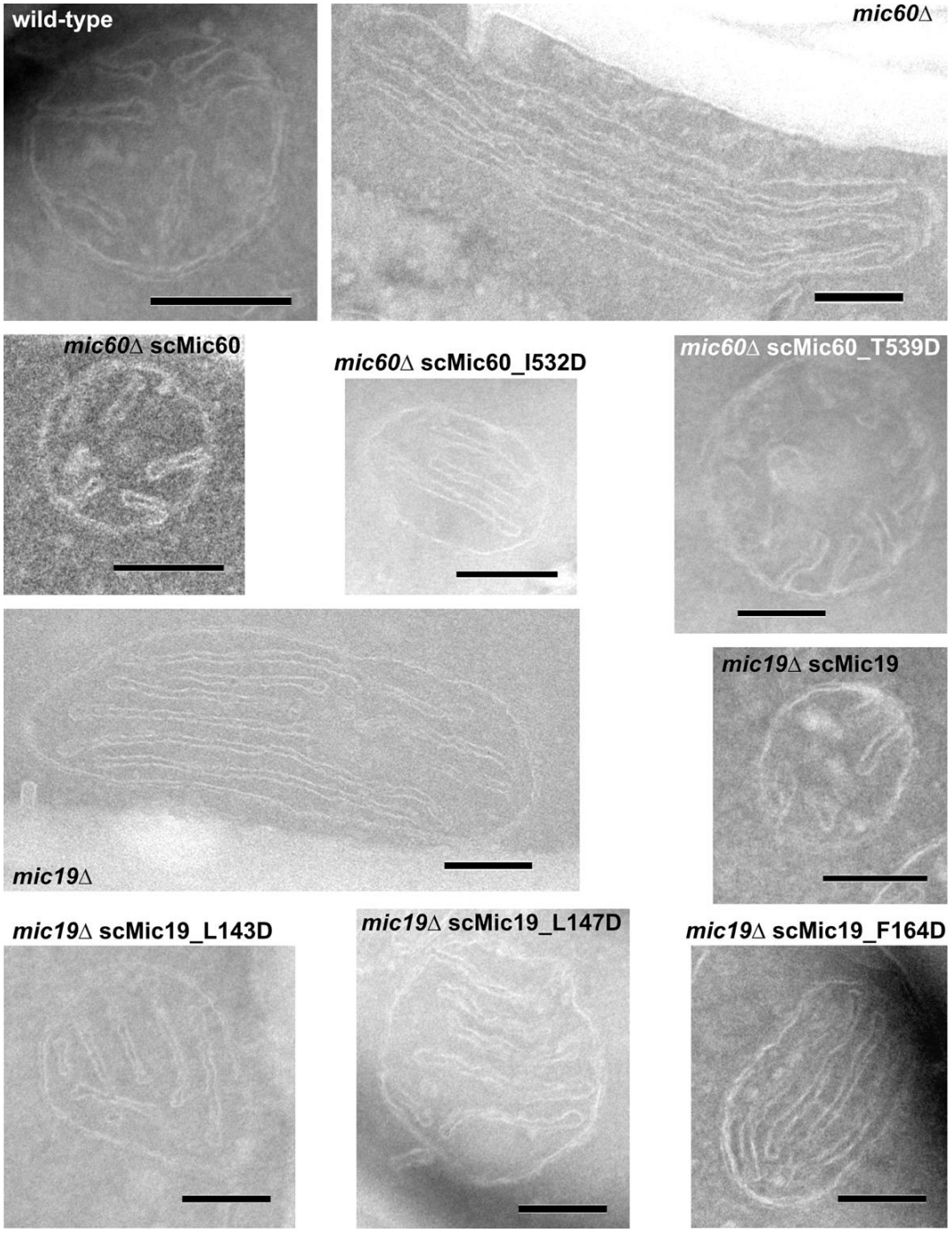

Figure 26: Analysis of yeast mitochondria in wild-type and mutants. *Saccharomyces cerevisiae* (sc) Mic60 or Mic19 knockout strains (*mic60*Δ or *mic19*Δ) were rescued by over-expression of mutant scMic60 or scMic19 from a plasmid to generate strains expressing scMic60 or scMic19 single-point mutants (empty vector in case of knockout and wild-type). Corresponding *Chaetomium thermophilum* (ct) constructs in parentheses; scMic60_I532D (ctMic60_V678D), scMic60_T539D (ctMic60_L685D), scMic19_L143D (ctMic19_V129D), scMic19_L147D (ctMic19_L133D), scMic19_F164D (ctMic19_F150D). Mitochondrial ultrastructures were analyzed by electron microscopy. Scale bar indicates 200 nm. Cloning of yeast constructs was performed by Florian Wollweber and Sibylle Jungbluth (Universität des Saarlandes). Experiments were performed by Elisa Lisicki at the MDC.

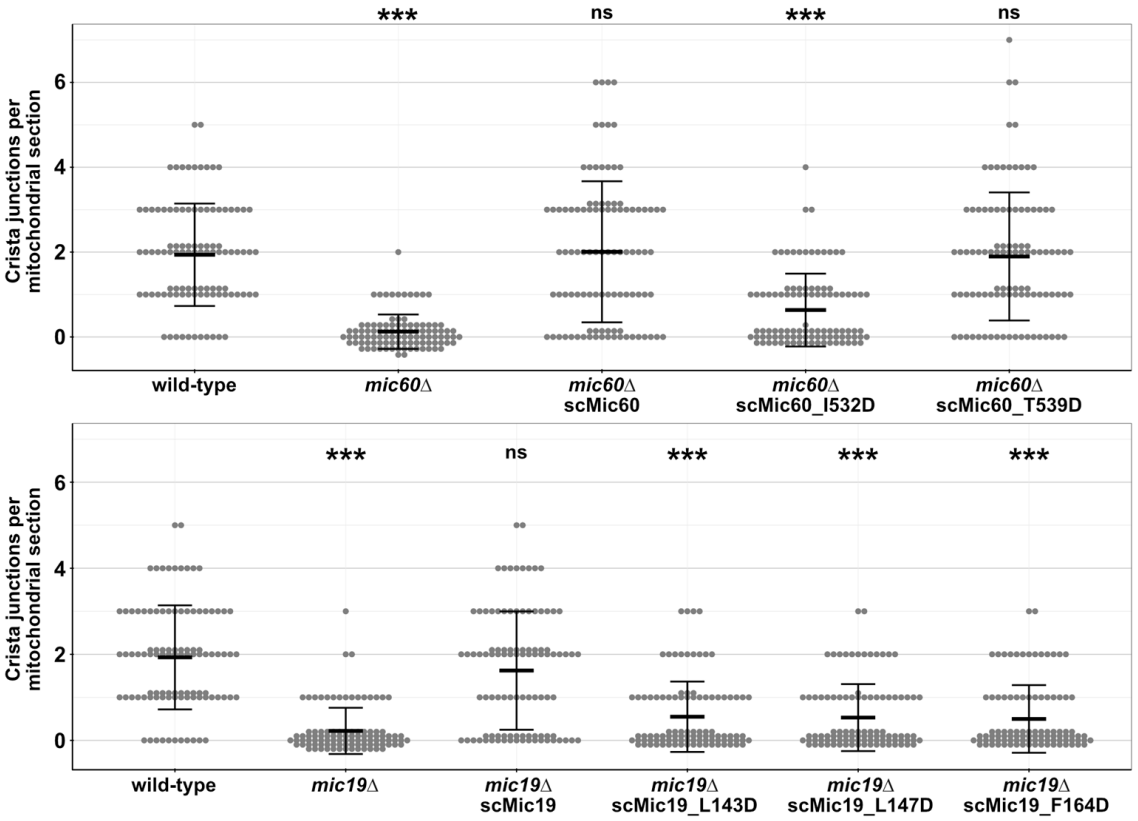

Figure 27: Quantification of crista junctions in wild-type and mutant mitochondria. *S. cerevisiae* (sc) Mic60 or Mic19 knockout strains (*mic60*Δ or *mic19*Δ) were rescued by over-expression of wild-type or mutant scMic60 or scMic19 from a plasmid (empty vector in case of knockout and wild-type). The following single-point mutants were generated (corresponding *Chaetomium thermophilum* (ct) constructs in parentheses): scMic60_I532D (ctMic60_V678D), scMic60_T539D (ctMic60_L685D), scMic19_L143D (ctMic19_V129D), scMic19_L147D (ctMic19_L133D), scMic19_F164D (ctMic19_F150D). Quantification of crista junctions per mitochondrial section; n = 100 mitochondrial cross sections were analyzed for all groups. Differences of $p \leq 0.05$ were considered significant ($p \leq 0.05$*,$p \leq 0.01$**, $p \leq 0.001$***) compared to wild-type and the test statistic W is reported; ns: no significance (see also Figure 26). Cloning of yeast constructs was performed by Florian Wollweber and Sibylle Jungbluth (Universität des Saarlandes). Experiments and quantification were performed by Elisa Lisicki at the MDC.

The number of crista junctions per mitochondrial section varies between zero and seven in all analyzed mitochondria (Figure 27). Wild-type mitochondria as well as scMic60 rescue and scMic19 rescue obtain approximately two crista junctions on average. Deletion of *mic60* or *mic19* resulted in almost complete absence of crista junctions, where the cristae membrane is detached from the inner boundary membrane

and forms internal membrane stacks (Figure 26). Mitochondria of most of the single-point mutants show a significantly reduced number of crista junctions and phenotypes close to *mic60*Δ or *mic19*Δ, pointing to the importance of these residues in cristae morphology. Only scMic60_T539D showed a similar mitochondrial morphology compared to wild-type. However, this residue is only partial conserved (T in sc, L in ct, Figure 25) and is situated at the very C-terminus. In this case, the interaction between the mitofilin domain and the CHCH domain might be slightly altered in yeast compared to *Chaetomium*.

Analysis of the protein levels in mitochondria revealed that levels of scMic19_L143D and scMic19_L147D were strongly reduced in comparison to wild-type (Figure 28 A). scMic19_F164D could not be detected, as F164 is part of the epitope recognized by the used antibody. Deletion of Mic19 resulted in reduced levels of Mic60, as reported previously for different organisms (von der Malsburg et al., 2011; Harner et al., 2011; Hoppins et al., 2011; Li et al., 2016; Ott et al., 2015; Darshi et al., 2011; Sakowska et al., 2015). Similar observations of reduced scMic60 levels were observed for all analyzed scMic19 mutants (L143D, L147D and F164D).
Protein level analysis of scMic60_I532D and scMic60_T539D is shown in Figure 28 B, indicating that expression of scMic60_T539D is similar to scMic60 rescue, while scMic60_I532D expression is slightly reduced. Mic19 levels are also similar in scMic60 rescue and scMic60_T539D. For scMic60_I532D, it seems that reduced amounts of Mic19 were detected, while deletion of Mic60 resulted in strongly reduced Mic19 levels. These results are in line with the observation that mitochondria of scMic60_T539D appear as in wild-type or Mic60 rescue (Figure 26, Figure 27).

Changes in cristae morphology (Figure 26, Figure 27) might be a consequence of reduced Mic60/Mic19 protein levels. However, Mic60 and Mic19 steady-state protein levels are mutually dependent and interaction between Mic60 and Mic19 was reported to cover a protease recognition site of Mic60 (Li et al., 2016). Therefore, reduced protein levels, as observed for scMic19_L143D, scMic19_L147D, scMic19_F164D and scMic60_I532D, point to disturbed scMic60-scMic19 interactions, which is in line with the *in vitro* results from *Chaetomium thermophilum*. However, these data need to be further validated.

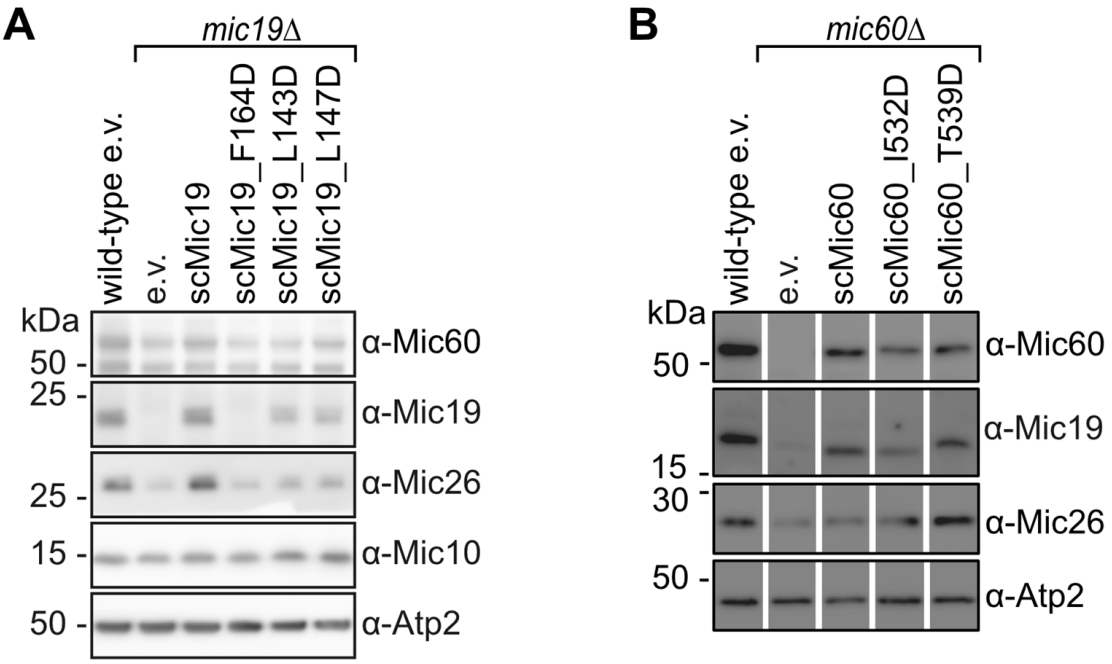

Figure 28: Protein levels analysis of wild-type and mutant mitochondria. Samples were analyzed by SDS-PAGE and western blot with polyclonal antibodies against MICOS subunits, and Atp2 as sample processing control; e.v.: empty vector. **(A)** scMic19_F164D: ctMic19_F150D, scMic19_L143D: ctMic19_V129D, scMic19_L147D: ctMic19_L133D. **(B)** scMic60_I532D: ctMic60_V678D, scMic60_T539D: ctMic60_L685D. Cloning of yeast constructs and experiments were performed by Florian Wollweber, Janina Laborenz and Sibylle Jungbluth (Universität des Saarlandes).

The analyzed residues and their positions in the crystal structure are depicted in Figure 29 and an overview of the performed *in vitro* and *in vivo* experiments is shown in Table 9.

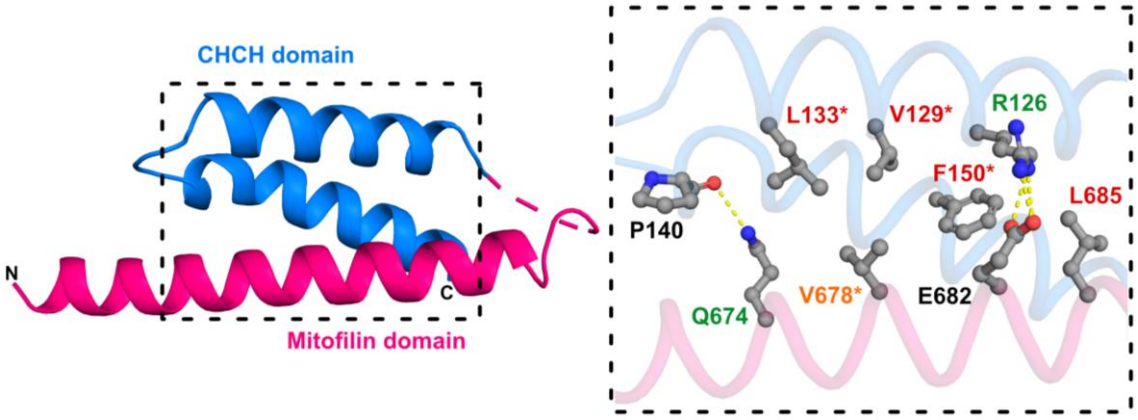

Figure 29: Monomer structure of Mitofilin_C-CHCH and interaction interface. Monomer (chain A) shown in ribbon representation. Domains are colored individually and termini are labelled. The linker region is not resolved in the crystal structure and indicated by a dashed line (pink). Black dashed rectangle indicates the Mic60-Mic19 interface shown in detail. Selected residues involved in the interaction are shown and labelled. The label of analyzed mutants is colored according to results shown in Table 9; up to 15x reduced binding in ITC (green), up to 100x reduced binding in ITC (orange), no binding in ITC (red); cristae morphology (sc) similar to knockout is marked by an asterisk.

Table 9: **Overview of blue native PAGE, ITC, liposome co-sedimentation assay and cristae morphology results for Mic60-Mic19 interaction interface mutants.** For some constructs, no binding could be calculated via ITC (–).

$Mic60_{sol}$ + Mic19 (or mutant)	Blue native PAGE, high-order oligomers	ITC, K_D in nM		Liposome co-sedimentation, Mic19 in pellet in %		Cristae morphology in correspond. yeast mutants
Wild-type	yes	190 ± 30		90 ± 2		
$Mic60_{sol}$_Q674A	yes	1700 ± 200	9x reduced			
$Mic60_{sol}$_V678D	no	11000 ± 5000	58x reduced	17 ± 6	5x reduced	Like knockout
$Mic60_{sol}$_L685D	no	–		40 ± 3	2x reduced	Like wild-type
Mic19_R126A	yes	2200 ± 700	12x reduced			
Mic19_V129D	no	–		38 ± 3	2x reduced	Like knockout
Mic19_L133D	no	–		34 ± 2	3x reduced	Like knockout
Mic19_F150D	no	–		45 ± 1	2x reduced	Like knockout

5.7. Design and purification of extended constructs containing LBS, mitofilin domain and CHCH domain

The mitofilin domain is the most conserved domain of Mic60 (Rabl et al., 2009; von der Malsburg et al., 2011; Körner et al., 2012; Zerbes et al., 2012). However, the crystallized construct Mitofilin_C-CHCH (after trypsin digestion) did not contain the full mitofilin domain (Figure 25). Thus, I tried to include additional parts of Mic60 to prolong the construct. Two predicted helices between the coiled-coil domain and the mitofilin domain of Mic60 were shown to be able to bind to liposomes and remodel them, independent of Mic60 transmembrane region (Hessenberger et al., 2017, see also Appendix C). This region is referred to lipid binding site (LBS) and the corresponding predicted helices LBS1 and LBS2. However, so far no structural information about this region and the membrane binding mechanism could be obtained.

To get structural information about the LBS of Mic60, Jeffrey Noel (MDC) applied co-evolutionary coupling analyses from sequence alignments for structure prediction (Hopf et al., 2019). In the resulting prediction, LBS1 was positioned in close proximity to the mitofilin domain (Figure 30) and formed with three helices a four-helix bundle (Figure 30 B). Moreover, the model reveals a long unstructured region between LBS and the mitofilin domain (brown), which might hinder proper crystal formation.

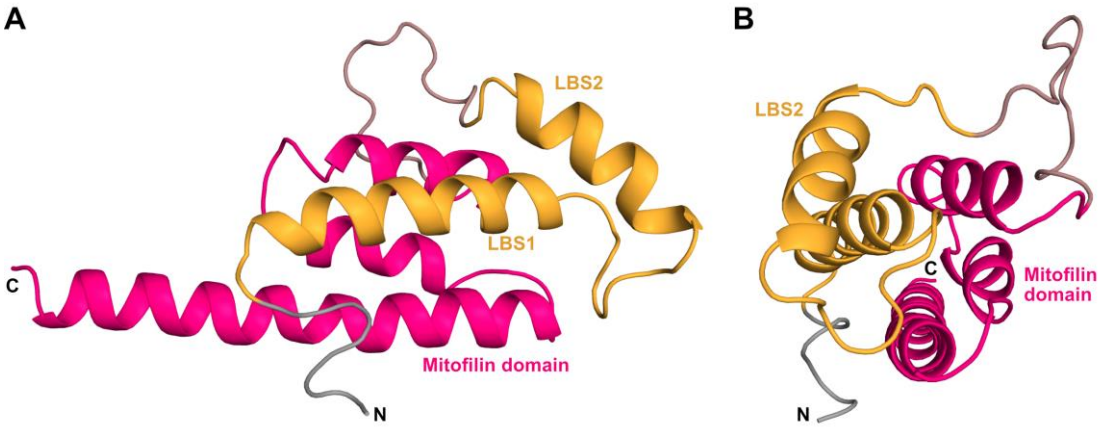

Figure 30: Structure prediction of Mic60. (A) Structure prediction of *Chaetomium thermophilum* Mic60 (residues 557-685) comprising the lipid binding site (LBS, orange) and the mitofilin domain (pink) in a side view. N- and C-termini and the two α-helices of LBS (LBS1, LBS2) are labelled. The unstructured loop region between the LBS and the mitofilin domain is colored in brown. Designed constructs used in this study do not contain the unstructured N-terminus (grey). Structure prediction derived from the *EVolutionary Couplings Server* (Hopf et al., 2019). **(B)** Structure as in (A) 90 ° turned clockwise (y-axis).

According to this prediction, I used new strategies for construct design (Figure 31). On the one hand, I fused LBS1 directly to Mitofilin_C-CHCH (Figure 31 C). An appropriate linker length between LBS1 and the mitofilin domain appeared required for the formation of the four-helix bundle. Thus, different linker lengths were designed by using repetitive glycine-serine (GS) stretches. On the other hand, the unstructured region between LBS2 and the mitofilin domain (Figure 30, brown) was removed and the remaining protein parts were connected via a variable GS linker (Figure 31 D). Furthermore, a construct containing the complete LBS and the mitofilin domain without deletion was designed (Figure 31 E). To maintain solubility, all constructs also included the CHCH domain of Mic19.

These new constructs were expressed and purified via Ni-NTA and SEC as described for Mitofilin_C-CHCH (see 5.1). The SEC profiles of the constructs are shown in Figure 31. Depending on the construct, yields of soluble protein between 2 mg and 30 mg protein per liter bacteria culture could be obtained after SEC. Only construct Mitofilin-CHCH_3 could be concentrated up to 18 mg/ml, all other proteins started to precipitate upon concentration.
The constructs combining LBS1 with Mitofilin_C-CHCH (Figure 31 C/F) led to highest yields, and reasonable concentrations for crystallization trials could be obtained. Moreover, the main peak of the SEC profile appears sharp and symmetric, assuming a single conformational species.

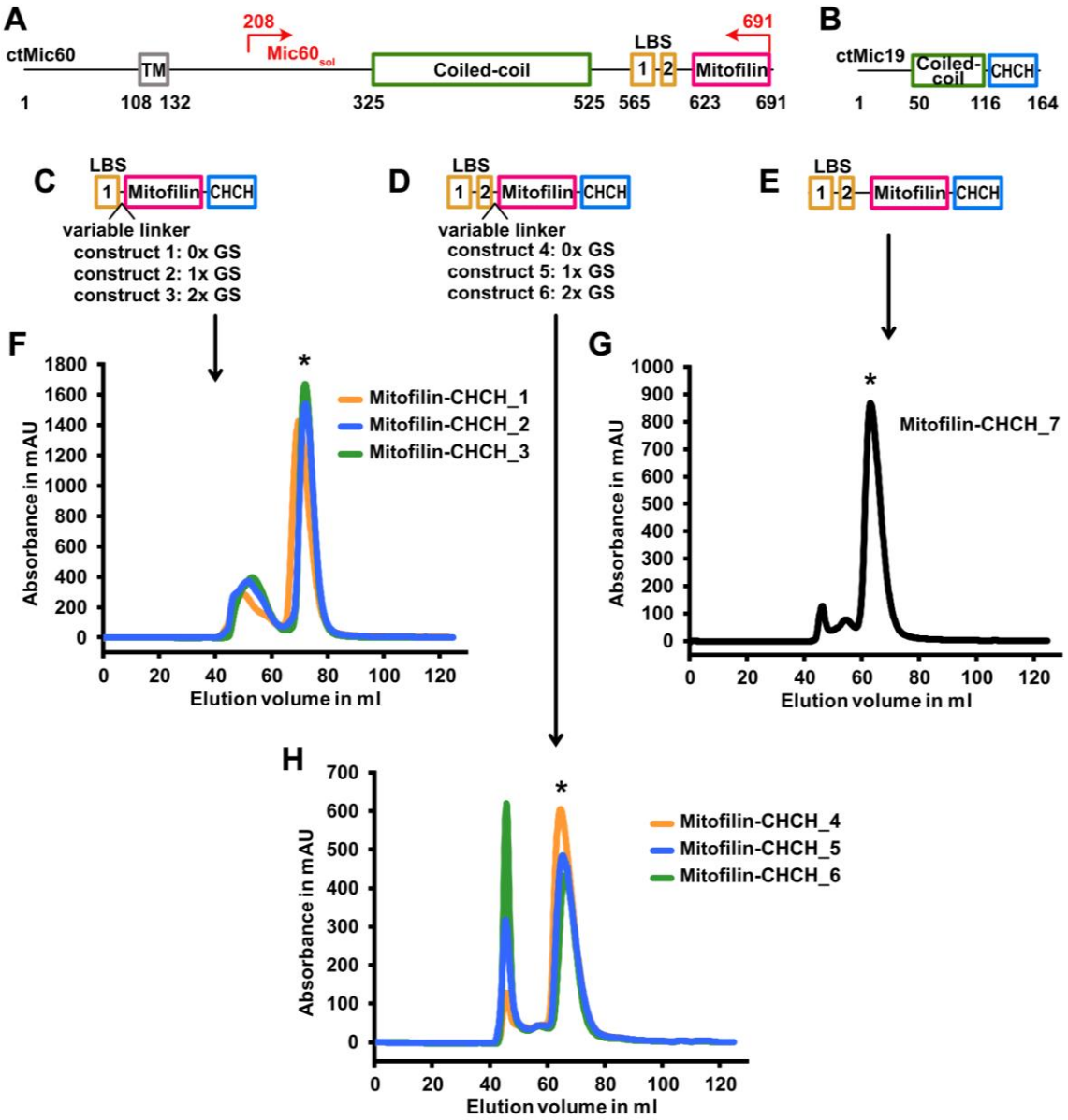

Figure 31: New constructs and SEC purifications. (A), **(B)** Schematic representation of the ctMic60 and the ctMic19 domain structure as shown in Figure 10; created based on *PSIPRED* (Buchan and Jones, 2019; Jones, 1999; see also Table 6 and Appendix C). TM: transmembrane helix, Coiled-coil: coiled-coil domain, LBS: lipid binding site, Mitofilin: mitofilin domain, CHCH: CHCH domain; numbers show the amino acid position; in this study a soluble Mic60 construct $Mic60_{sol}$ was used instead of full-length Mic60; construct borders are labelled. **(C)**, **(D)**, **(E)** Show the three strategies for construct design and the arrows point to the corresponding SEC purification chromatograms: **(F)**, **(G)**, **(H)** An ÄKTApurifier chromatography system connected to a HiLoad 16/600 Superdex 75 pg column (GE Healthcare) was used. Absorption was measured at 280 nm. 1 ml fractions were collected. Asterisks show pooled peaks. Constructs: C: Mic60_565-586-X-622-691-GSGS-Mic19_116-164, D: Mic60_565-607-X-622-691-GSGS-Mic19_116-164, E: Mic60_565-691-GSGS-Mic19_116-164, X = 0x GS or 1x GS or 2x GS; G: glycine, S: serine (see 4.2.12).

5.8. Crystallization and structure determination of the new Mic60-Mic19 fusion constructs

All purified constructs were subjected to crystallization trials (details in section 4.4.2). Crystals of the two constructs Mitofilin-CHCH_2 and Mitofilin-CHCH_3 (Figure 31 C/F) were obtained and optimized (Figure 32). In most cases, crystals grew as plates, but sometimes also cube-shaped crystals were observed. A plate-like crystal of Mitofilin-CHCH_2, derived from the crystal depicted in Figure 32 F, showed the best diffraction.

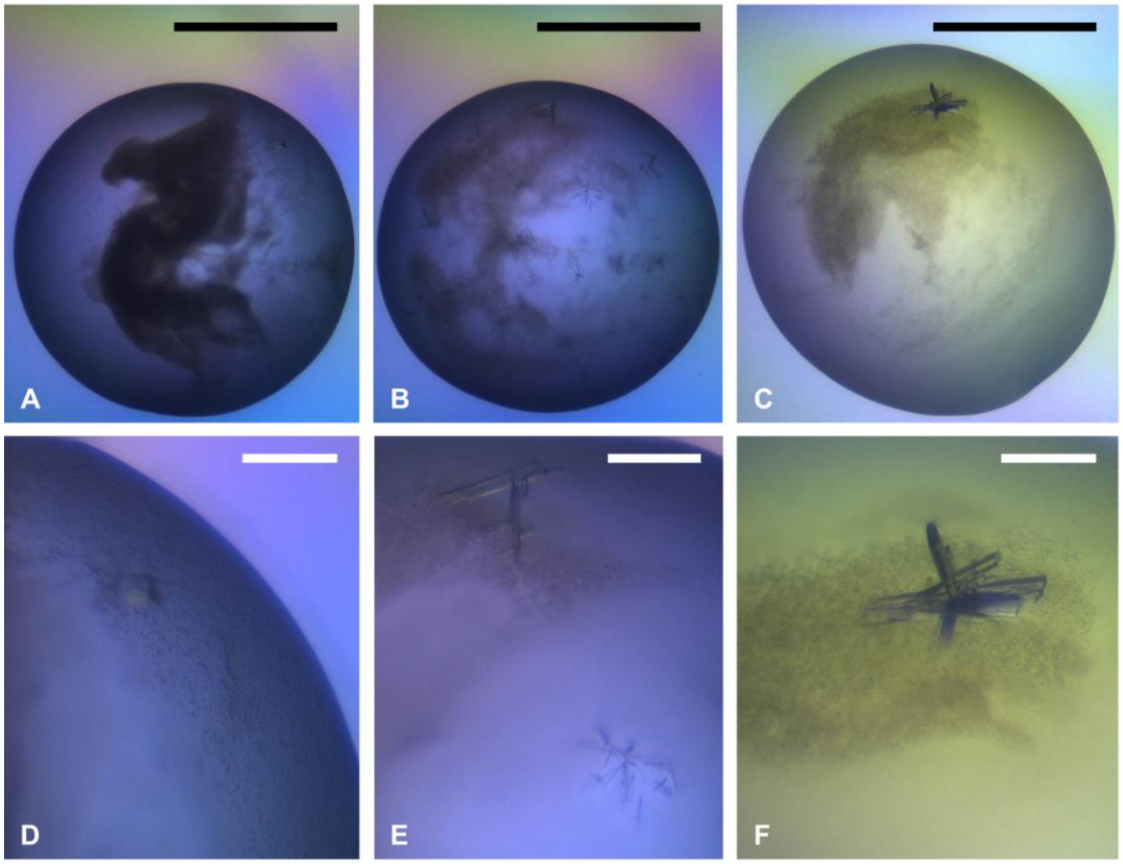

Figure 32: Images of crystals of new fusion constructs. The black scale bar indicates 600 µm and the white scale bar 100 µm. **(A)** Crystals of construct Mitofilin-CHCH_3 obtained in screening condition 20% (w/v) PEG MME 2000, 0.1 M TRIS, pH 8.5, 0.2 M TMANO after 8 days. **(B)** Crystals of construct Mitofilin-CHCH_2 after one day in the same condition as in (A). **(C)** Crystals of construct Mitofilin-CHCH_2 after 4 days in a crystallization solution containing 30% (w/v) Jeffamine ED-2001, 0.1 M HEPES, pH 7.0. **(D)** Magnification of (A). **(E)** Magnification of (B). **(F)** Magnification of (C). The crystal appeared after three days and was fished at the following day (approx. 160 µM x 100 µM); a plate of this crystal diffracted to a resolution of 2.5 Å.

X-ray diffraction data were collected at BESSY II in Berlin (see 4.4.3) and the best crystal diffracted X-rays to a maximum resolution of 2.5 Å (Table 10). The unit cell parameters indicated a high probability for four molecules per asymmetric unit, corresponding to a solvent content of 44% and a Matthews coefficient V_M = 2.19 Å^3/Da (see 4.4.3).

Table 10: **Data collection statistics of Mitofilin-CHCH_2.** Values in parentheses are for highest-resolution shell.

Data collection	
Space group	$P2_1$ (4)
Cell dimensions	
a, b, *c* (Å)	58.20, 85.37, 61.50
α, β, γ (°)	90.00, 101.72, 90.00
Resolution (Å)	49.21 – 2.50 (2.65 – 2.50)
R_{meas} (%)	13.0 (191.1)
I/σI	9.16 (0.75)
Completeness (%)	98.8 (97.7)
Multiplicity	4.0 (4.0)
$CC_{1/2}$ (%)	99.8 (39.4)

The structure was solved by molecular replacement using the structure of Mitofilin_C-CHCH as search model (details in 4.4.4.). In addition to the four protein chains, eight water molecules and three ligands were included in the model. R_{work} = 23.2% and R_{free} = 25.9%, the Ramachandran statistics and the obtained clashscore and rotamer outliers indicate a well refined model (Table 11).

Table 11: **Refinement statistics of Mitofilin-CHCH_2.** Values in parentheses are for highest-resolution shell.

Refinement	
Resolution (Å)	40.74 – 2.50
Total no. of reflections	81,921 (12,949)
R_{work} / R_{free} (%)	23.2 / 25.9
No. of atoms	
Protein	4,394
Ligand	93
Water	8
B-factors (Å^2)	
Protein	79.50
Ligand	95.35
Water	58.92
RMS deviations	
Bond lengths (Å)	0.003
Bond angles (°)	0.58
Ramachandran plot	
Favored (%)	98.70
Allowed (%)	1.30
Outliers (%)	0.00
Rotamer outliers (%)	1.10
Clashscore	4.90

5.9. Crystal structure of the dimeric mitofilin domain

The structure of Mitofilin-CHCH_2 represents four molecules in the asymmetric unit, arranged as two inter-domain swapped dimers (Figure 33). Chain A and chain B form one dimer and chain C and chain D the other dimer. Interestingly, the mitofilin domains within the dimer show a crescent-shaped surface (Figure 33 D). Contacts between the dimers are mediated via the mitofilin domain and the CHCH domain.

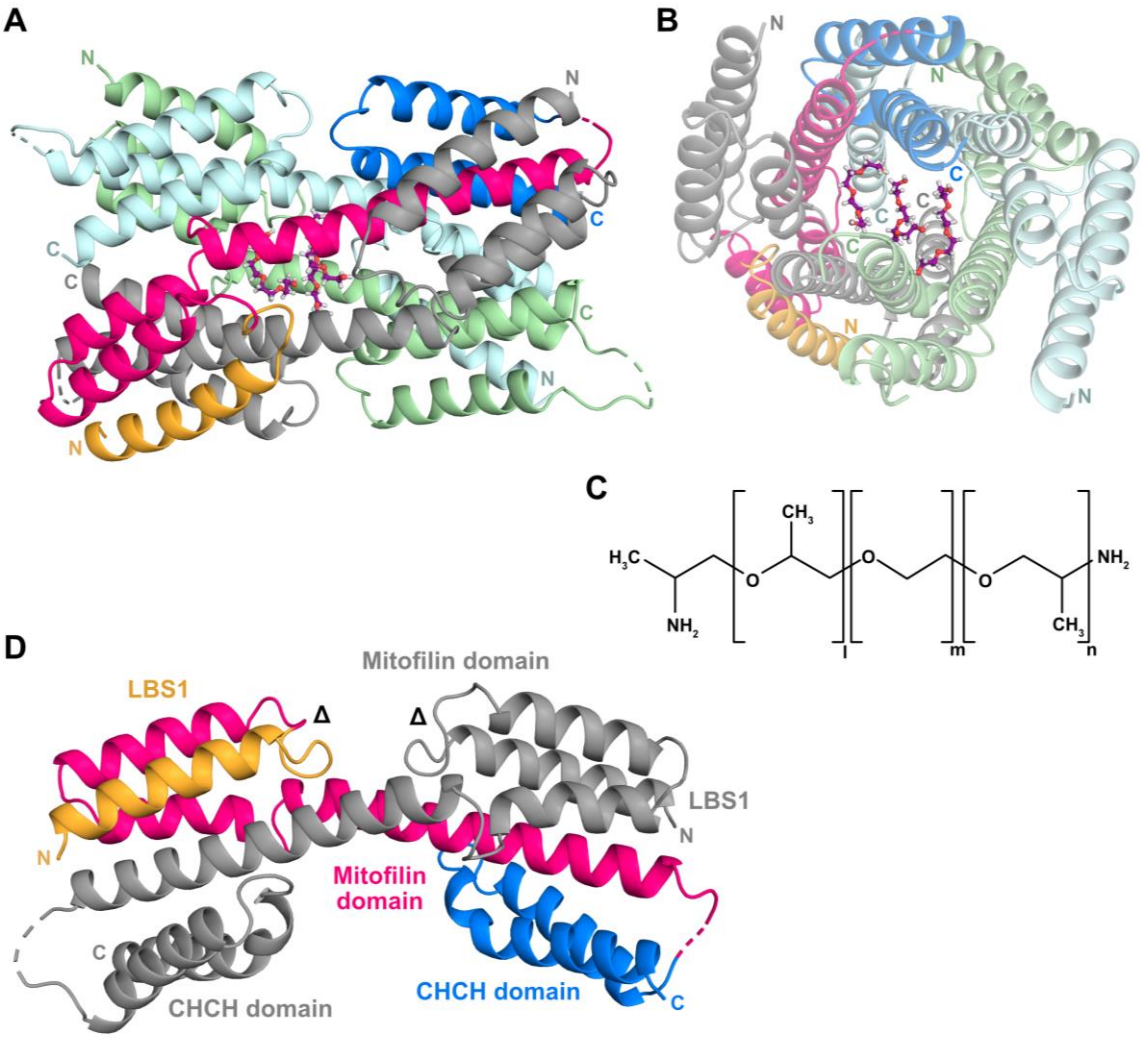

Figure 33: Crystal structure of Mitofilin-CHCH_2 fusion construct. (A) The asymmetric unit contains four molecules, arranged in two dimers. Chains are colored individually and shown in ribbon representation. Chain A: orange (LBS1), pink (mitofilin domain) and blue (CHCH domain), chain B: grey, chain C: cyan, chain D: green. Termini are labelled. The linker region between the mitofilin domain and the CHCH domain is not resolved in the crystal structure and indicated by a dashed line. Three molecules tetraethylene glycol (code: PG4) were built, colored in purple. **(B)** Structure as in (A) 90 ° turned clockwise (y-axis). **(C)** Structural formula of Jeffamine ED-2001 (O,O'-Bis(2-aminopropyl) polypropylene glycol-*block*-polyethylene glycol-*block*-polypropylene glycol), m ≈ 39, (l+n) ≈ 6; derived from JBScreen JCSG++ HTS (Jena Bioscience). **(D)** Dimer composed of chains A and B. The GS linker between LBS1 and the mitofilin domain (removal of LBS2) is indicated by delta (Δ).

The assembly of two dimers results in a cavity, where ligand molecules are present (Figure 33 B). The crystallization solution contained Jeffamine ED-2001, which is composed of different lengths of polypropylene glycol and polyethylene glycol blocks (Figure 33 C). However, polyethylene glycol makes up the majority of Jeffamine ED-2001. Due to ambiguous electron density, three molecules of tetraethylene glycol (three letter code: PG4) were modelled into the density.

In accordance with the secondary structure prediction (Appendix Figure C.3), the monomer of Mitofilin-CHCH_2 comprises six α-helices: LBS1, the three helices of the mitofilin domain ($\alpha1^{M}$-$\alpha2^{M}$-$\alpha3^{M}$) and the two helices of the CHCH domain ($\alpha1^{CHCH}$-$\alpha2^{CHCH}$, Figure 34). Helices $\alpha1^{M}$-$\alpha2^{M}$-$\alpha3^{M}$-$\alpha1^{CHCH}$-$\alpha2^{CHCH}$ represent construct Mitofilin_C-CHCH before trypsin digestion, whereby $\alpha3^{M}$-$\alpha1^{CHCH}$-$\alpha2^{CHCH}$ were visible in the first structure (Figure 16).
142 of 149 residues could be modelled in at least one chain (Figure 34 C). The linker between mitofilin domain and CHCH domain could not be modelled, while the linker between LBS1 and mitofilin domain displayed different arrangements and poor electron density (Figure 34 B). The disulfide bond within CHCH domain is visible in all chains, similar to the previous structure of Mitofilin_C-CHCH. Overall, the four chains can be superimposed with RMSDs of 0.511-0.664 Å over 121-124 Cα atoms, pointing to a highly related structure. High flexibility is found in the non-natural linker regions and termini.

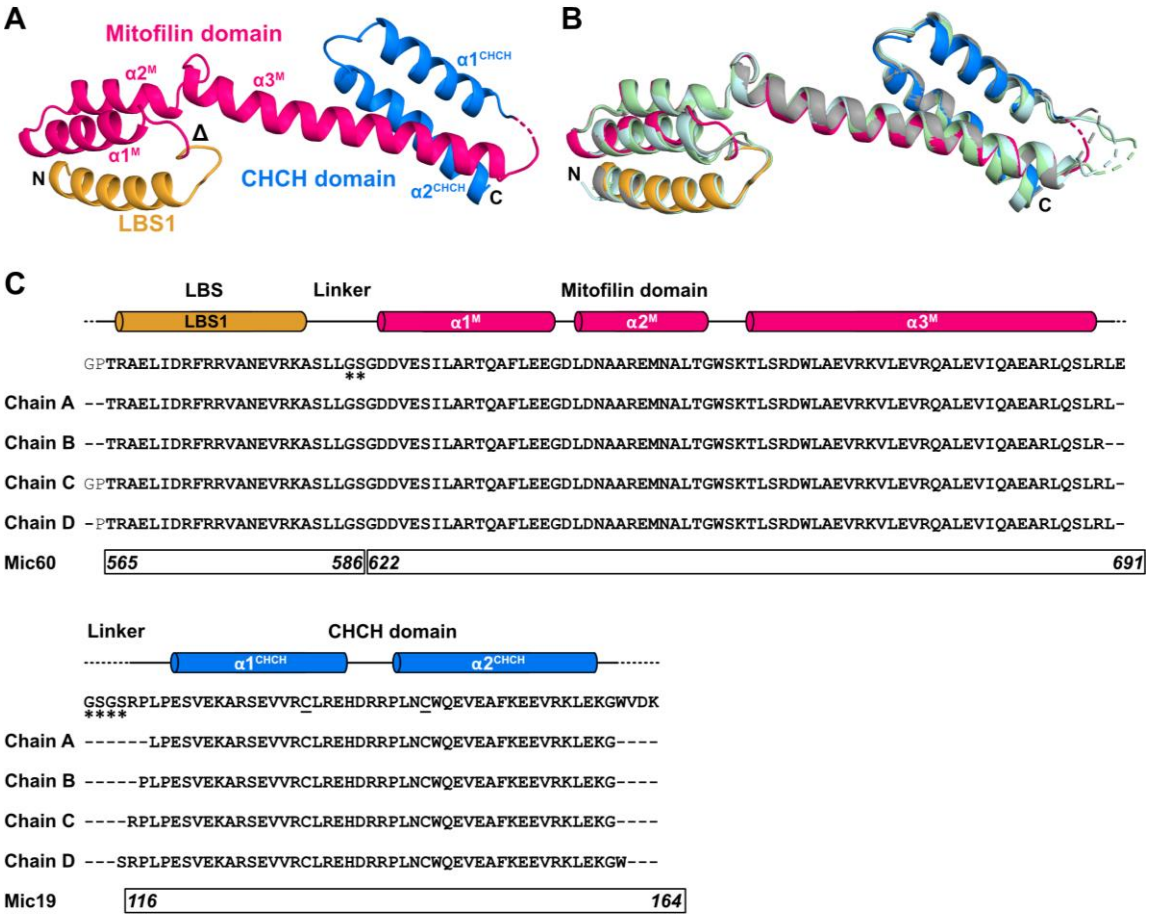

Figure 34: Monomer structure of Mitofilin-CHCH_2 and alignment. (A) Monomer (chain A) of Mitofilin-CHCH_2 in ribbon representation. Domains are colored individually and termini are labelled. The linker region between mitofilin (M) and CHCH domain (CHCH) is not resolved in the structure and indicated by a dashed line. The linker between LBS1 and mitofilin domain (removal of LBS2) is indicated by delta (Δ). **(B)** Monomer as in (A) aligned with the three additional chains of the asymmetric unit (see Figure 33); chain B: grey, chain C: cyan, chain D: green. **(C)** Sequence alignment and overview of all chains of the asymmetric unit. The first amino acid sequence represents Mitofilin-CHCH_2 after cleavage of the His_6-tag; GP (non-bold) vector derived. Non-natural linkers are marked with asterisks; cysteine residues forming a disulfide bond are underlined. Strokes within the sequence represent amino acids, which could not be modelled. Domains are labelled and colored as in (A). The cursive numbers at the bottom display the nomenclature according to Mic60 or Mic19. See also Appendix Figure C.3.

5.10. Structural comparisons

To compare the crystal structures of Mitofilin-CHCH_2 and Mitofilin_C-CHCH, the protein backbones (Cα) were superimposed. Superposition shows that the two structures share three helices ($\alpha3^{M}$-$\alpha1^{CHCH}$-$\alpha2^{CHCH}$) and the protein backbones superimpose well with an RMSD of 0.361 Å over 58 Cα atoms (Figure 35 A).

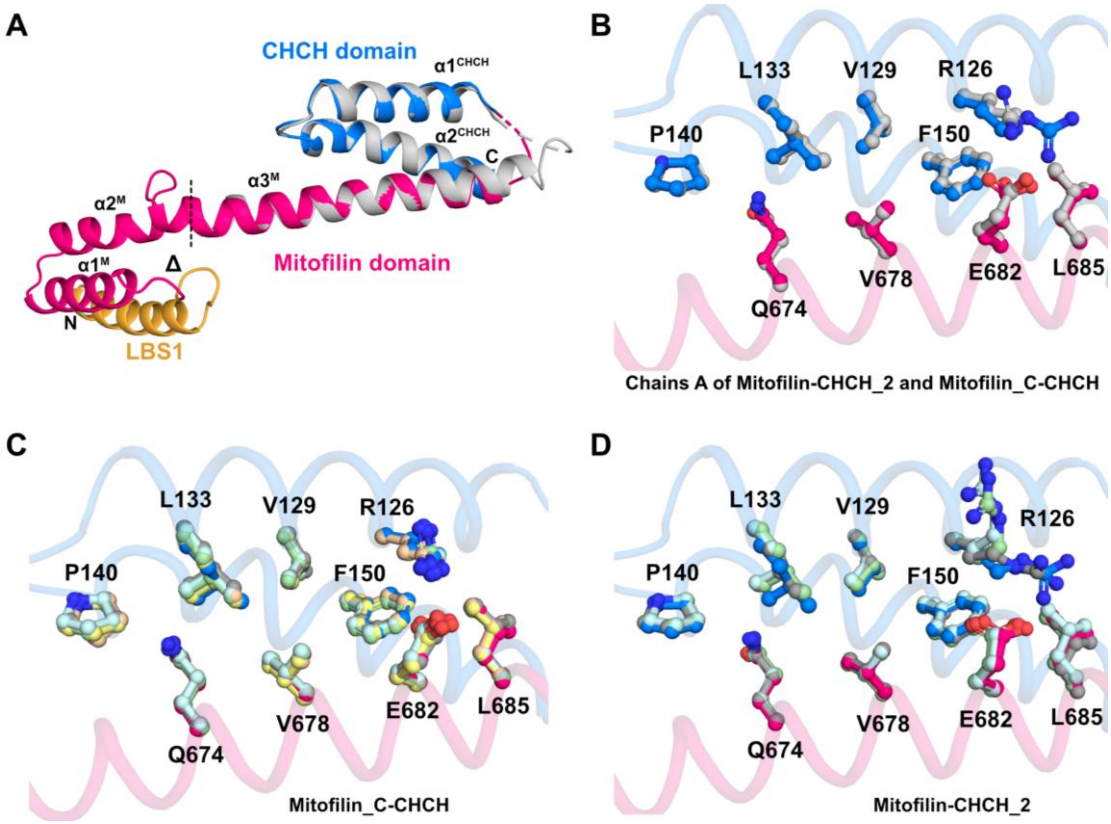

Figure 35: Alignment of Mitofilin-CHCH_2 and Mitofilin_C-CHCH. (A) Mitofilin-CHCH_2 (chain A) is aligned with the structure of Mitofilin_C-CHCH (light grey); both shown in ribbon representation. Domains of Mitofilin-CHCH_2 are colored individually and termini are labelled. The linker region between the mitofilin domain and the CHCH domain is not resolved in the structure and indicated by a dashed line (colored). The linker between LBS1 and the mitofilin domain (removal of LBS2) is indicated by delta (Δ). The black dashed line (vertical) marks the N-terminus of Mitofilin_C-CHCH after limited proteolysis. **(B)**, **(C)**, **(D)** Mic60-Mic19 interface shown in detail. Selected residues involved in the interaction are shown and labelled. (B) Alignment of chain A of Mitofilin-CHCH_2 (pink, blue) with residues of chain A of Mitofilin_C-CHCH (grey). (C) Alignment of residues of all chains of Mitofilin_C-CHCH. Chain A: pink and blue, chain B: green, chain C: beige, chain D: grey, chain E: cyan, chain F: yellow; backbone of chain A. (D) Alignment of residues of all chains of Mitofilin-CHCH_2. Chain A: pink and blue, chain B: grey, chain C: cyan, chain D: green; protein backbone of chain A.

As Mitofilin_C-CHCH, Mitofilin-CHCH_2 comprises the interaction interface of the mitofilin domain and the CHCH domain. Backbone superposition demonstrates that most of the analyzed residues involved in the Mic60-Mic19 interaction display the same conformation in Mitofilin-CHCH_2 and Mitofilin_C-CHCH (Figure 35 B). However, the salt bridge between Mic60_E682 and Mic19_R126 is only observed in chains A and B of Mitofilin-CHCH_2 (Figure 35 D). Instead, in chains C and D, crystal contacts with molecules in the adjacent asymmetric unit occurred.

In agreement with the structure prediction, LBS1 is positioned in close proximity to the mitofilin domain in Mitofilin-CHCH_2. Superposition of the prediction and the crystal structure reveals that LBS1 and the first two helices of the mitofilin domain ($\alpha1^{M}$, $\alpha2^{M}$) align well (Figure 36 A), indicating that the non-natural linker does not disturb the domain arrangement. However, the long mitofilin domain helix ($\alpha3^{M}$) is arranged in a different orientation. The flexible linker between $\alpha2^{M}$ and $\alpha3^{M}$ helix could enable a conformational change of the mitofilin domain (Figure 36 A, dashed arrow).
Interestingly, the mitofilin domain helix $\alpha3^{M}$ of one monomer completes the predicted four-helix bundle in the second monomer of the dimer (Figure 36 B).

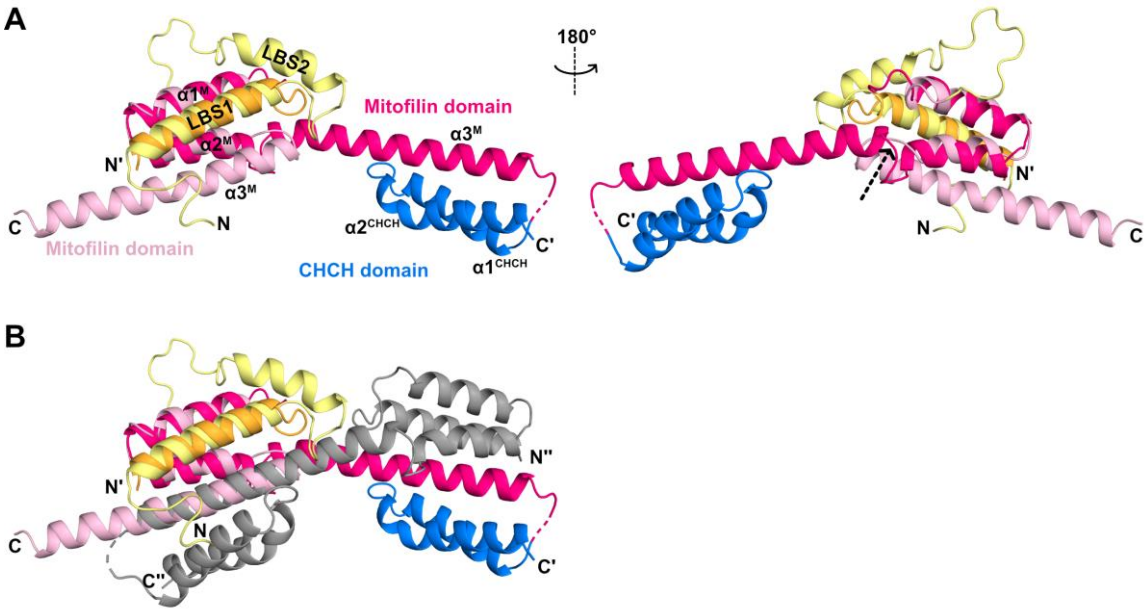

Figure 36: Alignment of Mitofilin-CHCH_2 and Mic60 prediction. (A) Superposition of structure prediction of *Chaetomium thermophilum* Mic60 (residues 557-685) and monomer (chain A) of Mitofilin-CHCH_2; both shown in ribbon representation. Domains are colored individually. Mic60 prediction comprises lipid binding site (LBS, yellow) and mitofilin domain (rose); N- and C-termini (N, C) are labelled. Mitofilin-CHCH_2 is colored in orange (LBS1), pink (mitofilin domain) and blue (CHCH domain) and termini are marked with N' or C'. The linker region between mitofilin domain and CHCH domain is not resolved in the crystal structure and indicated by a dashed line (colored). α-helices are labelled; M: mitofilin domain, CHCH: CHCH domain. The flexible linker between $\alpha2^{M}$ and $\alpha3^{M}$ is marked by a dashed arrow. Structure prediction derived from the *EVolutionary Couplings Server* (Hopf et al., 2019; see Figure 30). **(B)** Structure as in (A), but instead of Mitofilin-CHCH_2 monomer, the dimer is shown; the second monomer (chain B) is colored in grey and termini are labelled with N'' and C''.

5.11. Membrane binding of Mic60

It was shown that deletion of the LBS reduced liposome binding of $Mic60_{sol}$ (Hessenberger et al., 2017). However, the used $Mic60_{sol}$ constructs all contained the coiled-coil domain of Mic60. This raised the question whether the coiled-coil domain is necessary for liposome binding in addition to the LBS. Furthermore, I wanted to explore the effect of deleting LBS2 on liposome binding. To test this, liposomes co-sedimentation assays were performed as described previously (5.5.2., 4.3.13., see

construct overview in Figure 37 A-E). Interestingly, in contrast to $Mic60_{sol}$, Mitofilin_C-CHCH and Mitofilin-CHCH_2 did not bind to liposomes (Figure 37 F, G).

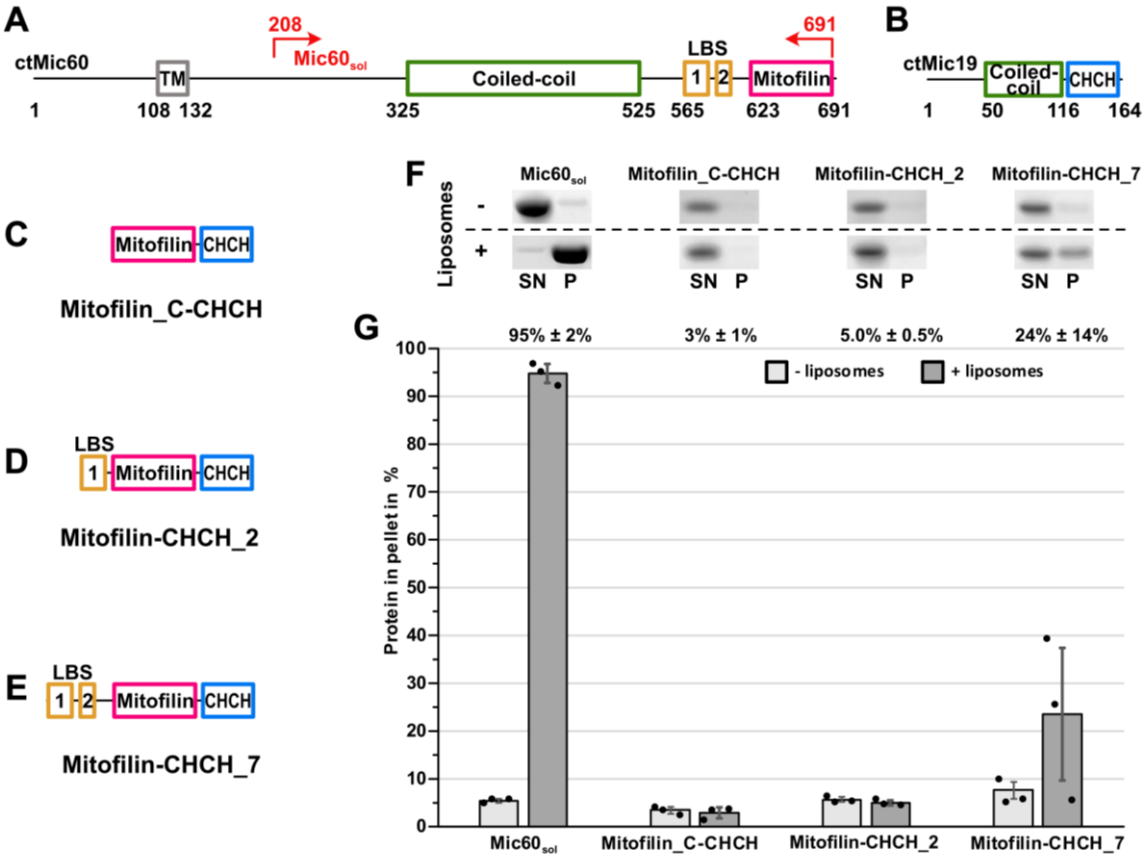

Figure 37: Liposome co-sedimentation assays using $Mic60_{sol}$ and different Mic60-Mic19 fusion constructs. (A), **(B)** Schematic representation of the domain structure of ctMic60 and ctMic19 as shown in Figure 10. TM: transmembrane helix, Coiled-coil: coiled-coil domain, LBS: lipid binding site, Mitofilin: mitofilin domain, CHCH: CHCH domain; numbers show the amino acid position; in this study a soluble Mic60 construct $Mic60_{sol}$ was used instead of full-length Mic60, the construct borders are labelled. **(C)**, **(D)**, **(E)** Schematic representation of the fusion constructs used in the liposome co-sedimentation assays. **(F)** 4-12% SDS-PAGE gel cuttings stained with Coomassie Brilliant Blue. The experiments were performed in the absence (-) or presence (+) of Folch liposomes. SN: supernatant after centrifugation; P: pellet. **(G)** Quantification of liposome co-sedimentation assays using *ImageJ* (Schneider et al., 2012). The bars indicate the average percentage of protein found in the pellet with respect of the total protein applied on the gel (protein in SN + protein in P = 100%). The calculated standard deviations are shown and the dots represent the results of three independent experiments. The numbers above the bars show the calculated values for the pellet fraction of the respective protein in presence of liposomes.

For Mitofilin-CHCH_7, experiments were difficult to reproduce, which may be caused by the tendency of the protein to precipitate. However, some liposome binding was consistently observed. These results suggest that LBS1 and LBS2, and likely their spatial arrangement, are important for liposome binding.

Furthermore, comparison with $Mic60_{sol}$ revealed reduced liposome binding of Mitofilin-CHCH_7 (Figure 37 G). This suggests that the presence of LBS is not sufficient for liposome binding, or the LBS is not correctly arranged in Mitofilin-CHCH_7. However, the most significant difference between both constructs is the coiled-coil domain of Mic60, which seems to contribute to liposome binding perhaps via a scaffolding function.
Taken together, these data indicate that the coiled-coil domain of Mic60 is needed for membrane binding, in addition to LBS1 and LBS2.

The mitofilin domain dimer forms a crescent-shaped membrane-binding site, which could interact within the highly curved crista junction membrane (Figure 38). To confirm the predicted membrane binding surface, a structure-based mutagenesis approach using $Mic60_{sol}$ was applied, with a focus on positively charged amino acids as possible binding partners for negatively charged phospholipid head groups. The first helix of the mitofilin domain ($\alpha1^{M}$) is in close proximity to LBS1 and might also be involved in membrane binding (Figure 38).
To probe this interface, surface-exposed positive charged residues in these regions were mutated to aspartate. Double mutants were designed if two positively charged amino acids were next to each other. These mutants were expressed and purified as $Mic60_{sol}$ (described in 5.5.1). The SEC profiles of the peak areas are shown in Figure 39 A.

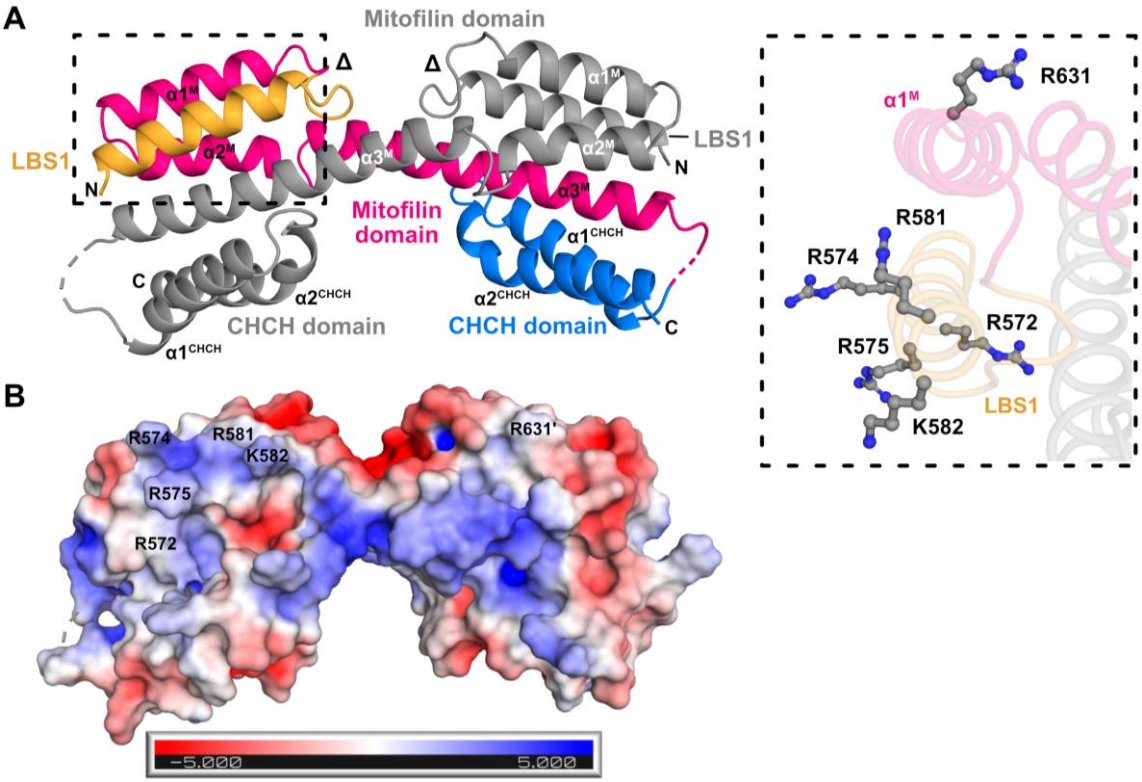

Figure 38: Surface analysis of Mitofilin-CHCH_2. (A) Mitofilin-CHCH_2 dimer composed of chains A and B shown in ribbon representation. Domains of chain A are colored individually and N- and C-termini are labelled. Chain B is colored in grey. The linker region between mitofilin domain (M) and CHCH domain (CHCH) is not resolved in the crystal structure and indicated by a dashed line. The GS linker between LBS1 and the mitofilin domain (removal of LBS2) is indicated by delta (Δ). The black dashed rectangle indicates LBS1 and the partial mitofilin domain shown in detail. Selected residues likely involved in membrane binding are shown and labelled (chain A). **(B)** Electrostatic surface potential projected on Mitofilin-CHCH_2 dimer shown in (A). Red color indicates negative charge, blue color positive charge at neutral pH. Selected residues likely involved in membrane binding (chain A) are labelled (see A); R631' of chain B is labelled.

In liposome co-sedimentation assays (see 4.3.13), $Mic60_{sol}$_R574D/R575D and $Mic60_{sol}$_R581D/K582D showed considerably reduced liposome binding of approx. 50% (Figure 39 B, C). In case of $Mic60_{sol}$_R631D, a reduction of approx. 20% was observed. Sequence conservation (analyzed in section 5.13) revealed that ctMic60_R574 and R575 vary among different species, whereas R581, K582 and R631 are highly conserved (Figure 42). For ctMic60_R631, the corresponding positive amino acid seems to be shifted one helix turn in higher eukaryotes (Figure 42, yellow star).

ctMic60_R572 is a highly conserved positive amino acid within LBS1, and its mutation reduced membrane binding (Hessenberger et al., 2017). This residue points toward the dimer interface in my structure, and does not have an obvious role in membrane binding (Figure 38).

In summary, these experiments indicate that the crescent-shaped surface in the mitofilin dimer comprises the membrane-binding site.

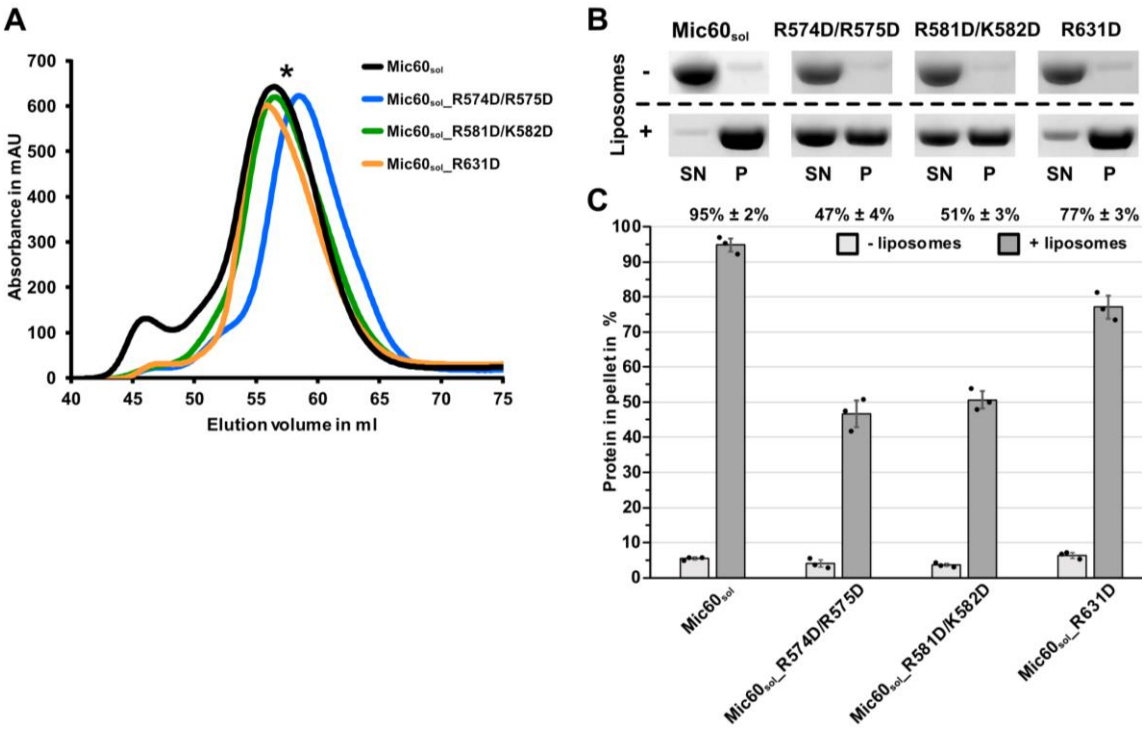

Figure 39: Liposome binding of Mic60$_{sol}$ constructs. (A) SEC purification chromatogram sections. An ÄKTApurifier chromatography system connected to a HiLoad 16/600 Superdex 200 pg column (GE Healthcare) was used. Absorption was measured at 280 nm. 1 ml fractions were collected. The asterisk shows the pooled peaks (complete SEC chromatogram of Mic60$_{sol}$ in Figure 18 A). **(B)** 4-12% SDS-PAGE gel cuttings stained with Coomassie Brilliant Blue. The experiments were performed in absence (-) or presence (+) of liposomes. SN: supernatant after centrifugation; P: pellet. **(C)** Quantification of liposome co-sedimentation assays using *ImageJ* (Schneider et al., 2012). The bars indicate the average percentage of protein found in the pellet with respect of total protein applied on the gel (SN + P = 100%). The calculated standard deviations are shown and the dots represent the results of three independent experiments. The numbers above the bars show the calculated values for the pellet of the respective protein in presence of liposomes.

5.12. Characterization of the dimer interfaces of the mitofilin domain

The crystal structure of Mitofilin-CHCH_2 not only revealed an inter-domain swapped dimer, but also raised the opportunity to study the dimer interfaces in more detail and get more information about the physiological relevance. Analysis of the structure revealed two evolutionary conserved dimer interfaces (Figure 40 A, Figure 42). In both cases, interactions were mediated via hydrophobic contacts. Interface 1 is located in the long mitofilin helix ($\alpha3^M$) and composed of the conserved residues W662, V666 and the non-conserved residue V669. In both monomers, the same residues are involved in the interaction in an antiparallel manner.
The second conserved interface consists of a hydrophobic pocket formed by F573, V576, V580, M648 and L651. L676 in $\alpha3^M$ of monomer 1 inserts into this hydrophobic pocket formed by LBS1 and the mitofilin domain (helix $\alpha2^M$) of the second monomer (Figure 40 A).

Single-point mutations were introduced into Mitofilin-CHCH_2 to analyze the dimer interfaces in more detail. Residues W662, V666 and L676 were mutated to aspartate, respectively, to tackle both interfaces. Proteins were expressed and purified as described in section 5.1. The SEC profiles of the main peak area (Figure 40 B) showed that only the main peaks of Mitofilin-CHCH_2 and mutant L676D are symmetric. Surprisingly, mutant L676D could be more highly concentrated compared to wild-type Mitofilin-CHCH_2.
In contrast, Mitofilin-CHCH_2_W662D and Mitofilin-CHCH_2_V666D started to precipitate during the purification process and were not stable. Therefore, only mutant Mitofilin-CHCH_2_L676D was further analyzed.

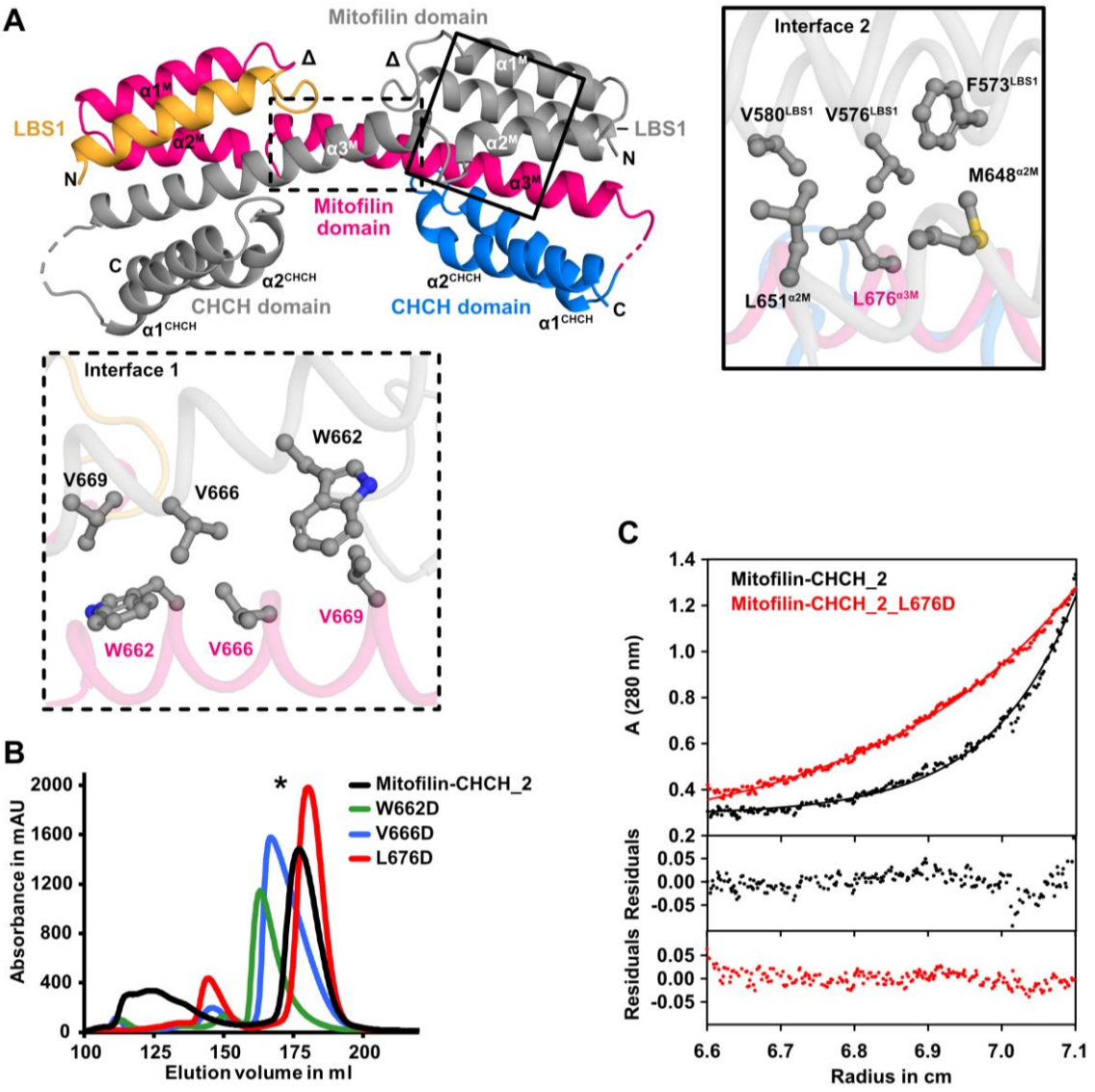

Figure 40: Dimer interfaces of Mitofilin-CHCH_2. (A) Dimer composed of chains A and B shown in ribbon representation. Domains of chain A are colored individually. Chain B is colored in grey. Termini and helices are labelled. The linker region between mitofilin domain and CHCH domain is not resolved in the structure and indicated by a dashed line. The GS linker between LBS1 and mitofilin domain (removal of LBS2) is indicated by delta (Δ). Black rectangles show the dimer interfaces in detail. Selected residues are shown and labelled (chain A in color, chain B in grey). All shown residues in the black dashed rectangle belong to helix $\alpha3^{M}$. **(B)** SEC purification chromatogram sections of Mitofilin-CHCH_2 and dimer interface mutants. An ÄKTApurifier chromatography system connected to a HiLoad 16/600 Superdex 75 pg column (GE Healthcare) was used. Absorption was measured at 280 nm and 1 ml fractions were collected. The asterisk points to pooled peaks. **(C)** Sedimentation equilibrium AUC runs using 1 mg/ml protein concentration. The upper panel shows the experimental data (dots) and the fit of the data (solid line), the lower two panels show the deviation of the fit to the data. The fit yielded a molecular mass of Mr = 34 ± 4 kDa for Mitofilin-CHCH_2 (black), which corresponds to a dimer and Mr = 16 ± 2 kDa for Mitofilin-CHCH_2_L676D (red), which corresponds to a monomer. A: absorbance. AUC experiments were performed by Dr. Hauke Lilie at the Martin-Luther-Universität Halle-Wittenberg.

Sedimentation equilibrium analytical ultracentrifugation (AUC) experiments were performed by Dr. Hauke Lilie at the Martin-Luther-Universität Halle-Wittenberg (see section 4.3.16.). The determined relative molecular mass (Mr) of Mitofilin-CHCH_2 (Figure 40 C) shows the presence of a predominant dimeric species in solution (Mr = 34 ± 4 kDa), as expected from the crystal structure. In contrast, Mitofilin-CHCH_2_L676D is present as a monomer in solution (Mr = 16 ± 2 kDa). These results confirm that Mitofilin-CHCH_2 is present as a dimer in solution and that mutation L676D disrupts the dimeric state of Mitofilin-CHCH_2.

The role of the mitofilin domain dimer in $Mic60_{sol}$ was further analyzed by Tobias Bock-Bierbaum (MDC). He introduced L676D into $Mic60_{sol}$ and performed blue native PAGE analysis. $Mic60_{sol}$_L676D showed similar oligomerization as $Mic60_{sol}$ (Figure 41). A complex consisting of $Mic60_{sol}$_L676D and Mic19 showed slightly reduced oligomerization in comparison to $Mic60_{sol}$-Mic19. Furthermore, it seems that a fraction of $Mic60_{sol}$_L676D does not interact with Mic19.

Previously, Tobias Bock-Bierbaum could crystallize the coiled-coil domain of *Lachancea thermotolerans* Mic60 (yeast), which displays a tetramer consisting of two antiparallel dimers (unpublished data). Using structure based-mutagenesis he identified the residues V455 and F461 to be crucial for $Mic60_{sol}$ tetramerization. Introduction of V455D/F461D into $Mic60_{sol}$ rendered the protein almost exclusively dimeric (Figure 41). A similar result was obtained for the triple mutant $Mic60_{sol}$V455D/F461D/L676D. However, while a complex of $Mic60_{sol}$V455D/F461D and Mic19 is still able to partially oligomerize to higher-order oligomers, incubation of $Mic60_{sol}$V455D/F461D/L676D with Mic19 resulted in only one predominant band, which should represent a dimeric Mic60-Mic19 complex or the $Mic60_{sol}$V455D/F461D/L676D dimer.
In conclusion, the Mic60 tetramer interface in the coiled-coil domain and the mitofilin domain dimer seem to be important and to cooperate during oligomerization of the Mic60-Mic19 complex.

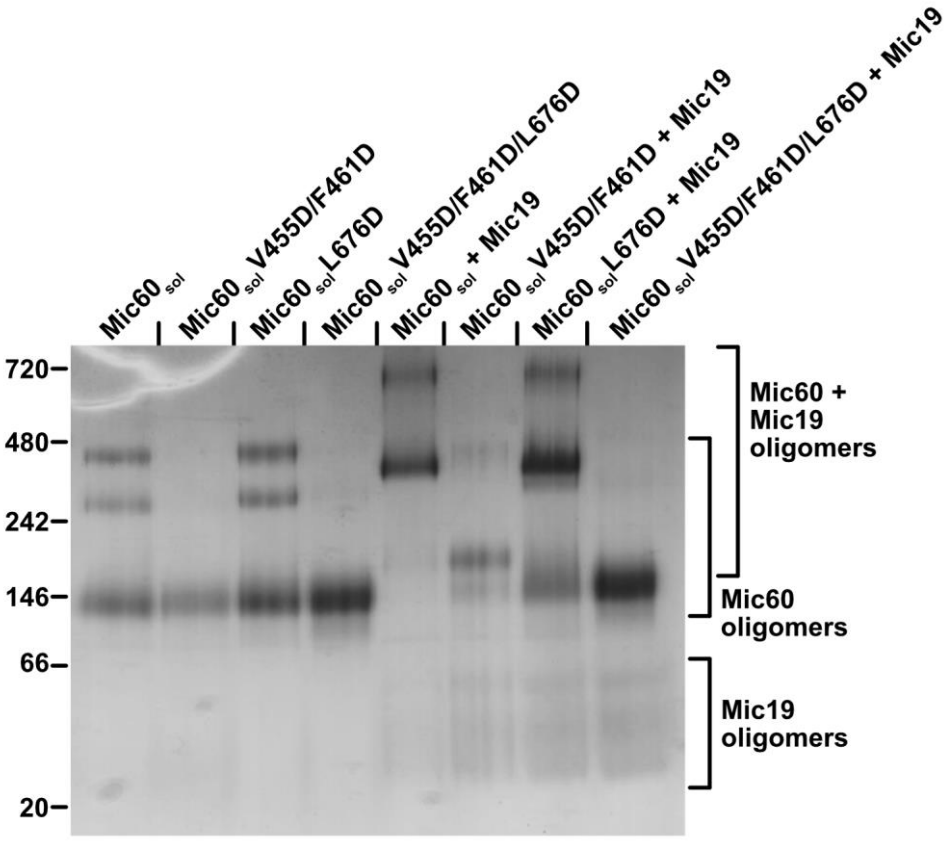

Figure 41: Blue native PAGE analysis of Mic60$_{sol}$ tetramer and dimer interfaces. 4-16% Bis-Tris gel stained with Coomassie Brilliant Blue; Marker: NativeMark™ Unstained Protein Standard. The numbers indicate the MW in kDa. The experiment was performed by Tobias Bock-Bierbaum (MDC).

5.13. Evolutionary conservation analysis

The crystal structure of Mitofilin-CHCH_2 revealed the structural arrangement of LBS1 and the complete mitofilin domain, which is in general in accordance with secondary structure prediction (Figure 42, see also Figure 25). The conservation of the mitofilin domain was already described previously (Rabl et al., 2009; von der Malsburg et al., 2011; Körner et al., 2012; Zerbes et al., 2012). In addition, sequence alignment revealed that several amino acids of LBS1 are also conserved within different species (Figure 42, Hessenberger et al., 2017). Distinct aspects of the mitofilin domain were analysed in the preceding sections including dimerization, membrane binding and

interaction with the CHCH domain of Mic19. The analysed residues are labelled in Figure 42 revealing that most of them are conserved.

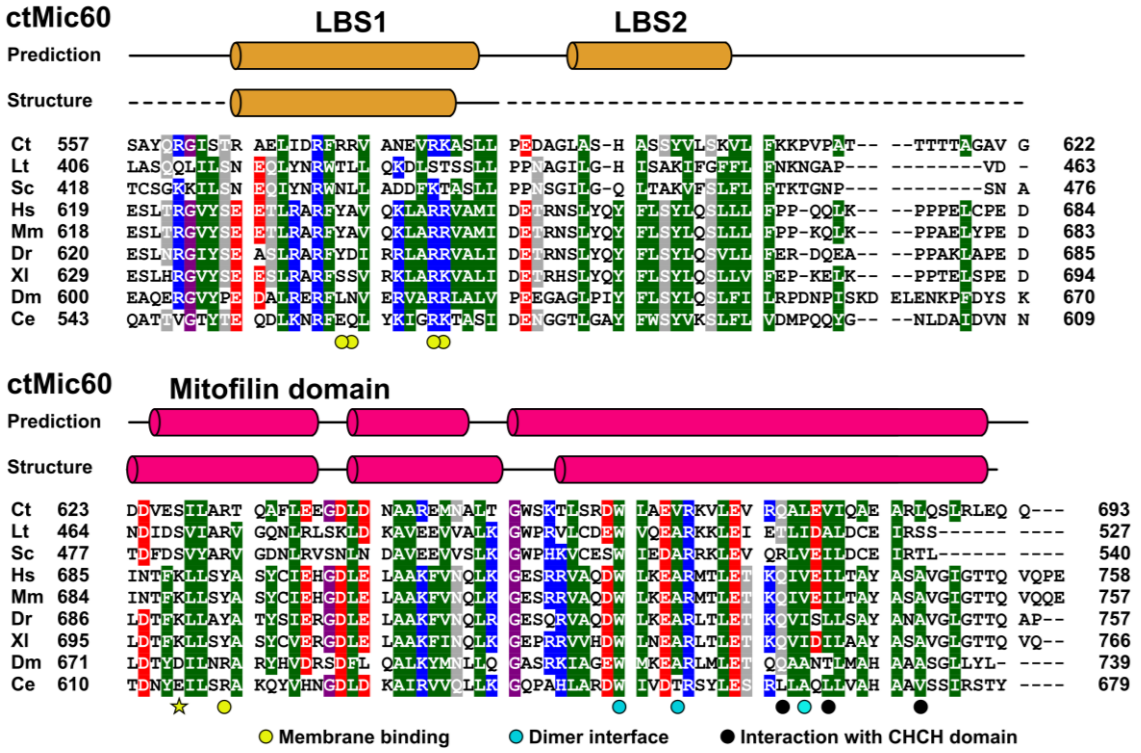

Figure 42: Secondary structure of LBS and mitofilin domain of Mic60 and sequence alignment. Secondary structure of LBS and mitofilin domain according to the structures of Mitofilin-CHCH_2 and Mitofilin_C-CHCH, and *PSIPRED* prediction (Buchan and Jones, 2019; Jones, 1999; see Appendix C). Cylinders represent α-helices. The dashed line indicates residues, which could not be modeled in the crystal structure. Mic60 from different species were aligned using *Clustal Omega* (Sievers et al., 2011) and manually refined (UniProtID in parentheses); Ct: *Chaetomium thermophilum*, Mic60 (G0SHY5); Lt: *Lacchancea thermotolerans*, Mic60 (C5E325); Sc: *Saccharomyces cerevisiae*, Mic60 (P36112); Hs: *Homo sapiens*, Mic60 (Q16891); Mm: *Mus musculus*, Mic60 (Q8CAQ8); Dr: *Danio rerio*, Mic60 (Q6PFS4); Xl: *Xenopus laevis*, Mic60 (A0A1L8HT59); Dm: *Drosophila melanogaster*, Mic60 (P91928); Ce: *Caenorhabditis elegans*, Mic60 (Q22505). Numbers represent the amino acid position (within full-length protein). A lack of the corresponding residue is indicated by a stroke. Residues with a conservation greater than 66% (6/9) are colored in red (D, E), blue (H, K, R), green (A, F, I, L, M, V, W, Y), purple (G, P), black (C) or grey (N, Q, S, T). The dots below the sequences indicate residues analyzed in this study; overlaying dots: double mutant. The star points to a lysine residue (K) in Hs, Mm, Dr and Xl, which might correspond to ctMic60_R631.

To gain insights into the position of conserved surface patches of Mic60 or Mic19, a surface representation of Mitofilin-CHCH_2 monomer is shown, where amino acids are colored according to their conservation (Figure 43, details in 4.4.5). A second monomer is presented in ribbon representation to indicate the conservation of the dimer interface. Furthermore, the dimer interface comprising L676 is shown in detail at two positions of the dimer (Figure 43 B, top). The dimerization interface shows a high conservation level.

To illustrate the interaction between Mic60 and Mic19, either the mitofilin domain or the CHCH domain is presented in ribbon representation or with surface conservation, respectively (Figure 43 B, dashed rectangles). Residues involved in the interaction display different levels of conservation, ranging from average to complete conservation. Interestingly, most of the residues of the CHCH domain, which are not involved in interaction with the mitofilin domain, are variable (colored in cyan).
In conclusion, the dimerization in the mitofilin domain and the mitofilin-CHCH-domain interface of Mic60 and Mic19 are evolutionary conserved, pointing a conserved function in evolution.

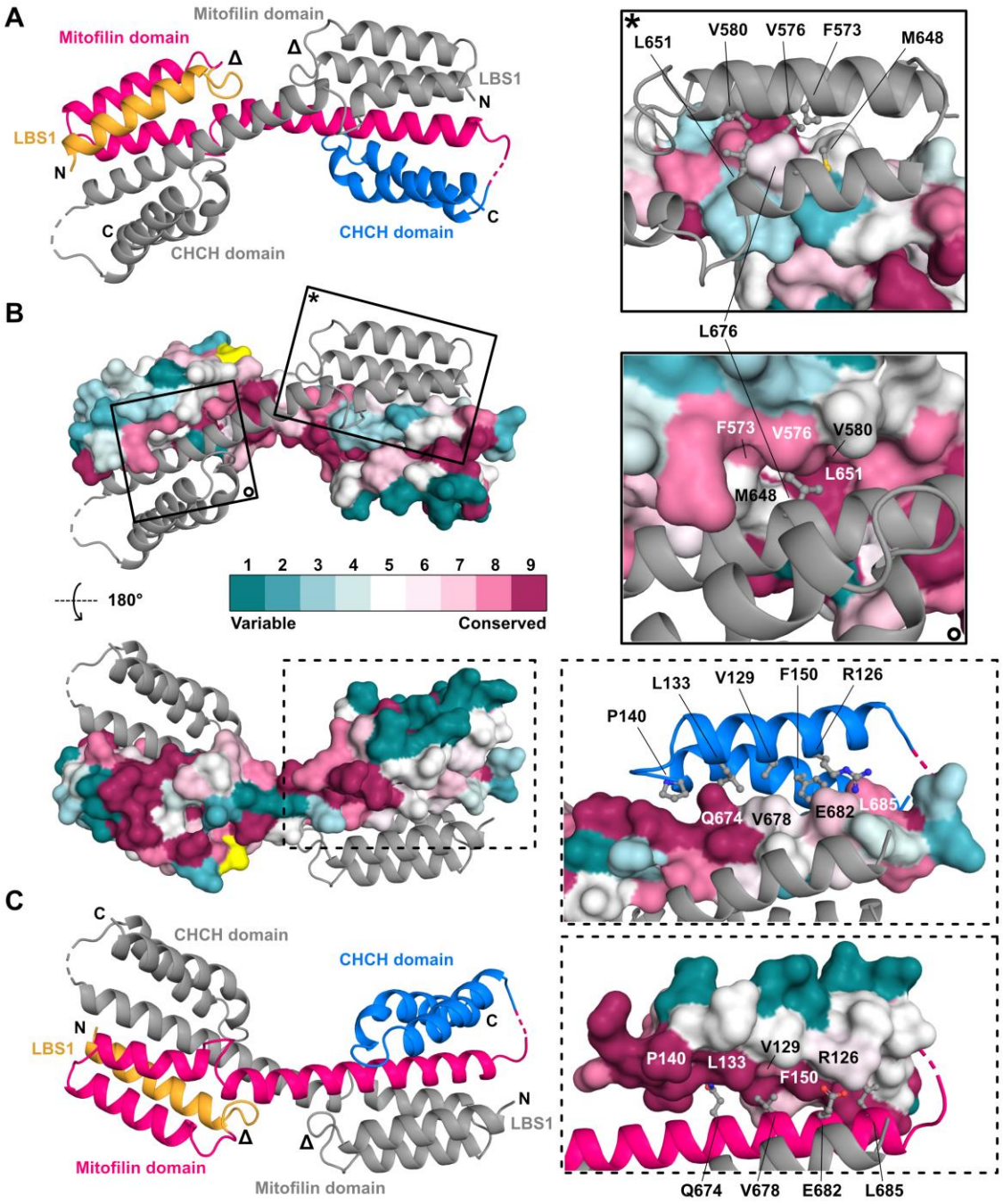

Figure 43: Conservation of the dimer interface and the Mic60-Mic19 interaction interface. (A) Mitofilin-CHCH_2 (chains A and B) in ribbon representation; termini labelled. Domains of chain A are colored individually, chain B: grey. The linker region between mitofilin and CHCH domain is indicated by a dashed line (not resolved). Linker between LBS1 and mitofilin domain (LBS2 removal) is indicated by delta (Δ). **(B)** Structure as in (A) with surface conservation plot of chain A using *ConSurf* (Ashkenazy et al., 2016; details in 4.4.5). GS linker is colored in yellow. Rectangles (black line) indicate the dimer interface shown in detail (interface 2, Figure 40). Selected residues involved in the interaction are shown and labelled. Black dashed rectangle indicates Mic60-Mic19 interaction shown in detail. Either the mitofilin or the CHCH domain is shown in ribbon representation or with surface conservation, respectively. Selected residues are shown and labelled (chain A). **(C)** Structure as in (A) 180° turned counter-clockwise (x-axis).

6. Discussion

In this study, the structure of the mitofilin domain of Mic60 and the CHCH domain of Mic19 was determined. The interaction between the mitofilin domain and the CHCH domain was analyzed in detail, demonstrating that mutation of hydrophobic residues in the interface disturbs the interaction *in vitro* and *in vivo*. Moreover, liposome binding of several Mic60 constructs and mutants was analyzed, leading to the suggestion that the coiled-coil domain and the LBS cooperate in lipid binding. The mitofilin domain formed a dimer in the crystal structure, revealing a crescent-shaped surface for membrane binding and remodeling. Several aspects of these results will be discussed in the following sections and a model for Mic60-Mic19 function in cristae morphology is presented.

6.1. LBS1 and mitofilin domain form a functional element

Most of the MICOS components are conserved in eukaryotes. Mic60 seems to be the oldest of these proteins, as even α-proteobacteria contain a Mic60 homolog (Munoz-Gomez et al., 2015; Huynen et al., 2016). Within Mic60, the mitofilin domain shows the highest sequence conservation pointing to an important physiological function (Figure 25, Figure 42; Munoz-Gomez et al., 2015). Mic60 was shown to bind to liposomes and induce membrane curvature, independently of the transmembrane region (Hessenberger et al., 2017; Tarasenko et al., 2017). Membrane bending activity of Mic60 is an ancient mechanism, as Mic60 from α-proteobacteria are also able to deform membranes (Tarasenko et al., 2017; Munoz-Gomez et al., 2015). Two predicted helices, located between the coiled-coil and the mitofilin domain, are involved in Mic60 mediated membrane remodeling (Hessenberger et al., 2017). Due to this observation, this region was termed lipid binding site (LBS) and the two helices LBS1 and LBS2. Membrane remodeling is a very important process in mitochondria, thus it is not surprising that this membrane binding site is crucial for mitochondrial ultrastructure (Hessenberger et al., 2017). However, the exact mechanism of Mic60 membrane binding and remodeling remained unclear.

In this work, co-evolutionary sequence analysis (Hopf et al., 2019) was initially used to obtain more insights. In this pipeline, multiple sequences were aligned to identify evolutionary couplings and predict protein structures *de novo*. The mitofilin domain and the LBS seem to be suitable for this analysis due to the high sequence conservation facilitating sequence alignment (Figure 42). The obtained model (Figure 30) seemed to be reasonable at first sight as the helices corresponded well with secondary structure prediction (Appendix C). Interestingly, LBS1 was predicted to be in close proximity to the mitofilin domain due to evolutionary couplings resulting in the formation of a four-helix bundle consisting of one helix LBS1 and three helices of the mitofilin domain (Figure 30). This model could explain why structure determination of the construct Mitofilin_C-CHCH lacking the LBS failed (Figure 13 A, B): LBS1 seems to be important for stabilization of the four-helix bundle, as well as structural arrangement and orientation of the mitofilin domain. The lack of LBS1 could lead to excessive flexibility, hindering proper crystal formation.

In the obtained structure of the construct Mitofilin-CHCH_2, LBS1 and the mitofilin domain are in close proximity, as predicted. Furthermore, LBS1 and the two smaller helices in the mitofilin also align well (Figure 36), which increases the credibility of the prediction. Since the domain arrangement is not disturbed, this indicates that the non-natural linker between LBS1 and $\alpha1^{M}$ does not interfere with proper folding. However, the predicted four-helix bundle does not form within a monomer, but within the dimer, e.g. the mitofilin domain helix $\alpha3^{M}$ of the second monomer completes the predicted four-helix bundle (Figure 36 B).

LBS and mitofilin domain are both evolutionary conserved and only separated via 19 residues in *Chaetomium thermophilum* (Figure 42). Hence, it is not aberrant to assume a structural connection between both domains. Furthermore, it is a common feature that domains or helices are structurally in close proximity, but distant in sequence, like the helical bundle signaling element of the dynamin family (Faelber et al., 2011).

The observation that Mitofilin-CHCH_2 exists as a dimer in the crystal raised the question if the dimer is a crystallographic artefact or if the mitofilin domain is also able to dimerize in solution, since high protein concentrations in the crystallization drop might favor dimer formation. AUC analysis clearly demonstrated that Mitofilin-CHCH_2

is present as a dimer in solution (Figure 40 C), consistent with the observed dimer in the crystal structure. Hence, the mitofilin dimer is not a crystal artefact. Moreover, the mitofilin domain was previously reported to be involved in homo-oligomer formation, as purified mitofilin domain (yeast) bound to full-length Mic60 in pull-down experiments (Körner et al., 2012).

The dimer interface mutants Mitofilin-CHCH_2_W662D and V666D were not stable and started to precipitate during concentrations, while Mitofilin-CHCH_2_L676D could be concentrated to similar or higher concentrations than the wild-type. Interestingly, in contrast to L676D, W662 and V666 are also involved in interactions within the predicted monomer (Figure 44). Furthermore, AUC experiments show that Mitofilin-CHCH_2_L676D exists as a monomer in solution (Figure 40 C). These observations demonstrate that the observed dimerization interface involving a domain-swapped dimer is indeed mediating assembly.

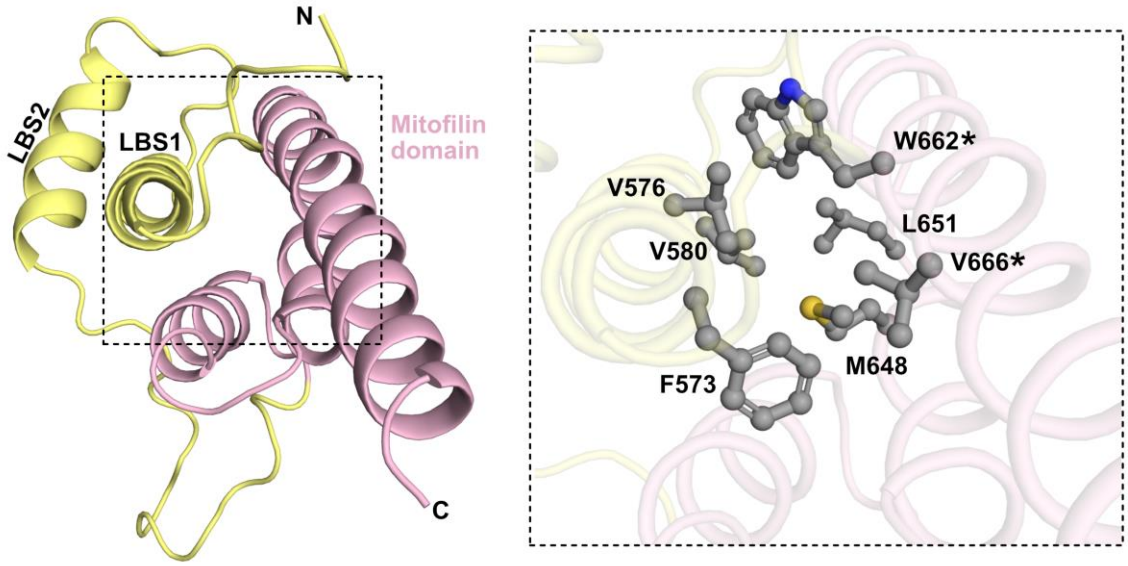

Figure 44: Monomer contacts of Mic60 prediction. (A) Structure prediction of *Chaetomium thermophilum* Mic60 (residues 557-685) comprising lipid binding site (LBS, yellow) and mitofilin domain (rose). N- and C-terminus and the two α-helices of LBS (LBS1, LBS2) are labelled. Black dashed rectangle shows monomer contacts in detail. Selected residues, also involved in dimer formation, are shown and labelled. W662 and V666 (Interface 1, Figure 40 A) are marked with asterisks. The structure prediction derived from the *EVolutionary Couplings Server* (Hopf et al., 2019).

The conformational change from a monomer to a dimer should be theoretically possible due to the flexible region between helices $\alpha2^M$ and $\alpha3^M$ of the mitofilin domain (Figure 36). Furthermore, interactions within the monomer, as well as dimer interactions are mediated via hydrophobic contacts. More precisely, the same conserved hydrophobic residues W662 and V666 in dimer interface 1, and F573, V576, V580, M648 and L651 in dimer interface 2 are involved in the predicted monomer and the experimentally determined dimer (Figure 44, Figure 40). These observations are in agreement with the idea that prior to dimerization, the mitofilin domain can also exist as a monomer. It also explains the high level of sequence conservation in these residues (Figure 42, Figure 43).

In a previous study, the conserved LBS1 residues R572 and F573 were analyzed in more detail. Mutation of these residues to aspartate had a dramatic effect on Mic60 membrane activity *in vitro* and *in vivo* and caused less membrane binding and remodeling, as well as disturbed mitochondrial ultrastructure (Hessenberger et al., 2017). Due to the predicted amphipathic character of LBS1, it was hypothesized that F573 inserts into the lipid bilayer and R572 interacts with negatively charged head groups (Hessenberger et al., 2017).
The structure of Mitofilin-CHCH_2 confirms the predicted amphipathic character of helix LBS1 (Hessenberger et al., 2017; Figure 38). However, as the hydrophobic part faces towards the four-helix bundle, a membrane insertion seems to be unlikely. Several conserved hydrophobic residues, including F573, are involved in the interaction with the mitofilin domain (Figure 40, Figure 44). Here, F573 is not on the protein surface, but located at a central position in the hydrophobic core, and seems to be crucial for the formation of the helix bundle. Mutation to aspartate should disturb the formation and proper arrangement of the mitofilin domain, which might explain the dramatic effects described in Hessenberger et al. (2017). Nevertheless, it cannot be excluded that a certain trigger leads to rearrangement of the helices, resulting in an opening of the helix bundle allowing LBS1 to insert into membranes. A similar scenario may account for the observed effects of R572. Although R572 points to the dimer interface in the structure of Mitofilin-CHCH_2, a potential function in membrane interaction cannot be excluded (Figure 38).

Structural information about LBS2 and the linker between LBS2 and the mitofilin domain are still missing, as constructs comprising LBS2 started to precipitate during

the purification processes. The region between LBS2 and the mitofilin domain is predicted to be unstructured and varies in length between different species. Interestingly, certain hydrophobic residues within this linker region are conserved (Figure 42). Assuming a correct secondary structure prediction, three conserved hydrophobic residues directly following LBS2 are of particular interest. In general, an unstructured linker region generates flexibility and the occurrence of conserved residues within this region points to a certain function. It is conceivable that these residues mediate interaction with interactions partners of Mic60 or mediate membrane contacts via insertion into the hydrophobic core of the lipid bilayer.
LBS2 forms a predicted α-helix and contains a high portion of conserved hydrophobic residues, especially in higher eukaryotes (Figure 42). It may also insert into the lipid bilayer and mediate membrane interaction. The presence of linkers preceding and following LBS2 should create flexibility and adaptability in positioning of LBS2.

Taking together, the structural results support the model, in which LBS1 and mitofilin domain form one functional element. In fact, it seems that LBS1 and LBS2 are integral part of the mitofilin domain.

6.2. Membrane shaping activity of MICOS

Mitochondria are highly dynamic organelles as they continuously divide and fuse (Westermann, 2010). These processes are accompanied by constant membrane remodeling events. At the same time, generation and stabilization of membrane curvature plays a crucial role (McMahon and Gallop, 2005). In general, the characteristic morphology of cells and organelles is defined by different membrane curvature events, for example generation of curvature during vesicle budding or generation of membrane sheets in the ER (Shibata et al., 2009). Membrane deformation can be introduced by lipids and/or proteins, and several mechanisms have been suggested (McMahon and Gallop, 2005).

Deletion of MICOS complex or single components dramatically alters cristae morphology, pointing to its crucial role in mitochondrial ultrastructure (von der Malsburg

et al., 2011). This raised the question of how MICOS contributes to membrane curvature. Most MICOS components except Mic19 (and Mic25 in mammals) are anchored in the IMM with at least one transmembrane helix (Figure 6, Figure 7). The soluble portions of these proteins are mostly exposed to the intermembrane space and may form a spacious scaffold. It has been discussed that such an asymmetric distribution of the extra-membrane domains in TM proteins can result in bending (McMahon and Boucrot, 2015). Mic10 has been suggested to employ a variation of this mechanism for membrane remodeling: The two transmembrane helices of Mic10 are proposed to adopt a hairpin topology with an asymmetric wedge shape (Barbot et al., 2015). Oligomerization of this wedge in the crista junction was proposed to create and maintain membrane curvature (Bohnert et al., 2015; Barbot et al., 2015).
Moreover, Mic12 is suggested to possess an amphipathic helix in the IMS-exposed domain containing one polar and one hydrophobic side (Huynen et al., 2016). Amphipathic helices can insert into one leaflet of the lipid bilayer and induce positive membrane curvature by asymmetric surface extension (McMahon and Gallop, 2005).

Mic60 is the largest MICOS component and possesses a single transmembrane helix. Apart from the anchoring function, the transmembrane helix of Mic60 seems not to be important for MICOS function (Körner et al., 2012), while the LBS plays a crucial role in membrane remodeling (Hessenberger et al., 2017). Despite the amphipathic character of LBS1, insertion of LBS1 into the membrane seems to be unlikely according to my obtained structure, as the helix is part of a stable four-helix bundle. However, conserved positive residues on the surface of LBS1 and the mitofilin domain seem to be involved in membrane interaction and might interact with negatively charged phospholipids (Figure 38, Figure 39). Furthermore, my structural analysis shows that the mitofilin domain dimer forms a crescent-shaped membrane-binding site (Figure 38). This intrinsic curvature is suitable for interaction with the crista junction membrane, which has a complementary negative membrane curvature. LBS2 could assist in introducing membrane curvature via insertion of its hydrophobic motif between lipid head-groups acting as a wedge (McMahon and Boucrot, 2015; section 6.1.). Thus, the mitofilin domain may deform the cristae membrane as an oligomerizing scaffold superimposing its shape onto the underlying membrane.

Mic60 contains a predicted coiled-coil domain, which length varies between different species. The coiled-coil domain of Mic60 alone was not able to bind to liposomes in

liposome co-sedimentation assays (Hessenberger et al., 2017) arguing against a membrane shaping activity like in BAR domain proteins (Peter et al., 2004; Shimada et al., 2007). The results of my studies rather indicate that the coiled-coil domain of Mic60 is needed to allow the LBS to efficiently bind to liposomes (Figure 37). The exact boundaries of the coiled-coil domain of ctMic60 are not clear. It is therefore also possible that the approx. 100 amino acids upstream of the predicted coiled-coil domain, which are included in $Mic60_{sol}$, contribute to liposome binding or protein folding. This could be tested by another construct excluding this portion of the protein.

Another feature of the employed mitofilin fusion constructs is the presence of the CHCH domain, which could disturb liposome binding. However, after co-incubation with Mic19, still approx. 95% $Mic60_{sol}$ co-sedimented with liposomes (Figure 24,), arguing against a negative impact of the CHCH domain.

Mic19 does not contain a transmembrane anchor, but seems to have a regulating function on Mic60 and other MICOS components (Friedman et al., 2015). Data from Hessenberger et al. (2017) indicate that Mic19 increases the membrane remodeling activity by Mic60. As Mic19 binding induces tetramerization, it can be envisioned that it may also promote the formation of the crescent-shaped dimeric membrane binding site in Mic60.

OPA1 has also been reported to interact with human Mic60, Mic19 and Mic25 (Darshi et al., 2011; Ding et al., 2015). Additionally to its function in mitochondrial fusion (Olichon et al., 2002; Cipolat et al., 2004), human OPA1 plays a critical role in maintenance of cristae and remodeling during apoptosis (Olichon et al., 2003; Frezza et al., 2006; Yamaguchi et al., 2008). OPA1 may form helical filaments at crista junctions, as postulated for the yeast homologue Mgm1 (Faelber et al., 2019). Via interaction with OPA1, MICOS could further influence membrane remodeling in mitochondria. However, there are no interactions with MICOS and Mgm1 described so far, pointing to a different mechanism in yeast.
Taken together, MICOS seems to combine different mechanisms of membrane deformation to ensure the formation of crista junctions. My results point to a crucial role of the dimeric mitofilin domain in creating mitochondrial membrane curvature via a scaffolding function.

6.3. Mic60-Mic19 interaction and regulation

Mic60 and Mic19 form one of the two MICOS subcomplexes (Bohnert et al., 2015; Guarani et al., 2015; Friedman et al., 2015; Anand et al., 2016). Both proteins interact predominantly via the mitofilin domain of Mic60 and the CHCH domain of Mic19, since deletion of either of these domains abolished the interaction (Hessenberger et al., 2017).

In my work, I used fusion constructs of the mitofilin domain and the CHCH domain to structurally unravel their interaction interface (Figure 17, Figure 29). In order to validate the significance of the observed interaction, interface mutations were introduced into almost full-length $Mic60_{sol}$ or full-length Mic19 (both from *Chaetomium thermophilum*) and the interaction was analyzed via blue native PAGE, ITC and liposome co-sedimentation assays. While these results confirmed the importance of the crystallographic interface also in a full length context, none of the introduced mutations resulted in a completely abolished Mic60-Mic19 interaction, since Mic19 still co-sedimented with Mic60 in the presence of liposomes and induced higher-order oligomers (Figure 24, Figure 19). One explanation for this observation could be that I analyzed single-point mutations, although several residues are involved in the interaction. However, these experiments could also point to a second binding site.

It has been shown in ITC experiments that an isolated CHCH domain construct of Mic19 binds with a twofold reduced affinity to Mic60 compared to full-length Mic19 (Hessenberger et al., 2017). This indicates that the N-terminal coiled-coil domain of Mic19 is also involved in the interaction, in agreement with data from Li et al. (2016). In addition, the isolated CHCH domain is not able to induce oligomerization of $Mic60_{sol}$ and is not sufficient to enhance membrane remodeling activity of $Mic60_{sol}$ in a membrane leakage assay (Hessenberger et al., 2017). This may suggest a sequential activation mechanism for Mic60: First, the mitofilin domain of Mic60 binds the CHCH domain of Mic19 with high affinity; subsequently, a second binding site is formed, which activates Mic60. In this way, Mic19 might regulate Mic60 activity in membrane remodeling.

CHCH domain-containing proteins are involved in several mitochondrial processes like biogenesis, quality control and dynamics (Modjtahedi et al., 2016). The characteristic feature of the CHCH domain of higher eukaryotes is the Cys-X_9-Cys motif within each of the two helices resulting in the formation of two disulfide bonds (Modjtahedi et al.,

2016; Darshi et al., 2011; Sakowska et al., 2015). The CHCH domain of yeast or *Chaetomium thermophilum* Mic19 only consists of one disulfide bond (Sakowska et al., 2015).
In this work, the formation of the disulfide bond was confirmed by mass spectrometry for all Mic19 constructs, as well as for Mic60-Mic19 fusion constructs and Mitofilin_C-CHCH after limited proteolysis (Figure 14, Appendix E). Furthermore, the disulfide bond was visible in both crystal structures. The CHCH domain has been shown to be important for import of Mic19 into the intermembrane space of mitochondria via the MIA pathway, whereas intermolecular disulfide bonds are described (Darshi et al., 2012; Sakowska et al., 2015; Utsumi et al., 2018; Ueda et al., 2019). Measurements of the redox potentials revealed that the intermembrane space (-255 mV) is more oxidizing than the cytosol (-286 mV) or mitochondrial matrix (-296 mV) supporting oxidative folding of IMS imported proteins (Hu et al., 2008).

Apart from the role in import into mitochondria, the disulfide bond of the CHCH domain seems to have an additional function in MICOS regulation (Sakowska et al., 2015). Mic19 was found in different redox states in human and yeast mitochondria, whereas predominantly the oxidized form of Mic19, containing the intramolecular disulfide bond was present in the MICOS complex (Sakowska et al., 2015). Interestingly, mitochondria lacking Mic60 show reduced levels of oxidized Mic19 (Sakowska et al., 2015). Mic19 mutants, which were not able to form one or two disulfide bonds, displayed reduced binding efficiency to Mic60, resulting in decreased interactions between Mic60 and the Mic10 subcomplex as well as partially altered mitochondrial morphology (Sakowska et al., 2015; Darshi et al., 2012). In line with this, ITC experiments with $Mic60_{sol}$ and Mic19 demonstrated that the affinity is strongly reduced if the two cysteines of Mic19 are mutated to serines (Hessenberger et al., 2017).
The two new structures presented in this study help to explain the strong influence of the disulfide bond on the interaction between Mic60 and Mic19. Contacts between the mitofilin domain and the CHCH domain are predominantly mediated via hydrophobic interactions (Figure 29, Table 9). Single point mutations, located in both CHCH domain helices, disturbed the Mic60-Mic19 interaction, indicating that both helices are involved in the interaction (Figure 29). It seems that proper arrangement of the CHCH domain is a prerequisite for tight interaction, in which the disulfide bond stabilizes this conformation. In line with this idea, a variant of the Mitofilin_C-CHCH fusion construct, in which the two cysteines were mutated to valines, was completely digested by trypsin

within a very short time (data not shown). In contrast, the trypsin-treated wild-type Mitofilin_C-CHCH fragments were stable for several days (data not shown). This demonstrates that the disulfide bond is necessary for the tight interaction between mitofilin domain and CHCH domain protecting the complex from proteolytic digestion.

6.4. Role of the Mic60-Mic19 subcomplex in membrane curvature and cristae stabilization

Crystal structure analysis of proteins provides important insights into the architecture and cellular functions of eukaryotic protein complexes. In parallel to my work, Tobias Bock-Bierbaum crystallized the coiled-coil domain of the yeast *Lachancea thermotolerans* Mic60 (unpublished data). By combining our crystal structures and biochemical data, we propose the model of how the Mic60-Mic19 subcomplex acts in crista junction stabilization, as shown in Figure 45 (prepared by Dr. Erik Werner, RNS Berlin). The coiled-coil domain of Mic60 forms a tetramer consisting of two antiparallel dimers with elongated coiled-coil domains, whereas the monomer consists of one long and two small α-helices. In addition to the central coiled-coil domain, the model also contains the mitofilin domain of Mic60 in complex with the CHCH domain of Mic19 from *Chaetomium thermophilum* presented in this work. The LBS of Mic60 was previously shown to be involved in membrane interaction and deformation (Hessenberger et al., 2017), and my results indicate that positive residues of LBS1 and mitofilin domain might mediate membrane interaction (Figure 38, Figure 39). In our model, the Mic60 tetramer stretches over the crista junctions, enabling their stabilization. Two mitofilin dimers would be located on opposite sides of the coiled-coil to mediate membrane interaction. Such model is in line with my data, which assume that the coiled-coil domain of Mic60 forms a structural scaffold required for organization of the lipid binding sites (Figure 37, 6.2). Furthermore, such a model would rationalize the idea of how the MICOS complex could act as diffusion barrier in crista junctions (Perkins et al., 1997; Mannella, 2006).

The length of the coiled-coil domain of Mic60 varies between different species. In HeLa cells, an average crista junction diameter of 20 nm was observed, which is enlarged to about 32 nm in the absence of Mic60 (Stephan et al., 2020). For yeast, a crista junction

diameter of 12.5 - 17.5 nm has been reported (Rabl et al., 2009), closely matching the length of the coiled-coil domain in the crystal structure (approx. 14 nm). The range of Mic60 could be even larger *in vivo* compared to the crystal structure, as the two small helices of the coiled-coil domain seem to be flexible resulting in rearrangement in the Mic60-Mic19 complex.

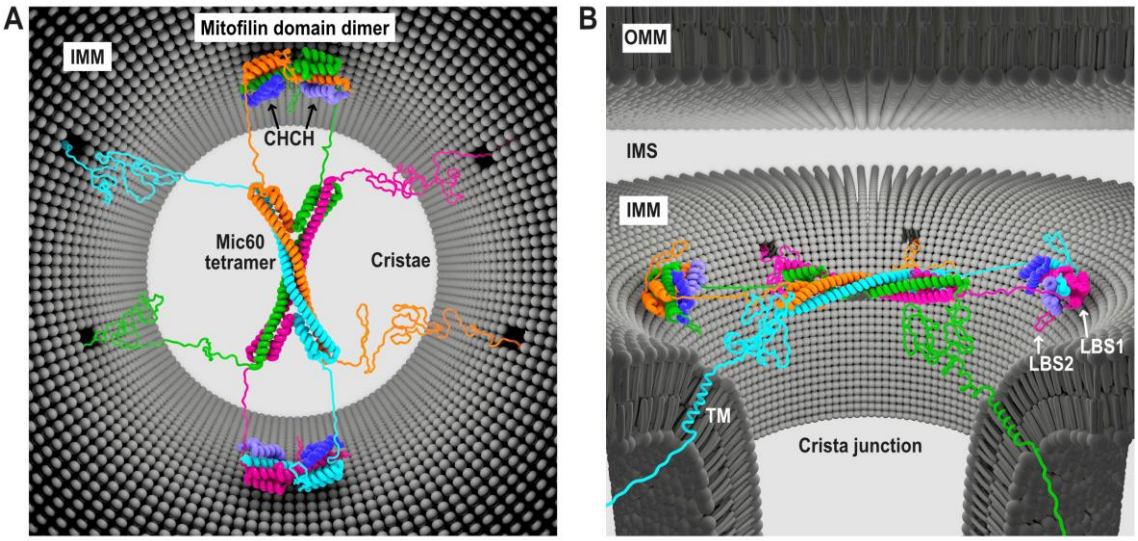

Figure 45: Model of Mic60 and CHCH domain in crista junctions. The model comprises the crystal structures of the coiled-coil domain of *Lachancea thermotolerans* Mic60 (Mic60 tetramer) of Tobias Bock-Bierbaum (MDC) and my *Chaetomium thermophilum* Mitofilin-CHCH_2 dimer (Mitofilin domain dimer; chains C and D). Regions not determined by X-ray crystallography are modeled as unstructured elements. The four Mic60 monomers are colored in pink, green, cyan and orange. The model contains four CHCH domains (CHCH) colored in blue and purple. A crista junction diameter of 17.5 nm was used (details in 4.4.5). **(A)** Top view. **(B)** Side view. IMM: inner mitochondrial membrane, IMS: intermembrane space, OMM: outer mitochondrial membrane, TM: transmembrane helix, LBS: lipid binding site. Copyright Dr. Erik Werner (2021), RNS Berlin (www.rns.berlin).

This model may also account for the assembly pathway of the Mic60-Mic19 subcomplex. The Mic60 coiled-coil dimer is the predominant oligomeric state of $Mic60_{sol}$ in solution (Figure 19, Figure 20; Hessenberger et al., 2017). Within the antiparallel dimer, the two mitofilin domains appear far away from each other and may

therefore be in a monomeric state. After Mic19 binding, tetramer formation of Mic60 and Mic19 is induced, in line with our biochemical experiments (Figure 19, C2). Furthermore, two mitofilin domains of adjacent dimers come into close proximity in the tetramer to form a crescent-shaped dimer (Figure 40). The membrane-binding site of the mitofilin domain dimer seems to be tailored to interact with the highly curved crista junction membrane (Figure 45, Figure 38). Furthermore, the dimeric state of the mitofilin domain seems to be important for the physiological function of Mic60, since conserved residues mediate dimer interface contacts (Figure 40, Figure 42, Figure 43). A single mutant in this interface, L676D, efficiently disrupted dimerization of the mitofilin domain (Figure 40). However, in an almost full-length context, the related mutant still tetramerized with Mic19, albeit with reduced efficiency (Figure 41). Combining L676D with a tetramerization mutant led to a protein that completely failed to form higher-order oligomers after co-incubation with Mic19 (Figure 41). These results indicate that formation of the Mic60 tetramer is linked to the formation of the mitofilin domain dimer, and both interfaces are required for the proper function of the Mic60-Mic19 complex.

The interaction between the two MICOS subcomplexes is supposed to be independent of the transmembrane domain of Mic60 (yeast), as replacement by a TM domain of a protein with the same topology does not change the overall mitochondrial morphology (Körner et al., 2012). It has been shown that deletion of the mitofilin domain dramatically reduced the co-purification of Mic60 with all other MICOS components resulting in abnormal mitochondrial ultrastructure (Körner et al., 2012; Zerbes et al., 2012). Hence, the mitofilin domain might play a crucial role in connecting both MICOS subcomplexes. Furthermore, cross-linking mass spectrometry experiments in mouse mitochondria revealed cross-links between the mitofilin domain of Mic60 and the C-terminus of Mic10, indicating close proximity of the mitofilin domain and the Mic10 subcomplex (Schweppe et al., 2017). In the same experiment, cross-links were obtained between Mic60 and Mic12, a small transmembrane protein which is thought to connect both subcomplexes (Guarani et al., 2015; Anand et al., 2016; Zerbes et al., 2016). Interestingly, these cross-links are located in the LBS of Mic60 and a predicted conserved amphipathic helix of Mic12 (Schweppe et al., 2017; Huynen et al., 2016). Based on our model of the position of Mic60-Mic19 in crista junctions, these results indicate that the Mic10-Mic12-Mic26-Mic27 subcomplex is located in close proximity to the mitofilin domain dimer.

Additionally, interactions of the Mic60-Mic19 subcomplex with the SAM and TOM complex, which are located in the outer mitochondrial membrane, have been reported (Darshi et al., 2011; Xie et al., 2007; von der Malsburg et al., 2011; Zerbes et al., 2012; Körner et al., 2012; Ott et al., 2015; Ding et al., 2015; Tang et al., 2020). More precisely, the mitofilin domain of Mic60 and the N-terminus of Mic19 seem to mediate these contacts (Körner et al., 2012; Darshi et al., 2011; Tang et al., 2020). It is proposed that the formation of crista junctions requires the integrity of the MICOS complex, whereas contact sites to the outer membrane are mediated via Mic60, Mic19 and the SAM complex (Ding et al., 2015; Tang et al., 2020). Importantly, our model of Mic60-Mic19 is consistent with MICOS forming a contact site: The N-terminal residues of Mic19 could extend from the mitofilin domain contact via the coiled-coil domain to the outer membrane to mediate the contact of the Mic19 N-terminus with the SAM complex.

As deletion of Mic19 resulted in significantly reduced interaction of Mic60 with other MICOS components, it was suggested that the MICOS subcomplexes are connected and regulated via Mic19 (Friedman et al., 2015; Sakowska et al., 2015). In our model, the tetramer is the cristae spanning form of Mic60, which needs to be activated by Mic19. It seems that Mic12 and Mic19 are both necessary for the connection between the subcomplexes: Mic12 via direct interactions with Mic60 and Mic19 as a regulator for Mic60 activation.

Altogether, our structural and functional data allowed the formulation of a model of how Mic60 and Mic19 might contribute to the formation of crista junctions in mitochondria. Thereby, it conveys a structural understanding of mitochondrial membrane organization.

6.5. Outlook

It has been suggested for several years that crista junctions limit the diffusion of certain metabolites and proteins between IMS and intracristal space (Perkins et al., 1997; Mannella, 2006). How this is achieved has remained, however, mostly unknown. Based on the structural and biochemical characterization of Mic60 and Mic19 obtained in this work and by Tobias Bock-Bierbaum, an active function of MICOS in limiting the

diffusion at crista junctions can be assumed. Thus, the Mic60 coiled-coil domain spanning across the crista junction may act as physical barrier that limits the space in the crista junctions and therefore prevents free diffusion across the crista junctions (Figure 46). Such mode of action could be directly tested by reconstituting membrane tubules with the Mic60-Mic19 complex in the interior and performing diffusion experiments, for example, with dextrans of different sizes.

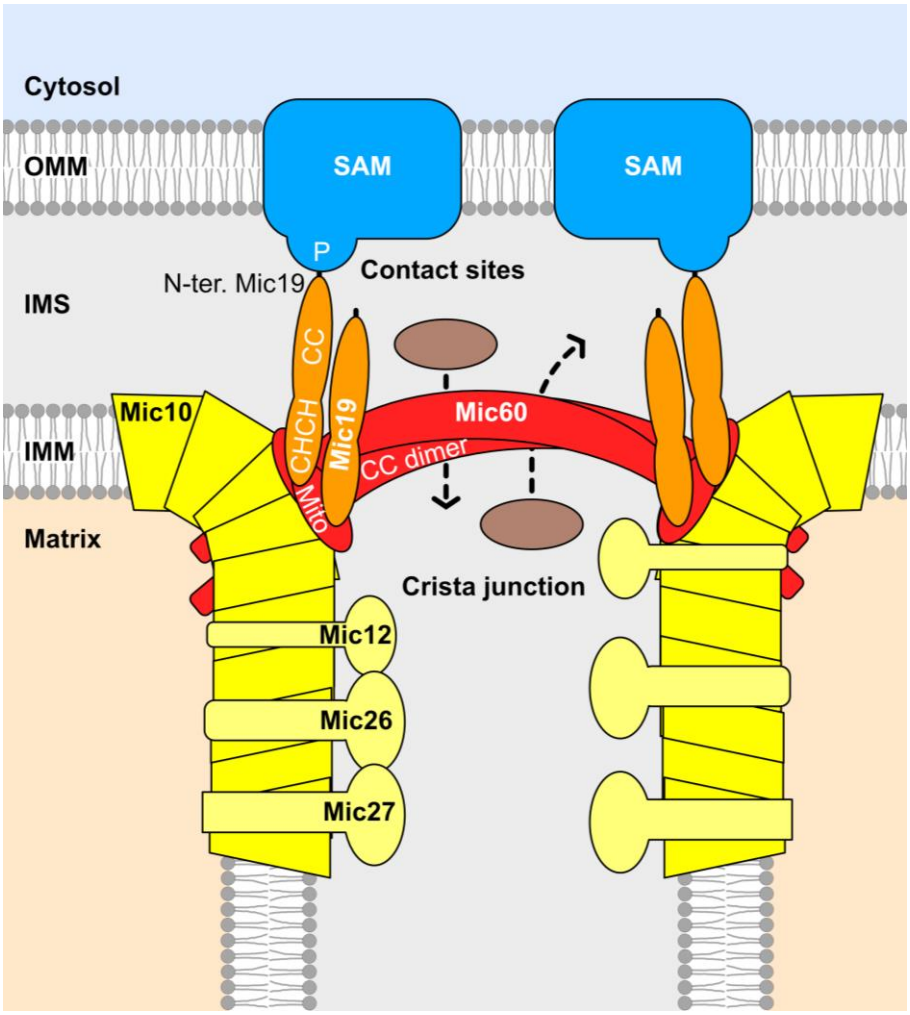

Figure 46: Schematic representation of the MICOS complex in crista junctions. Components of the yeast MICOS complex are shown. Two coiled-coil domain (CC) dimers of Mic60 stretch over the crista junction and form a tetramer. The mitofilin domain (Mito) of Mic60 interacts with the CHCH domain of Mic19, while Mic19 interacts via its N-terminus with the POTRA domain (P) of Sam50 of the SAM complex. The diffusion of certain metabolites and proteins (brown ellipses) is limited by Mic60. Mic10 oligomers induce membrane curvature at crista junctions. OMM: outer mitochondrial membrane, IMS: intermembrane space, IMM: inner mitochondrial membrane.

A second exciting line of research for future experiments is the role of MICOS as membrane contact site between the IMM and OMM. The previous experimental observation that the N-terminus of Mic19 interacts with the SAM complex in the OMM may constitute the structural basis of such contact site (Figure 46; Darshi et al., 2011; Bohnert et al., 2012; Utsumi et al., 2018). However, the exact 3D structure of the membrane contact site is still obscure; the proposed architecture of MICOS in Figure 46 suggests that it may adapt a structure resembling a molecular basket, e.g. similar to the nuclear pore architecture (Raices and D'Angelo, 2012). However, this model is still highly speculative and could be addressed by future cryo-electron tomography experiments of crista junctions within intact mitochondria or even with intact cells (Toro-Nahuelpan et al., 2020; Chakraborty et al., 2020).

Also the function of the contact site involving MICOS is still unclear: It may be envisaged that it mediates the sorting or even targeted delivery of imported proteins into the IMS or the crista lumen. If structural data of the contact site were available, such idea could be directly tested by a structure-function approach, e.g. by introducing mutations that specifically disrupt specific interfaces of the contact site, followed by functional experiments. For example, the delivery of imported, labelled proteins or dextrans into the crista lumen or IMS in such MICOS variants could be explored by using super resolution microscopy. These studies will be also key to delineate the mechanisms of how MICOS orchestrates the stabilization of crista junction architecture with crista junction functionality as a diffusion barrier.

7. References

Abe, Y., Shodai, T., Muto, T., Mihara, K., Torii, H., Nishikawa, S., Endo, T., and Kohda, D. (2000). Structural basis of presequence recognition by the mitochondrial protein import receptor Tom20. Cell *100*, 551-560.

Adams, P.D., Afonine, P.V., Bunkoczi, G., Chen, V.B., Davis, I.W., Echols, N., Headd, J.J., Hung, L.W., Kapral, G.J., Grosse-Kunstleve, R.W.*, et al.* (2010). PHENIX: a comprehensive Python-based system for macromolecular structure solution. Acta Crystallogr D Biol Crystallogr *66*, 213-221.

Afonine, P.V., Grosse-Kunstleve, R.W., Echols, N., Headd, J.J., Moriarty, N.W., Mustyakimov, M., Terwilliger, T.C., Urzhumtsev, A., Zwart, P.H., and Adams, P.D. (2012). Towards automated crystallographic structure refinement with phenix.refine. Acta Crystallogr D Biol Crystallogr *68*, 352-367.

Akabane, S., Uno, M., Tani, N., Shimazaki, S., Ebara, N., Kato, H., Kosako, H., and Oka, T. (2016). PKA Regulates PINK1 Stability and Parkin Recruitment to Damaged Mitochondria through Phosphorylation of MIC60. Mol Cell *62*, 371-384.

Alavian, K.N., Beutner, G., Lazrove, E., Sacchetti, S., Park, H.A., Licznerski, P., Li, H., Nabili, P., Hockensmith, K., Graham, M.*, et al.* (2014). An uncoupling channel within the c-subunit ring of the F1FO ATP synthase is the mitochondrial permeability transition pore. Proc Natl Acad Sci U S A *111*, 10580-10585.

Alexander, C., Votruba, M., Pesch, U.E., Thiselton, D.L., Mayer, S., Moore, A., Rodriguez, M., Kellner, U., Leo-Kottler, B., Auburger, G.*, et al.* (2000). OPA1, encoding a dynamin-related GTPase, is mutated in autosomal dominant optic atrophy linked to chromosome 3q28. Nat Genet *26*, 211-215.

Alkhaja, A.K., Jans, D.C., Nikolov, M., Vukotic, M., Lytovchenko, O., Ludewig, F., Schliebs, W., Riedel, D., Urlaub, H., Jakobs, S.*, et al.* (2012). MINOS1 is a conserved component of mitofilin complexes and required for mitochondrial function and cristae organization. Mol Biol Cell *23*, 247-257.

Amutha, B., Gordon, D.M., Gu, Y., and Pain, D. (2004). A novel role of Mgm1p, a dynamin-related GTPase, in ATP synthase assembly and cristae formation/maintenance. Biochem J *381*, 19-23.

An, J., Shi, J., He, Q., Lui, K., Liu, Y., Huang, Y., and Sheikh, M.S. (2012). CHCM1/CHCHD6, novel mitochondrial protein linked to regulation of mitofilin and mitochondrial cristae morphology. J Biol Chem *287*, 7411-7426.

Anand, R., Kondadi, A.K., Meisterknecht, J., Golombek, M., Nortmann, O., Riedel, J., Peifer-Weiss, L., Brocke-Ahmadinejad, N., Schlutermann, D., Stork, B.*, et al.* (2020). MIC26 and MIC27 cooperate to regulate cardiolipin levels and the landscape of OXPHOS complexes. Life Sci Alliance *3*.

Anand, R., Strecker, V., Urbach, J., Wittig, I., and Reichert, A.S. (2016). Mic13 Is Essential for Formation of Crista Junctions in Mammalian Cells. PLoS One *11*, e0160258.

Arnold, I., Pfeiffer, K., Neupert, W., Stuart, R.A., and Schagger, H. (1998). Yeast mitochondrial F1F0-ATP synthase exists as a dimer: identification of three dimer-specific subunits. EMBO J *17*, 7170-7178.

Ashkenazy, H., Abadi, S., Martz, E., Chay, O., Mayrose, I., Pupko, T., and Ben-Tal, N. (2016). ConSurf 2016: an improved methodology to estimate and visualize evolutionary conservation in macromolecules. Nucleic Acids Res *44*, W344-350.

Barbot, M., Jans, D.C., Schulz, C., Denkert, N., Kroppen, B., Hoppert, M., Jakobs, S., and Meinecke, M. (2015). Mic10 oligomerizes to bend mitochondrial inner membranes at cristae junctions. Cell Metab *21*, 756-763.

Barchiesi, A., and Vascotto, C. (2019). Transcription, Processing, and Decay of Mitochondrial RNA in Health and Disease. Int J Mol Sci *20*.

Baseler, W.A., Dabkowski, E.R., Williamson, C.L., Croston, T.L., Thapa, D., Powell, M.J., Razunguzwa, T.T., and Hollander, J.M. (2011). Proteomic alterations of distinct mitochondrial subpopulations in the type 1 diabetic heart: contribution of protein import dysfunction. Am J Physiol Regul Integr Comp Physiol *300*, R186-200.

Bayrhuber, M., Meins, T., Habeck, M., Becker, S., Giller, K., Villinger, S., Vonrhein, C., Griesinger, C., Zweckstetter, M., and Zeth, K. (2008). Structure of the human voltage-dependent anion channel. Proc Natl Acad Sci U S A *105*, 15370-15375.

Becker, T., Pfannschmidt, S., Guiard, B., Stojanovski, D., Milenkovic, D., Kutik, S., Pfanner, N., Meisinger, C., and Wiedemann, N. (2008). Biogenesis of the mitochondrial TOM complex: Mim1 promotes insertion and assembly of signal-anchored receptors. J Biol Chem *283*, 120-127.

Bernert, G., Fountoulakis, M., and Lubec, G. (2002). Manifold decreased protein levels of matrin 3, reduced motor protein HMP and hlark in fetal Down's syndrome brain. Proteomics *2*, 1752-1757.

Bhatti, J.S., Bhatti, G.K., and Reddy, P.H. (2017). Mitochondrial dysfunction and oxidative stress in metabolic disorders - A step towards mitochondria based therapeutic strategies. Biochim Biophys Acta Mol Basis Dis *1863*, 1066-1077.

Bibby, J., Keegan, R.M., Mayans, O., Winn, M.D., and Rigden, D.J. (2012). AMPLE: a cluster-and-truncate approach to solve the crystal structures of small proteins using rapidly computed ab initio models. Acta Crystallogr D Biol Crystallogr *68*, 1622-1631.

Bohnert, M., Wenz, L.S., Zerbes, R.M., Horvath, S.E., Stroud, D.A., von der Malsburg, K., Muller, J.M., Oeljeklaus, S., Perschil, I., Warscheid, B.*, et al.* (2012). Role of mitochondrial inner membrane organizing system in protein biogenesis of the mitochondrial outer membrane. Mol Biol Cell *23*, 3948-3956.

Bohnert, M., Zerbes, R.M., Davies, K.M., Muhleip, A.W., Rampelt, H., Horvath, S.E., Boenke, T., Kram, A., Perschil, I., Veenhuis, M.*, et al.* (2015). Central role of Mic10 in the mitochondrial contact site and cristae organizing system. Cell Metab *21*, 747-755.

Brandon, N.J., and Sawa, A. (2011). Linking neurodevelopmental and synaptic theories of mental illness through DISC1. Nat Rev Neurosci *12*, 707-722.

Buchan, D.W.A., and Jones, D.T. (2019). The PSIPRED Protein Analysis Workbench: 20 years on. Nucleic Acids Res *47*, W402-W407.

Cavallaro, G. (2010). Genome-wide analysis of eukaryotic twin CX9C proteins. Mol Biosyst *6*, 2459-2470.

Chacinska, A., Lind, M., Frazier, A.E., Dudek, J., Meisinger, C., Geissler, A., Sickmann, A., Meyer, H.E., Truscott, K.N., Guiard, B.*, et al.* (2005). Mitochondrial presequence translocase: switching between TOM tethering and motor recruitment involves Tim21 and Tim17. Cell *120*, 817-829.

Chacinska, A., Pfannschmidt, S., Wiedemann, N., Kozjak, V., Sanjuan Szklarz, L.K., Schulze-Specking, A., Truscott, K.N., Guiard, B., Meisinger, C., and Pfanner, N. (2004). Essential role of Mia40 in import and assembly of mitochondrial intermembrane space proteins. EMBO J *23*, 3735-3746.

Chakraborty, S., Mahamid, J., and Baumeister, W. (2020). Cryoelectron Tomography Reveals Nanoscale Organization of the Cytoskeleton and Its Relation to Microtubule Curvature Inside Cells. Structure *28*, 991-1003 e1004.

Chalk, R. (2017). Mass Spectrometric Analysis of Proteins. Methods Mol Biol *1586*, 373-395.

Chen, H., and Chan, D.C. (2009). Mitochondrial dynamics--fusion, fission, movement, and mitophagy--in neurodegenerative diseases. Hum Mol Genet *18*, R169-176.

Chen, V.B., Arendall, W.B., 3rd, Headd, J.J., Keedy, D.A., Immormino, R.M., Kapral, G.J., Murray, L.W., Richardson, J.S., and Richardson, D.C. (2010). MolProbity: all-atom structure validation for macromolecular crystallography. Acta Crystallogr D Biol Crystallogr *66*, 12-21.

Chojnacka, M., Gornicka, A., Oeljeklaus, S., Warscheid, B., and Chacinska, A. (2015). Cox17 Protein Is an Auxiliary Factor Involved in the Control of the Mitochondrial Contact Site and Cristae Organizing System. J Biol Chem *290*, 15304-15312.

Cipolat, S., Martins de Brito, O., Dal Zilio, B., and Scorrano, L. (2004). OPA1 requires mitofusin 1 to promote mitochondrial fusion. Proc Natl Acad Sci U S A *101*, 15927-15932.

Colina-Tenorio, L., Horten, P., Pfanner, N., and Rampelt, H. (2020). Shaping the mitochondrial inner membrane in health and disease. J Intern Med *287*, 645-664.

Collins, T.J., Berridge, M.J., Lipp, P., and Bootman, M.D. (2002). Mitochondria are morphologically and functionally heterogeneous within cells. EMBO J *21*, 1616-1627.

Corpet, F. (1988). Multiple sequence alignment with hierarchical clustering. Nucleic Acids Res *16*, 10881-10890.

Darshi, M., Mendiola, V.L., Mackey, M.R., Murphy, A.N., Koller, A., Perkins, G.A., Ellisman, M.H., and Taylor, S.S. (2011). ChChd3, an inner mitochondrial membrane protein, is essential for maintaining crista integrity and mitochondrial function. J Biol Chem *286*, 2918-2932.

Darshi, M., Trinh, K.N., Murphy, A.N., and Taylor, S.S. (2012). Targeting and import mechanism of coiled-coil helix coiled-coil helix domain-containing protein 3 (ChChd3) into the mitochondrial intermembrane space. J Biol Chem *287*, 39480-39491.

Davies, K.M., Anselmi, C., Wittig, I., Faraldo-Gomez, J.D., and Kuhlbrandt, W. (2012). Structure of the yeast F1Fo-ATP synthase dimer and its role in shaping the mitochondrial cristae. Proc Natl Acad Sci U S A *109*, 13602-13607.

Davies, K.M., Strauss, M., Daum, B., Kief, J.H., Osiewacz, H.D., Rycovska, A., Zickermann, V., and Kuhlbrandt, W. (2011). Macromolecular organization of ATP synthase and complex I in whole mitochondria. Proc Natl Acad Sci U S A *108*, 14121-14126.

Delettre, C., Lenaers, G., Griffoin, J.M., Gigarel, N., Lorenzo, C., Belenguer, P., Pelloquin, L., Grosgeorge, J., Turc-Carel, C., Perret, E*., et al.* (2000). Nuclear gene OPA1, encoding a mitochondrial dynamin-related protein, is mutated in dominant optic atrophy. Nat Genet *26*, 207-210.

Deng, H., Dodson, M.W., Huang, H., and Guo, M. (2008). The Parkinson's disease genes pink1 and parkin promote mitochondrial fission and/or inhibit fusion in Drosophila. Proc Natl Acad Sci U S A *105*, 14503-14508.

Devaux, P.F., Herrmann, A., Ohlwein, N., and Kozlov, M.M. (2008). How lipid flippases can modulate membrane structure. Biochim Biophys Acta *1778*, 1591-1600.

Dimmer, K.S., Papic, D., Schumann, B., Sperl, D., Krumpe, K., Walther, D.M., and Rapaport, D. (2012). A crucial role for Mim2 in the biogenesis of mitochondrial outer membrane proteins. J Cell Sci *125*, 3464-3473.

Ding, C., Wu, Z., Huang, L., Wang, Y., Xue, J., Chen, S., Deng, Z., Wang, L., Song, Z., and Chen, S. (2015). Mitofilin and CHCHD6 physically interact with Sam50 to sustain cristae structure. Sci Rep *5*, 16064.

Drews, G., and Golecki, J.R. (1995). Structure, Molecular Organization, and Biosynthesis of Membranes of Purple Bacteria. In: Blankenship, R.E., Madigan, M.T., Bauer, C.E. (eds) Anoxygenic Photosynthetic Bacteria. Advances in Photosynthesis and Respiration (Springer, Dordrecht),vol. 2, pp. 231-257.

Embley, T.M. (2006). Multiple secondary origins of the anaerobic lifestyle in eukaryotes. Philos Trans R Soc Lond B Biol Sci *361*, 1055-1067.

Emsley, P., Lohkamp, B., Scott, W.G., and Cowtan, K. (2010). Features and development of Coot. Acta Crystallogr D Biol Crystallogr *66*, 486-501.

Eydt, K., Davies, K.M., Behrendt, C., Wittig, I., and Reichert, A.S. (2017). Cristae architecture is determined by an interplay of the MICOS complex and the F1FO ATP synthase via Mic27 and Mic10. Microb Cell *4*, 259-272.

Faelber, K., Dietrich, L., Noel, J.K., Wollweber, F., Pfitzner, A.K., Muhleip, A., Sanchez, R., Kudryashev, M., Chiaruttini, N., Lilie, H.*, et al.* (2019). Structure and assembly of the mitochondrial membrane remodelling GTPase Mgm1. Nature *571*, 429-433.

Faelber, K., Posor, Y., Gao, S., Held, M., Roske, Y., Schulze, D., Haucke, V., Noe, F., and Daumke, O. (2011). Crystal structure of nucleotide-free dynamin. Nature *477*, 556-560.

Frezza, C., Cipolat, S., Martins de Brito, O., Micaroni, M., Beznoussenko, G.V., Rudka, T., Bartoli, D., Polishuck, R.S., Danial, N.N., De Strooper, B.*, et al.* (2006). OPA1 controls apoptotic cristae remodeling independently from mitochondrial fusion. Cell *126*, 177-189.

Friedman, J.R., Mourier, A., Yamada, J., McCaffery, J.M., and Nunnari, J. (2015). MICOS coordinates with respiratory complexes and lipids to establish mitochondrial inner membrane architecture. Elife *4*.

Fukada, K., Zhang, F., Vien, A., Cashman, N.R., and Zhu, H. (2004). Mitochondrial proteomic analysis of a cell line model of familial amyotrophic lateral sclerosis. Mol Cell Proteomics *3*, 1211-1223.

Gasteiger E., Hoogland C., Gattiker A., Duvaud S., Wilkins M.R., Appel R.D., and Bairoch A. (2005). Protein Identification and Analysis Tools on the ExPASy Server. In: John M. Walker (ed): The Proteomics Protocols Handbook (Humana Press), pp. 571-607.

Gerlach, M., Mueller, U., and Weiss, M.S., Helmholtz-Zentrum Berlin für Materialien und Energie (2016). The MX beamlines BL14.1-3 at BESSY II. Journal of large-scale research facilities, *2*, A47.

Gieffers, C., Korioth, F., Heimann, P., Ungermann, C., and Frey, J. (1997). Mitofilin is a transmembrane protein of the inner mitochondrial membrane expressed as two isoforms. Exp Cell Res *232*, 395-399.

Godiker, J., Gruneberg, M., DuChesne, I., Reunert, J., Rust, S., Westermann, C., Wada, Y., Classen, G., Langhans, C.D., Schlingmann, K.P.*, et al.* (2018). QIL1-dependent assembly of MICOS complex-lethal mutation in C19ORF70 resulting in liver disease and severe neurological retardation. J Hum Genet *63*, 707-716.

Guarani, V., Jardel, C., Chretien, D., Lombes, A., Benit, P., Labasse, C., Lacene, E., Bourillon, A., Imbard, A., Benoist, J.F.*, et al.* (2016). QIL1 mutation causes MICOS disassembly and early onset fatal mitochondrial encephalopathy with liver disease. Elife *5*.

Guarani, V., McNeill, E.M., Paulo, J.A., Huttlin, E.L., Frohlich, F., Gygi, S.P., Van Vactor, D., and Harper, J.W. (2015). QIL1 is a novel mitochondrial protein required for MICOS complex stability and cristae morphology. Elife *4*.

Hackenbrock, C.R. (1966). Ultrastructural bases for metabolically linked mechanical activity in mitochondria. I. Reversible ultrastructural changes with change in metabolic steady state in isolated liver mitochondria. J Cell Biol *30*, 269-297.

Hallermayer, G., and Neupert, W. (1974). Lipid composition of mitochondrial outer and inner membranes of Neurospora crassa. Hoppe Seylers Z Physiol Chem *355*, 279-288.

Harner, M., Körner, C., Walther, D., Mokranjac, D., Kaesmacher, J., Welsch, U., Griffith, J., Mann, M., Reggiori, F., and Neupert, W. (2011). The mitochondrial contact site complex, a determinant of mitochondrial architecture. EMBO J *30*, 4356-4370.

Harner, M.E., Unger, A.K., Izawa, T., Walther, D.M., Ozbalci, C., Geimer, S., Reggiori, F., Brugger, B., Mann, M., Westermann, B.*, et al.* (2014). Aim24 and MICOS modulate respiratory function, tafazzin-related cardiolipin modification and mitochondrial architecture. Elife *3*, e01684.

Hawlitschek, G., Schneider, H., Schmidt, B., Tropschug, M., Hartl, F.U., and Neupert, W. (1988). Mitochondrial protein import: identification of processing peptidase and of PEP, a processing enhancing protein. Cell *53*, 795-806.

Head, B.P., Zulaika, M., Ryazantsev, S., and van der Bliek, A.M. (2011). A novel mitochondrial outer membrane protein, MOMA-1, that affects cristae morphology in Caenorhabditis elegans. Mol Biol Cell *22*, 831-841.

Herrmann, J.M., and Riemer, J. (2012). Mitochondrial disulfide relay: redox-regulated protein import into the intermembrane space. J Biol Chem *287*, 4426-4433.

Hess, D.C., Myers, C.L., Huttenhower, C., Hibbs, M.A., Hayes, A.P., Paw, J., Clore, J.J., Mendoza, R.M., Luis, B.S., Nislow, C.*, et al.* (2009). Computationally driven, quantitative experiments discover genes required for mitochondrial biogenesis. PLoS Genet *5*, e1000407.

Hessenberger, M., Zerbes, R.M., Rampelt, H., Kunz, S., Xavier, A.H., Purfurst, B., Lilie, H., Pfanner, N., van der Laan, M., and Daumke, O. (2017). Regulated membrane remodeling by Mic60 controls formation of mitochondrial crista junctions. Nat Commun *8*, 15258.

Hill, K., Model, K., Ryan, M.T., Dietmeier, K., Martin, F., Wagner, R., and Pfanner, N. (1998). Tom40 forms the hydrophilic channel of the mitochondrial import pore for preproteins [see comment]. Nature *395*, 516-521.

Ho, S.N., Hunt, H.D., Horton, R.M., Pullen, J.K., and Pease, L.R. (1989). Site-directed mutagenesis by overlap extension using the polymerase chain reaction. Gene *77*, 51-59.

Höhr, A.I., Straub, S.P., Warscheid, B., Becker, T., and Wiedemann, N. (2015). Assembly of beta-barrel proteins in the mitochondrial outer membrane. Biochim Biophys Acta *1853*, 74-88.

Hopf, T.A., Green, A.G., Schubert, B., Mersmann, S., Scharfe, C.P.I., Ingraham, J.B., Toth-Petroczy, A., Brock, K., Riesselman, A.J., Palmedo, P.*, et al.* (2019). The EVcouplings Python framework for coevolutionary sequence analysis. Bioinformatics *35*, 1582-1584.

Hoppins, S., Collins, S.R., Cassidy-Stone, A., Hummel, E., Devay, R.M., Lackner, L.L., Westermann, B., Schuldiner, M., Weissman, J.S., and Nunnari, J. (2011). A mitochondrial-focused genetic interaction map reveals a scaffold-like complex required for inner membrane organization in mitochondria. J Cell Biol *195*, 323-340.

Horng, Y.C., Cobine, P.A., Maxfield, A.B., Carr, H.S., and Winge, D.R. (2004). Specific copper transfer from the Cox17 metallochaperone to both Sco1 and Cox11 in the assembly of yeast cytochrome C oxidase. J Biol Chem *279*, 35334-35340.

Horvath, S.E., Rampelt, H., Oeljeklaus, S., Warscheid, B., van der Laan, M., and Pfanner, N. (2015). Role of membrane contact sites in protein import into mitochondria. Protein Sci *24*, 277-297.

Hu, J., Dong, L., and Outten, C.E. (2008). The redox environment in the mitochondrial intermembrane space is maintained separately from the cytosol and matrix. J Biol Chem *283*, 29126-29134.

Hulett, J.M., Lueder, F., Chan, N.C., Perry, A.J., Wolynec, P., Likic, V.A., Gooley, P.R., and Lithgow, T. (2008). The transmembrane segment of Tom20 is recognized by Mim1 for docking to the mitochondrial TOM complex. J Mol Biol *376*, 694-704.

Huynen, M.A., Muhlmeister, M., Gotthardt, K., Guerrero-Castillo, S., and Brandt, U. (2016). Evolution and structural organization of the mitochondrial contact site (MICOS) complex and the mitochondrial intermembrane space bridging (MIB) complex. Biochim Biophys Acta *1863*, 91-101.

Hwang, H., Bowen, B.P., Lefort, N., Flynn, C.R., De Filippis, E.A., Roberts, C., Smoke, C.C., Meyer, C., Hojlund, K., Yi, Z.*, et al.* (2010). Proteomics analysis of human skeletal muscle reveals novel abnormalities in obesity and type 2 diabetes. Diabetes *59*, 33-42.

Icho, T., Ikeda, T., Matsumoto, Y., Hanaoka, F., Kaji, K., and Tsuchida, N. (1994). A novel human gene that is preferentially transcribed in heart muscle. Gene *144*, 301-306.

Ikon, N., and Ryan, R.O. (2017). Cardiolipin and mitochondrial cristae organization. Biochim Biophys Acta Biomembr *1859*, 1156-1163.

Itoh, K., Tamura, Y., Iijima, M., and Sesaki, H. (2013). Effects of Fcj1-Mos1 and mitochondrial division on aggregation of mitochondrial DNA nucleoids and organelle morphology. Mol Biol Cell *24*, 1842-1851.

Jans, D.C., Wurm, C.A., Riedel, D., Wenzel, D., Stagge, F., Deckers, M., Rehling, P., and Jakobs, S. (2013). STED super-resolution microscopy reveals an array of MINOS clusters along human mitochondria. Proc Natl Acad Sci U S A *110*, 8936-8941.

John, G.B., Shang, Y., Li, L., Renken, C., Mannella, C.A., Selker, J.M., Rangell, L., Bennett, M.J., and Zha, J. (2005). The mitochondrial inner membrane protein mitofilin controls cristae morphology. Mol Biol Cell *16*, 1543-1554.

Johnston, P.B., Gaster, R.N., Smith, V.C., and Tripathi, R.C. (1979). A clinicopathologic study of autosomal dominant optic atrophy. Am J Ophthalmol *88*, 868-875.

Jones, D.T. (1999). Protein secondary structure prediction based on position-specific scoring matrices. J Mol Biol *292*, 195-202.

Jurrus, E., Engel, D., Star, K., Monson, K., Brandi, J., Felberg, L.E., Brookes, D.H., Wilson, L., Chen, J., Liles, K., et al. (2018). Improvements to the APBS biomolecular solvation software suite. Protein Sci *27*, 112-128.

Kantardjieff, K.A., and Rupp, B. (2003). Matthews coefficient probabilities: Improved estimates for unit cell contents of proteins, DNA, and protein-nucleic acid complex crystals. Protein Sci *12*, 1865-1871.

Kärgel, E., Menzel, R., Honeck, H., Vogel, F., Bohmer, A., and Schunck, W.H. (1996). Candida maltosa NADPH-cytochrome P450 reductase: cloning of a full-length cDNA, heterologous expression in Saccharomyces cerevisiae and function of the N-terminal region for membrane anchoring and proliferation of the endoplasmic reticulum. Yeast *12*, 333-348.

Koehler, C.M., Jarosch, E., Tokatlidis, K., Schmid, K., Schweyen, R.J., and Schatz, G. (1998). Import of mitochondrial carriers mediated by essential proteins of the intermembrane space. Science *279*, 369-373.

Kondadi, A.K., Anand, R., Hansch, S., Urbach, J., Zobel, T., Wolf, D.M., Segawa, M., Liesa, M., Shirihai, O.S., Weidtkamp-Peters, S.*, et al.* (2020). Cristae undergo continuous cycles of membrane remodelling in a MICOS-dependent manner. EMBO Rep *21*, e49776.

Koob, S., Barrera, M., Anand, R., and Reichert, A.S. (2015). The non-glycosylated isoform of MIC26 is a constituent of the mammalian MICOS complex and promotes formation of crista junctions. Biochim Biophys Acta *1853*, 1551-1563.

Körner, C., Barrera, M., Dukanovic, J., Eydt, K., Harner, M., Rabl, R., Vogel, F., Rapaport, D., Neupert, W., and Reichert, A.S. (2012). The C-terminal domain of Fcj1 is required for formation of crista junctions and interacts with the TOB/SAM complex in mitochondria. Mol Biol Cell *23*, 2143-2155.

Krissinel, E., and Henrick, K. (2007). Inference of macromolecular assemblies from crystalline state. J Mol Biol *372*, 774-797.

Lamant, M., Smih, F., Harmancey, R., Philip-Couderc, P., Pathak, A., Roncalli, J., Galinier, M., Collet, X., Massabuau, P., Senard, J.M.*, et al.* (2006). ApoO, a novel apolipoprotein, is an original glycoprotein up-regulated by diabetes in human heart. J Biol Chem *281*, 36289-36302.

Landau, M., Mayrose, I., Rosenberg, Y., Glaser, F., Martz, E., Pupko, T., and Ben-Tal, N. (2005). ConSurf 2005: the projection of evolutionary conservation scores of residues on protein structures. Nucleic Acids Res *33*, W299-302.

Leigh, D. (1951). Subacute necrotizing encephalomyelopathy in an infant. J Neurol Neurosurg Psychiatry *14*, 216-221.

Lemasters, J.J. (2007). Modulation of mitochondrial membrane permeability in pathogenesis, autophagy and control of metabolism. J Gastroenterol Hepatol *22 Suppl 1*, S31-37.

Li, H., Ruan, Y., Zhang, K., Jian, F., Hu, C., Miao, L., Gong, L., Sun, L., Zhang, X., Chen, S.*, et al.* (2016). Mic60/Mitofilin determines MICOS assembly essential for mitochondrial dynamics and mtDNA nucleoid organization. Cell Death Differ *23*, 380-392.

Liebschner, D., Afonine, P.V., Baker, M.L., Bunkoczi, G., Chen, V.B., Croll, T.I., Hintze, B., Hung, L.W., Jain, S., McCoy, A.J.*, et al.* (2019). Macromolecular structure determination using X-rays, neutrons and electrons: recent developments in Phenix. Acta Crystallogr D Struct Biol *75*, 861-877.

Mannella, C.A. (2006). The relevance of mitochondrial membrane topology to mitochondrial function. Biochim Biophys Acta *1762*, 140-147.

Matthews, B.W. (1968). Solvent content of protein crystals. J Mol Biol *33*, 491-497.

McCoy, A.J., Grosse-Kunstleve, R.W., Adams, P.D., Winn, M.D., Storoni, L.C., and Read, R.J. (2007). Phaser crystallographic software. J Appl Crystallogr *40*, 658-674.

McMahon, H.T., and Boucrot, E. (2015). Membrane curvature at a glance. J Cell Sci *128*, 1065-1070.

McMahon, H.T., and Gallop, J.L. (2005). Membrane curvature and mechanisms of dynamic cell membrane remodelling. Nature *438*, 590-596.

Meeusen, S., DeVay, R., Block, J., Cassidy-Stone, A., Wayson, S., McCaffery, J.M., and Nunnari, J. (2006). Mitochondrial inner-membrane fusion and crista maintenance requires the dynamin-related GTPase Mgm1. Cell *127*, 383-395.

Modjtahedi, N., Tokatlidis, K., Dessen, P., and Kroemer, G. (2016). Mitochondrial Proteins Containing Coiled-Coil-Helix-Coiled-Coil-Helix (CHCH) Domains in Health and Disease. Trends Biochem Sci *41*, 245-260.

Mokranjac, D., and Neupert, W. (2010). The many faces of the mitochondrial TIM23 complex. Biochim Biophys Acta *1797*, 1045-1054.

Moriarty, N.W., Grosse-Kunstleve, R.W., and Adams, P.D. (2009). electronic Ligand Builder and Optimization Workbench (eLBOW): a tool for ligand coordinate and restraint generation. Acta Crystallogr D Biol Crystallogr *65*, 1074-1080.

Mueller, U., Förster, R., Hellmig, M., Huschmann, F.U., Kastner, A., Malecki, P., Pühringer, S., Röwer, M., Sparta, K., Steffien, M.*,* Ühlein, M., Wilk, P., and Weiss M. S. (2015). The macromolecular crystallography beamlines at BESSY II of the Helmholtz-Zentrum Berlin: Current status and perspectives. Eur Phys J Plus *130*, 141.

Mun, J.Y., Lee, T.H., Kim, J.H., Yoo, B.H., Bahk, Y.Y., Koo, H.S., and Han, S.S. (2010). Caenorhabditis elegans mitofilin homologs control the morphology of mitochondrial cristae and influence reproduction and physiology. J Cell Physiol *224*, 748-756.

Munoz-Gomez, S.A., Slamovits, C.H., Dacks, J.B., Baier, K.A., Spencer, K.D., and Wideman, J.G. (2015). Ancient homology of the mitochondrial contact site and cristae organizing system points to an endosymbiotic origin of mitochondrial cristae. Curr Biol *25*, 1489-1495.

Myung, J., Gulesserian, T., Fountoulakis, M., and Lubec, G. (2003). Deranged hypothetical proteins Rik protein, Nit protein 2 and mitochondrial inner membrane protein, Mitofilin, in fetal Down syndrome brain. Cell Mol Biol (Noisy-le-grand) *49*, 739-746.

Niyazov, D.M., Kahler, S.G., and Frye, R.E. (2016). Primary Mitochondrial Disease and Secondary Mitochondrial Dysfunction: Importance of Distinction for Diagnosis and Treatment. Mol Syndromol *7*, 122-137.

Odgren, P.R., Toukatly, G., Bangs, P.L., Gilmore, R., and Fey, E.G. (1996). Molecular characterization of mitofilin (HMP), a mitochondria-associated protein with predicted coiled-coil and intermembrane space targeting domains. J Cell Sci *109 (Pt 9)*, 2253-2264.

Olichon, A., Baricault, L., Gas, N., Guillou, E., Valette, A., Belenguer, P., and Lenaers, G. (2003). Loss of OPA1 perturbates the mitochondrial inner membrane structure and integrity, leading to cytochrome c release and apoptosis. J Biol Chem *278*, 7743-7746.

Olichon, A., Emorine, L.J., Descoins, E., Pelloquin, L., Brichese, L., Gas, N., Guillou, E., Delettre, C., Valette, A., Hamel, C.P.*, et al.* (2002). The human dynamin-related protein OPA1 is anchored to the mitochondrial inner membrane facing the inter-membrane space. FEBS Lett *523*, 171-176.

Olsen, J.V., Ong, S.E., and Mann, M. (2004). Trypsin cleaves exclusively C-terminal to arginine and lysine residues. Mol Cell Proteomics *3*, 608-614.

Ott, C., Dorsch, E., Fraunholz, M., Straub, S., and Kozjak-Pavlovic, V. (2015). Detailed analysis of the human mitochondrial contact site complex indicate a hierarchy of subunits. PLoS One *10*, e0120213.

Ott, C., Ross, K., Straub, S., Thiede, B., Gotz, M., Goosmann, C., Krischke, M., Mueller, M.J., Krohne, G., Rudel, T.*, et al.* (2012). Sam50 functions in mitochondrial intermembrane space bridging and biogenesis of respiratory complexes. Mol Cell Biol *32*, 1173-1188.

Palade, G.E. (1952). The fine structure of mitochondria. Anat Rec *114*, 427-451.

Paradies, G., Paradies, V., Ruggiero, F.M., and Petrosillo, G. (2019). Role of Cardiolipin in Mitochondrial Function and Dynamics in Health and Disease: Molecular and Pharmacological Aspects. Cells *8*.

Park, Y.U., Jeong, J., Lee, H., Mun, J.Y., Kim, J.H., Lee, J.S., Nguyen, M.D., Han, S.S., Suh, P.G., and Park, S.K. (2010). Disrupted-in-schizophrenia 1 (DISC1) plays essential roles in mitochondria in collaboration with Mitofilin. Proc Natl Acad Sci U S A *107*, 17785-17790.

Paumard, P., Vaillier, J., Coulary, B., Schaeffer, J., Soubannier, V., Mueller, D.M., Brethes, D., di Rago, J.P., and Velours, J. (2002). The ATP synthase is involved in generating mitochondrial cristae morphology. EMBO J *21*, 221-230.

Perkins, G., Renken, C., Martone, M.E., Young, S.J., Ellisman, M., and Frey, T. (1997). Electron tomography of neuronal mitochondria: three-dimensional structure and organization of cristae and membrane contacts. J Struct Biol *119*, 260-272.

Peter, B.J., Kent, H.M., Mills, I.G., Vallis, Y., Butler, P.J., Evans, P.R., and McMahon, H.T. (2004). BAR domains as sensors of membrane curvature: the amphiphysin BAR structure. Science *303*, 495-499.

Pfanner, N., van der Laan, M., Amati, P., Capaldi, R.A., Caudy, A.A., Chacinska, A., Darshi, M., Deckers, M., Hoppins, S., Icho, T.*, et al.* (2014). Uniform nomenclature for the mitochondrial contact site and cristae organizing system. J Cell Biol *204*, 1083-1086.

Pfanner, N., Warscheid, B., and Wiedemann, N. (2019). Mitochondrial proteins: from biogenesis to functional networks. Nat Rev Mol Cell Biol *20*, 267-284.

Pfanner, N., Warscheid, B., and Wiedemann, N. (2021). Author Correction: Mitochondrial proteins: from biogenesis to functional networks. Nat Rev Mol Cell Biol *22*, 367.

Pinero-Martos, E., Ortega-Vila, B., Pol-Fuster, J., Cisneros-Barroso, E., Ruiz-Guerra, L., Medina-Dols, A., Heine-Suner, D., Llado, J., Olmos, G., and Vives-Bauza, C. (2016). Disrupted in schizophrenia 1 (DISC1) is a constituent of the mammalian mitochondrial contact site and cristae organizing system (MICOS) complex, and is essential for oxidative phosphorylation. Hum Mol Genet *25*, 4157-4169.

Praefcke, G.J., and McMahon, H.T. (2004). The dynamin superfamily: universal membrane tubulation and fission molecules? Nat Rev Mol Cell Biol *5*, 133-147.

Rabl, R., Soubannier, V., Scholz, R., Vogel, F., Mendl, N., Vasiljev-Neumeyer, A., Körner, C., Jagasia, R., Keil, T., Baumeister, W.*, et al.* (2009). Formation of cristae and crista junctions in mitochondria depends on antagonism between Fcj1 and Su e/g. J Cell Biol *185*, 1047-1063.

Raices, M., and D'Angelo, M.A. (2012). Nuclear pore complex composition: a new regulator of tissue-specific and developmental functions. Nat Rev Mol Cell Biol *13*, 687-699.

Rampelt, H., Bohnert, M., Zerbes, R.M., Horvath, S.E., Warscheid, B., Pfanner, N., and van der Laan, M. (2017a). Mic10, a Core Subunit of the Mitochondrial Contact Site and Cristae Organizing System, Interacts with the Dimeric F1Fo-ATP Synthase. J Mol Biol *429*, 1162-1170.

Rampelt, H., Wollweber, F., Gerke, C., de Boer, R., van der Klei, I.J., Bohnert, M., Pfanner, N., and van der Laan, M. (2018). Assembly of the Mitochondrial Cristae Organizer Mic10 Is Regulated by Mic26-Mic27 Antagonism and Cardiolipin. J Mol Biol *430*, 1883-1890.

Rampelt, H., Zerbes, R.M., van der Laan, M., and Pfanner, N. (2017b). Role of the mitochondrial contact site and cristae organizing system in membrane architecture and dynamics. Biochim Biophys Acta Mol Cell Res *1864*, 737-746.

Reddy Chichili, V.P., Kumar, V., and Sivaraman, J. (2013). Linkers in the structural biology of protein-protein interactions. Protein Sci *22*, 153-167.

Rehling, P., Brandner, K., and Pfanner, N. (2004). Mitochondrial import and the twin-pore translocase. Nat Rev Mol Cell Biol *5*, 519-530.

Reichert, A.S., and Neupert, W. (2002). Contact sites between the outer and inner membrane of mitochondria-role in protein transport. Biochim Biophys Acta *1592*, 41-49.

Roger, A.J., Munoz-Gomez, S.A., and Kamikawa, R. (2017). The Origin and Diversification of Mitochondria. Curr Biol *27*, R1177-R1192.

Roise, D., Horvath, S.J., Tomich, J.M., Richards, J.H., and Schatz, G. (1986). A chemically synthesized pre-sequence of an imported mitochondrial protein can form an amphiphilic helix and perturb natural and artificial phospholipid bilayers. EMBO J *5*, 1327-1334.

Rossi, M.N., Carbone, M., Mostocotto, C., Mancone, C., Tripodi, M., Maione, R., and Amati, P. (2009). Mitochondrial localization of PARP-1 requires interaction with mitofilin and is involved in the maintenance of mitochondrial DNA integrity. J Biol Chem *284*, 31616-31624.

Ruhoy, I.S., and Saneto, R.P. (2014). The genetics of Leigh syndrome and its implications for clinical practice and risk management. Appl Clin Genet *7*, 221-234.

Sakowska, P., Jans, D.C., Mohanraj, K., Riedel, D., Jakobs, S., and Chacinska, A. (2015). The Oxidation Status of Mic19 Regulates MICOS Assembly. Mol Cell Biol *35*, 4222-4237.

Sambrook, J., Fritsch, E.F., and Maniatis, T. (1989). Molecular Cloning: A Laboratory Manual (Cold Spring Harbor Laboratory Press).

Schauble, S., King, C.C., Darshi, M., Koller, A., Shah, K., and Taylor, S.S. (2007). Identification of ChChd3 as a novel substrate of the cAMP-dependent protein kinase (PKA) using an analog-sensitive catalytic subunit. J Biol Chem *282*, 14952-14959.

Schneider, C.A., Rasband, W.S., and Eliceiri, K.W. (2012). NIH Image to ImageJ: 25 years of image analysis. Nat Methods *9*, 671-675.

Schuck, P. (2000). Size-distribution analysis of macromolecules by sedimentation velocity ultracentrifugation and lamm equation modeling. Biophys J *78*, 1606-1619.

Schweppe, D.K., Chavez, J.D., Lee, C.F., Caudal, A., Kruse, S.E., Stuppard, R., Marcinek, D.J., Shadel, G.S., Tian, R., and Bruce, J.E. (2017). Mitochondrial protein interactome elucidated by chemical cross-linking mass spectrometry. Proc Natl Acad Sci U S A *114*, 1732-1737.

Scorrano, L., Ashiya, M., Buttle, K., Weiler, S., Oakes, S.A., Mannella, C.A., and Korsmeyer, S.J. (2002). A distinct pathway remodels mitochondrial cristae and mobilizes cytochrome c during apoptosis. Dev Cell *2*, 55-67.

Seigneuret, M., and Devaux, P.F. (1984). ATP-dependent asymmetric distribution of spin-labeled phospholipids in the erythrocyte membrane: relation to shape changes. Proc Natl Acad Sci U S A *81*, 3751-3755.

Sheldrick, G.M. (2008). A short history of SHELX. Acta Crystallogr A *64*, 112-122.

Shibata, Y., Hu, J., Kozlov, M.M., and Rapoport, T.A. (2009). Mechanisms shaping the membranes of cellular organelles. Annu Rev Cell Dev Biol *25*, 329-354.

Shimada, A., Niwa, H., Tsujita, K., Suetsugu, S., Nitta, K., Hanawa-Suetsugu, K., Akasaka, R., Nishino, Y., Toyama, M., Chen, L.*, et al.* (2007). Curved EFC/F-BAR-domain dimers are joined end to end into a filament for membrane invagination in endocytosis. Cell *129*, 761-772.

Sickmann, A., Reinders, J., Wagner, Y., Joppich, C., Zahedi, R., Meyer, H.E., Schonfisch, B., Perschil, I., Chacinska, A., Guiard, B.*, et al.* (2003). The proteome of Saccharomyces cerevisiae mitochondria. Proc Natl Acad Sci U S A *100*, 13207-13212.

Sievers, F., Wilm, A., Dineen, D., Gibson, T.J., Karplus, K., Li, W., Lopez, R., McWilliam, H., Remmert, M., Soding, J.*, et al.* (2011). Fast, scalable generation of high-quality protein multiple sequence alignments using Clustal Omega. Mol Syst Biol *7*, 539.

Sikorski, R.S., and Hieter, P. (1989). A system of shuttle vectors and yeast host strains designed for efficient manipulation of DNA in Saccharomyces cerevisiae. Genetics *122*, 19-27.

Sirrenberg, C., Bauer, M.F., Guiard, B., Neupert, W., and Brunner, M. (1996). Import of carrier proteins into the mitochondrial inner membrane mediated by Tim22. Nature *384*, 582-585.

Sjostrand, F.S. (1953). Electron microscopy of mitochondria and cytoplasmic double membranes. Nature *171*, 30-32.

Slot, J.W., and Geuze, H.J. (2007). Cryosectioning and immunolabeling. Nat Protoc *2*, 2480-2491.

Sparta, K.M., Krug, M., Heinemann, U., Mueller, U., and Weiss, M.S. (2016). XDSAPP2.0. J Appl Cryst *49*, 1085-1092.

St Clair, D., Blackwood, D., Muir, W., Carothers, A., Walker, M., Spowart, G., Gosden, C., and Evans, H.J. (1990). Association within a family of a balanced autosomal translocation with major mental illness. Lancet *336*, 13-16.

Stephan, T., Bruser, C., Deckers, M., Steyer, A.M., Balzarotti, F., Barbot, M., Behr, T.S., Heim, G., Hubner, W., Ilgen, P.*, et al.* (2020). MICOS assembly controls mitochondrial inner membrane remodeling and crista junction redistribution to mediate cristae formation. EMBO J *39*, e104105.

Strauss, M., Hofhaus, G., Schroder, R.R., and Kuhlbrandt, W. (2008). Dimer ribbons of ATP synthase shape the inner mitochondrial membrane. EMBO J *27*, 1154-1160.

Tang, J., Zhang, K., Dong, J., Yan, C., Hu, C., Ji, H., Chen, L., Chen, S., Zhao, H., and Song, Z. (2020). Sam50-Mic19-Mic60 axis determines mitochondrial cristae architecture by mediating mitochondrial outer and inner membrane contact. Cell Death Differ *27*, 146-160.

Tarasenko, D., Barbot, M., Jans, D.C., Kroppen, B., Sadowski, B., Heim, G., Mobius, W., Jakobs, S., and Meinecke, M. (2017). The MICOS component Mic60 displays a conserved membrane-bending activity that is necessary for normal cristae morphology. J Cell Biol *216*, 889-899.

Taylor, A.B., Smith, B.S., Kitada, S., Kojima, K., Miyaura, H., Otwinowski, Z., Ito, A., and Deisenhofer, J. (2001). Crystal structures of mitochondrial processing peptidase reveal the mode for specific cleavage of import signal sequences. Structure *9*, 615-625.

Taylor, S.W., Fahy, E., Zhang, B., Glenn, G.M., Warnock, D.E., Wiley, S., Murphy, A.N., Gaucher, S.P., Capaldi, R.A., Gibson, B.W.*, et al.* (2003). Characterization of the human heart mitochondrial proteome. Nat Biotechnol *21*, 281-286.

Terwilliger, T.C., Grosse-Kunstleve, R.W., Afonine, P.V., Moriarty, N.W., Zwart, P.H., Hung, L.W., Read, R.J., and Adams, P.D. (2008). Iterative model building, structure refinement and density modification with the PHENIX AutoBuild wizard. Acta Crystallogr D Biol Crystallogr *64*, 61-69.

Thomas, J.M., Keegan, R.M., Bibby, J., Winn, M.D., Mayans, O., and Rigden, D.J. (2015). Routine phasing of coiled-coil protein crystal structures with AMPLE. IUCrJ *2*, 198-206.

Thorn, A., and Sheldrick, G.M. (2013). Extending molecular-replacement solutions with SHELXE. Acta Crystallogr D Biol Crystallogr *69*, 2251-2256.

Tirrell, P.S., Nguyen, K.N., Luby-Phelps, K., and Friedman, J.R. (2020). MICOS subcomplexes assemble independently on the mitochondrial inner membrane in proximity to ER contact sites. J Cell Biol *219*.

Tokuyasu, K.T. (1973). A technique for ultracryotomy of cell suspensions and tissues. J Cell Biol *57*, 551-565.

Toro-Nahuelpan, M., Zagoriy, I., Senger, F., Blanchoin, L., Thery, M., and Mahamid, J. (2020). Tailoring cryo-electron microscopy grids by photo-micropatterning for in-cell structural studies. Nat Methods *17*, 50-54.

Tsai, P.I., Lin, C.H., Hsieh, C.H., Papakyrikos, A.M., Kim, M.J., Napolioni, V., Schoor, C., Couthouis, J., Wu, R.M., Wszolek, Z.K.*, et al.* (2018). PINK1 Phosphorylates MIC60/Mitofilin to Control Structural Plasticity of Mitochondrial Crista Junctions. Mol Cell *69*, 744-756 e746.

Tucker, J.D., Siebert, C.A., Escalante, M., Adams, P.G., Olsen, J.D., Otto, C., Stokes, D.L., and Hunter, C.N. (2010). Membrane invagination in Rhodobacter sphaeroides is initiated at curved regions of the cytoplasmic membrane, then forms both budded and fully detached spherical vesicles. Mol Microbiol *76*, 833-847.

Turkieh, A., Caubere, C., Barutaut, M., Desmoulin, F., Harmancey, R., Galinier, M., Berry, M., Dambrin, C., Polidori, C., Casteilla, L.*, et al.* (2014). Apolipoprotein O is mitochondrial and promotes lipotoxicity in heart. J Clin Invest *124*, 2277-2286.

Ueda, E., Tamura, Y., Sakaue, H., Kawano, S., Kakuta, C., Matsumoto, S., and Endo, T. (2019). Myristoyl group-aided protein import into the mitochondrial intermembrane space. Sci Rep *9*, 1185.

Utsumi, T., Matsuzaki, K., Kiwado, A., Tanikawa, A., Kikkawa, Y., Hosokawa, T., Otsuka, A., Iuchi, Y., Kobuchi, H., and Moriya, K. (2018). Identification and characterization of protein N-myristoylation occurring on four human mitochondrial proteins, SAMM50, TOMM40, MIC19, and MIC25. PLoS One *13*, e0206355.

Valente, E.M., Salvi, S., Ialongo, T., Marongiu, R., Elia, A.E., Caputo, V., Romito, L., Albanese, A., Dallapiccola, B., and Bentivoglio, A.R. (2004). PINK1 mutations are associated with sporadic early-onset parkinsonism. Ann Neurol *56*, 336-341.

van der Laan, M., Horvath, S.E., and Pfanner, N. (2016). Mitochondrial contact site and cristae organizing system. Curr Opin Cell Biol *41*, 33-42.

Van Laar, V.S., Dukes, A.A., Cascio, M., and Hastings, T.G. (2008). Proteomic analysis of rat brain mitochondria following exposure to dopamine quinone: implications for Parkinson disease. Neurobiol Dis *29*, 477-489.

Van Laar, V.S., Otero, P.A., Hastings, T.G., and Berman, S.B. (2018). Potential Role of Mic60/Mitofilin in Parkinson's Disease. Front Neurosci *12*, 898.

Varabyova, A., Topf, U., Kwiatkowska, P., Wrobel, L., Kaus-Drobek, M., and Chacinska, A. (2013). Mia40 and MINOS act in parallel with Ccs1 in the biogenesis of mitochondrial Sod1. FEBS J *280*, 4943-4959.

Vögtle, F.N., Wortelkamp, S., Zahedi, R.P., Becker, D., Leidhold, C., Gevaert, K., Kellermann, J., Voos, W., Sickmann, A., Pfanner, N.*, et al.* (2009). Global analysis of the mitochondrial N-proteome identifies a processing peptidase critical for protein stability. Cell *139*, 428-439.

von der Malsburg, K., Muller, J.M., Bohnert, M., Oeljeklaus, S., Kwiatkowska, P., Becker, T., Loniewska-Lwowska, A., Wiese, S., Rao, S., Milenkovic, D.*, et al.* (2011). Dual role of mitofilin in mitochondrial membrane organization and protein biogenesis. Dev Cell *21*, 694-707.

Vonck, J., von Nidda, T.K., Meier, T., Matthey, U., Mills, D.J., Kuhlbrandt, W., and Dimroth, P. (2002). Molecular architecture of the undecameric rotor of a bacterial Na+-ATP synthase. J Mol Biol *321*, 307-316.

Votruba, M., Fitzke, F.W., Holder, G.E., Carter, A., Bhattacharya, S.S., and Moore, A.T. (1998). Clinical features in affected individuals from 21 pedigrees with dominant optic atrophy. Arch Ophthalmol *116*, 351-358.

Wagner, F., Kunz, T.C., Chowdhury, S.R., Thiede, B., Fraunholz, M., Eger, D., and Kozjak-Pavlovic, V. (2019). Armadillo repeat-containing protein 1 is a dual localization protein associated with mitochondrial intermembrane space bridging complex. PLoS One *14*, e0218303.

Wang, Q., Liu, Y., Zou, X., Wang, Q., An, M., Guan, X., He, J., Tong, Y., and Ji, J. (2008). The hippocampal proteomic analysis of senescence-accelerated mouse: implications of Uchl3 and mitofilin in cognitive disorder and mitochondria dysfunction in SAMP8. Neurochem Res *33*, 1776-1782.

Weber, T.A., Koob, S., Heide, H., Wittig, I., Head, B., van der Bliek, A., Brandt, U., Mittelbronn, M., and Reichert, A.S. (2013). APOOL is a cardiolipin-binding constituent of the Mitofilin/MINOS protein complex determining cristae morphology in mammalian mitochondria. PLoS One *8*, e63683.

Weichenberger, C.X., and Rupp, B. (2014). Ten years of probabilistic estimates of biocrystal solvent content: new insights via nonparametric kernel density estimate. Acta Crystallogr D Biol Crystallogr *70*, 1579-1588.

Weihofen, A., Thomas, K.J., Ostaszewski, B.L., Cookson, M.R., and Selkoe, D.J. (2009). Pink1 forms a multiprotein complex with Miro and Milton, linking Pink1 function to mitochondrial trafficking. Biochemistry *48*, 2045-2052.

Westermann, B. (2010). Mitochondrial fusion and fission in cell life and death. Nat Rev Mol Cell Biol *11*, 872-884.

Wiedemann, N., Kozjak, V., Chacinska, A., Schonfisch, B., Rospert, S., Ryan, M.T., Pfanner, N., and Meisinger, C. (2003). Machinery for protein sorting and assembly in the mitochondrial outer membrane. Nature *424*, 565-571.

Wiedemann, N., and Pfanner, N. (2017). Mitochondrial Machineries for Protein Import and Assembly. Annu Rev Biochem *86*, 685-714.

Williams, C.J., Headd, J.J., Moriarty, N.W., Prisant, M.G., Videau, L.L., Deis, L.N., Verma, V., Keedy, D.A., Hintze, B.J., Chen, V.B.*, et al.* (2018). MolProbity: More and better reference data for improved all-atom structure validation. Protein Sci *27*, 293-315.

Winn, M.D., Ballard, C.C., Cowtan, K.D., Dodson, E.J., Emsley, P., Evans, P.R., Keegan, R.M., Krissinel, E.B., Leslie, A.G., McCoy, A.*, et al.* (2011). Overview of the CCP4 suite and current developments. Acta Crystallogr D Biol Crystallogr *67*, 235-242.

Wishart, T.M., Paterson, J.M., Short, D.M., Meredith, S., Robertson, K.A., Sutherland, C., Cousin, M.A., Dutia, M.B., and Gillingwater, T.H. (2007). Differential proteomics analysis of synaptic proteins identifies potential cellular targets and protein mediators of synaptic neuroprotection conferred by the slow Wallerian degeneration (Wlds) gene. Mol Cell Proteomics *6*, 1318-1330.

Wolf, D.M., Segawa, M., Kondadi, A.K., Anand, R., Bailey, S.T., Reichert, A.S., van der Bliek, A.M., Shackelford, D.B., Liesa, M., and Shirihai, O.S. (2019). Individual cristae within the same mitochondrion display different membrane potentials and are functionally independent. EMBO J *38*, e101056.

Xie, J., Marusich, M.F., Souda, P., Whitelegge, J., and Capaldi, R.A. (2007). The mitochondrial inner membrane protein mitofilin exists as a complex with SAM50, metaxins 1 and 2, coiled-coil-helix coiled-coil-helix domain-containing protein 3 and 6 and DnaJC11. FEBS Lett *581*, 3545-3549.

Yamaguchi, R., Lartigue, L., Perkins, G., Scott, R.T., Dixit, A., Kushnareva, Y., Kuwana, T., Ellisman, M.H., and Newmeyer, D.D. (2008). Opa1-mediated cristae opening is Bax/Bak and BH3 dependent, required for apoptosis, and independent of Bak oligomerization. Mol Cell *31*, 557-569.

Yu, B.L., Wu, C.L., and Zhao, S.P. (2012). Plasma apolipoprotein O level increased in the patients with acute coronary syndrome. J Lipid Res *53*, 1952-1957.

Zeharia, A., Friedman, J.R., Tobar, A., Saada, A., Konen, O., Fellig, Y., Shaag, A., Nunnari, J., and Elpeleg, O. (2016). Mitochondrial hepato-encephalopathy due to deficiency of QIL1/MIC13 (C19orf70), a MICOS complex subunit. Eur J Hum Genet *24*, 1778-1782.

Zerbes, R.M., Bohnert, M., Stroud, D.A., von der Malsburg, K., Kram, A., Oeljeklaus, S., Warscheid, B., Becker, T., Wiedemann, N., Veenhuis, M.*, et al.* (2012). Role of MINOS in mitochondrial membrane architecture: cristae morphology and outer membrane interactions differentially depend on mitofilin domains. J Mol Biol *422*, 183-191.

Zerbes, R.M., Hoss, P., Pfanner, N., van der Laan, M., and Bohnert, M. (2016). Distinct Roles of Mic12 and Mic27 in the Mitochondrial Contact Site and Cristae Organizing System. J Mol Biol *428*, 1485-1492.

Zick, M., Rabl, R., and Reichert, A.S. (2009). Cristae formation-linking ultrastructure and function of mitochondria. Biochim Biophys Acta *1793*, 5-19.

Züchner, S., Mersiyanova, I.V., Muglia, M., Bissar-Tadmouri, N., Rochelle, J., Dadali, E.L., Zappia, M., Nelis, E., Patitucci, A., Senderek, J.*, et al.* (2004). Mutations in the mitochondrial GTPase mitofusin 2 cause Charcot-Marie-Tooth neuropathy type 2A. Nat Genet *36*, 449-451.

Appendix

A. Abbreviations

ADP	Adenosine diphosphate
AEBSF	4-(2-aminoethyl)benzenesulfonyl fluoride
ATP	Adenosine triphosphate
AU	Arbitrary unit
AUC	Analytical ultracentrifugation
BICINE	*N,N*-Bis(2-hydroxyethyl)glycine
bp	Base pair(s)
C-terminus	Carboxy-terminus
CHCH	Coiled-coil-helix-coiled-coil-helix
Ct/ct	*Chaetomium thermophilum*
DMSO	Dimethyl sulfoxide
DNA	Deoxyribonucleic acid
DTT	Dithiothreitol
E. coli	*Escherichia coli*
EDTA	Ethylenediaminetetraacetic acid
ER	Endoplasmic reticulum
HEPES	4-(2-hydroxyethyl)-1-piperazineethanesulfonic acid
HPLC	High-performance liquid chromatography
IMAC	Immobilized metal ion affinity chromatography
IMM	Inner mitochondrial membrane
IMS	Intermembrane space
IPTG	Isopropyl β-D-1-thiogalactopyranoside
ITC	Isothermal titration calorimetry
K_D	Dissociation constant
LB	Lysogeny broth (medium)
LBS	Lipid binding site
LC-ESI-Q-TOF-MS	Liquid chromatography-electrospray ionization-quadrupole-time of flight-mass spectrometry
MDC	Max-Delbrück-Centrum für Molekulare Medizin in der Helmholtz-Gemeinschaft (Berlin)
MES	2-(*N*-morpholino)ethanesulfonic acid

MIA	Mitochondrial intermembrane space import and assembly
MICOS	Mitochondrial contact site and cristae organizing system
MPD	Hexylene glycol, 2-Methyl-2,4-pentanediol
mtDNA	Mitochondrial DNA
MW	Molecular weight
MWCO	Molecular weight cut-off
n	Binding number
N-terminus	Amino-terminus
Ni-NTA	Nickel-nitrilotriacetic acid (nickel-charged resin)
OD_{600}	Optical density, measured at 600 nm
OMM	Outer mitochondrial membrane
OPA1	Optic atrophy 1 protein
P	Pellet
PAGE	Polyacrylamide gel electrophoresis
PCR	Polymerase chain reaction
PEG	Polyethylene glycol
PEG MME	Polyethylene glycol monomethyl ether
PINK1	PTEN-induced kinase 1
PKA	cAMP-dependent protein kinase
RALS	Right-angle light scattering
RMSD	Root-mean-square deviation
SAM	Sorting and assembly machinery
Sc/sc	*Saccharomyces cerevisiae*
SDS	Sodium dodecyl sulfate
SDS-PAGE	Sodium dodecyl sulfate polyacrylamide gel electrophoresis
SEC	Size exclusion chromatography
SEC-RALS	Size exclusion chromatography coupled to right-angle light scattering
SN	Supernatant
TAE	Tris/Acetate/EDTA (buffer)
TB	Terrific broth (medium)
TBE	Tris/Borate/EDTA (buffer)
TIM	Translocase of the inner membrane
TM	Transmembrane
TMANO	Trimethylamine N-oxide

TOM	Translocase of the outer membrane
TRIS	Tris-(hydroxymethyl)-amino methane
U	Unit
VDAC	Voltage-dependent anion channel
v/v	Volume per volume
w/v	Weight per volume
w/w	Weight per weight
X-ray	X-radiation (high-energy electromagnetic radiation)

One letter code and three letter code for amino acids

A	Ala	Alanine	I	Ile	Isoleucine	R	Arg	Arginine
C	Cys	Cysteine	K	Lys	Lysine	S	Ser	Serine
D	Asp	Aspartate	L	Leu	Leucine	T	Thr	Threonine
E	Glu	Glutamate	M	Met	Methionine	V	Val	Valine
F	Phe	Phenylalanine	N	Asn	Asparagine	W	Trp	Tryptophane
G	Gly	Glycine	P	Pro	Proline	Y	Tyr	Tyrosine
H	His	Histidine	Q	Gln	Glutamine			

Units

M, mM, µM	Amount of substance (mole)
Da, kDa, MDa	Atomic mass unit (dalton)
eV, keV	Energy (electron-volt)
mm, nm, Å	Length
g, mg, µg, ng	Mass
rpm	Rotational speed (revolutions per minute)
x g	Degree of acceleration in multiples of g (g-force)
°C, K	Temperature
h, min, s	Time
l, ml, µl	Volume

B. Chemicals

Acetic acid (ROTIPURAN®, 100%)	Carl Roth GmbH + Co. KG (Karlsruhe, Germany)
AEBSF Hydrochloride BioChemica	AppliChem GmbH (Darmstadt, Germany)
Agar-Agar Kobe I, powdered	Carl Roth GmbH + Co. KG (Karlsruhe, Germany)
Agarose for DNA Electrophoresis	SERVA Electrophoresis GmbH (Heidelberg, Germany)
Ampicillin sodium salt (≥ 97%)	Carl Roth GmbH + Co. KG (Karlsruhe, Germany)
BICINE (≥ 99%)	Sigma-Aldrich (St. Louis, USA)
Boric acid (≥ 99.8%)	Carl Roth GmbH + Co. KG (Karlsruhe, Germany)
Brain extract from bovine brain, type I, Folch fraction I	Sigma-Aldrich (St. Louis, USA)
Bromophenol blue sodium salt	Carl Roth GmbH + Co. KG (Karlsruhe, Germany)
Calcium chloride dihydrate (≥ 99.5%)	Sigma-Aldrich (St. Louis, USA)
Carbenicillin disodium salt (≥ 88%)	Carl Roth GmbH + Co. KG (Karlsruhe, Germany)
Chloroform (EMSURE®)	Merck KGaA (Darmstadt, Germany)
Citric acid anhydrous	Sigma-Aldrich (St. Louis, USA)
Coomassie® Brilliant Blue R-250	Carl Roth GmbH + Co. KG (Karlsruhe, Germany)
Decon™ Decon 90	Fisher Scientific GmbH (Schwerte, Germany)
DMSO (≥ 99.5%)	Carl Roth GmbH + Co. KG (Karlsruhe, Germany)
dNTP Set	Bioline, Meridian Bioscience (Cincinnati, USA)
DTT (1,4-Dithiothreitol, ≥ 99%)	Carl Roth GmbH + Co. KG (Karlsruhe, Germany)
EDTA disodium salt dihydrate (≥ 99%)	Carl Roth GmbH + Co. KG (Karlsruhe, Germany)
Ethanol (≥ 99,8%, denatured)	Carl Roth GmbH + Co. KG (Karlsruhe, Germany)
Ethanol (ROTIPURAN®, ≥ 99,8%)	Carl Roth GmbH + Co. KG (Karlsruhe, Germany)
Ethidium bromide solution (1%)	Carl Roth GmbH + Co. KG (Karlsruhe, Germany)
Glycerol (ROTIPURAN®, ≥ 99,5%, anhydrous)	Carl Roth GmbH + Co. KG (Karlsruhe, Germany)
HEPES (PUFFERAN®, ≥ 99.5%)	Carl Roth GmbH + Co. KG (Karlsruhe, Germany)
Hydrochloric acid (32%, extra pure)	Carl Roth GmbH + Co. KG (Karlsruhe, Germany)
Imidazole (PUFFERAN®, ≥ 99%)	Carl Roth GmbH + Co. KG (Karlsruhe, Germany)
IPTG (≥ 99%)	Carl Roth GmbH + Co. KG (Karlsruhe, Germany)
Jeffamine® M-600 (No. 422118)	Sigma-Aldrich (St. Louis, USA)

Kanamycin sulphate (≥ 750 I.U./mg)	Carl Roth GmbH + Co. KG (Karlsruhe, Germany)
Magnesium chloride hexahydrate (≥ 99%)	Sigma-Aldrich (St. Louis, USA)
β-Mercaptoethanol (≥ 99%)	Carl Roth GmbH + Co. KG (Karlsruhe, Germany)
MES monohydrate (≥ 99%)	Sigma-Aldrich (St. Louis, USA)
Methanol (EMSURE®)	Merck KGaA (Darmstadt, Germany)
Methanol (≥ 99.8%)	Th. Geyer GmbH & Co. KG (Renningen, Germany)
MPD, Hexylene glycol (≥ 99%)	Sigma-Aldrich (St. Louis, USA)
Nickel(II) sulfate hexahydrate (≥ 99.0%, crystallized)	Sigma-Aldrich (St. Louis, USA)
Poly(ethylene glycol) (PEG), BioUltra 6,000 and 8,000	Sigma-Aldrich (St. Louis, USA)
Potassium dihydrogen phosphate (≥ 99%)	Carl Roth GmbH + Co. KG (Karlsruhe, Germany)
di-Potassium hydrogen phosphate (≥ 99%, anhydrous)	Carl Roth GmbH + Co. KG (Karlsruhe, Germany)
2-Propanol (ROTIPURAN® ≥ 99,8%)	Carl Roth GmbH + Co. KG (Karlsruhe, Germany)
SDS (≥ 99%, pellets)	Carl Roth GmbH + Co. KG (Karlsruhe, Germany)
Silica gel orange (2-5 mm)	Carl Roth GmbH + Co. KG (Karlsruhe, Germany)
Sodium acetate (≥ 99.0%)	Sigma-Aldrich (St. Louis, USA)
Sodium chloride (≥ 99.8%)	Carl Roth GmbH + Co. KG (Karlsruhe, Germany)
Sodium citrate tribasic dihydrate (≥ 99.5%)	Sigma-Aldrich (St. Louis, USA)
Sodium dihydrogen phosphate dihydrate (≥ 99%)	Carl Roth GmbH + Co. KG (Karlsruhe, Germany)
di-Sodium hydrogen phosphate (≥ 99%, anhydrous)	Carl Roth GmbH + Co. KG (Karlsruhe, Germany)
Sodium hydroxide (≥ 98%, pellets)	Carl Roth GmbH + Co. KG (Karlsruhe, Germany)
Sodium hydroxide solution (ROTIPURAN® ≥ 32%)	Carl Roth GmbH + Co. KG (Karlsruhe, Germany)
Terrific Broth, Modified (Powder)	Melford Laboratories Ltd. (Ipswich, United Kingdom)
TRIS (PUFFERAN®, ≥ 99,9%)	Carl Roth GmbH + Co. KG (Karlsruhe, Germany)
Tryptone / Peptone ex Casein	Carl Roth GmbH + Co. KG (Karlsruhe, Germany)
Yeast Extract (powdered)	Carl Roth GmbH + Co. KG (Karlsruhe, Germany)

C. Secondary structure predictions

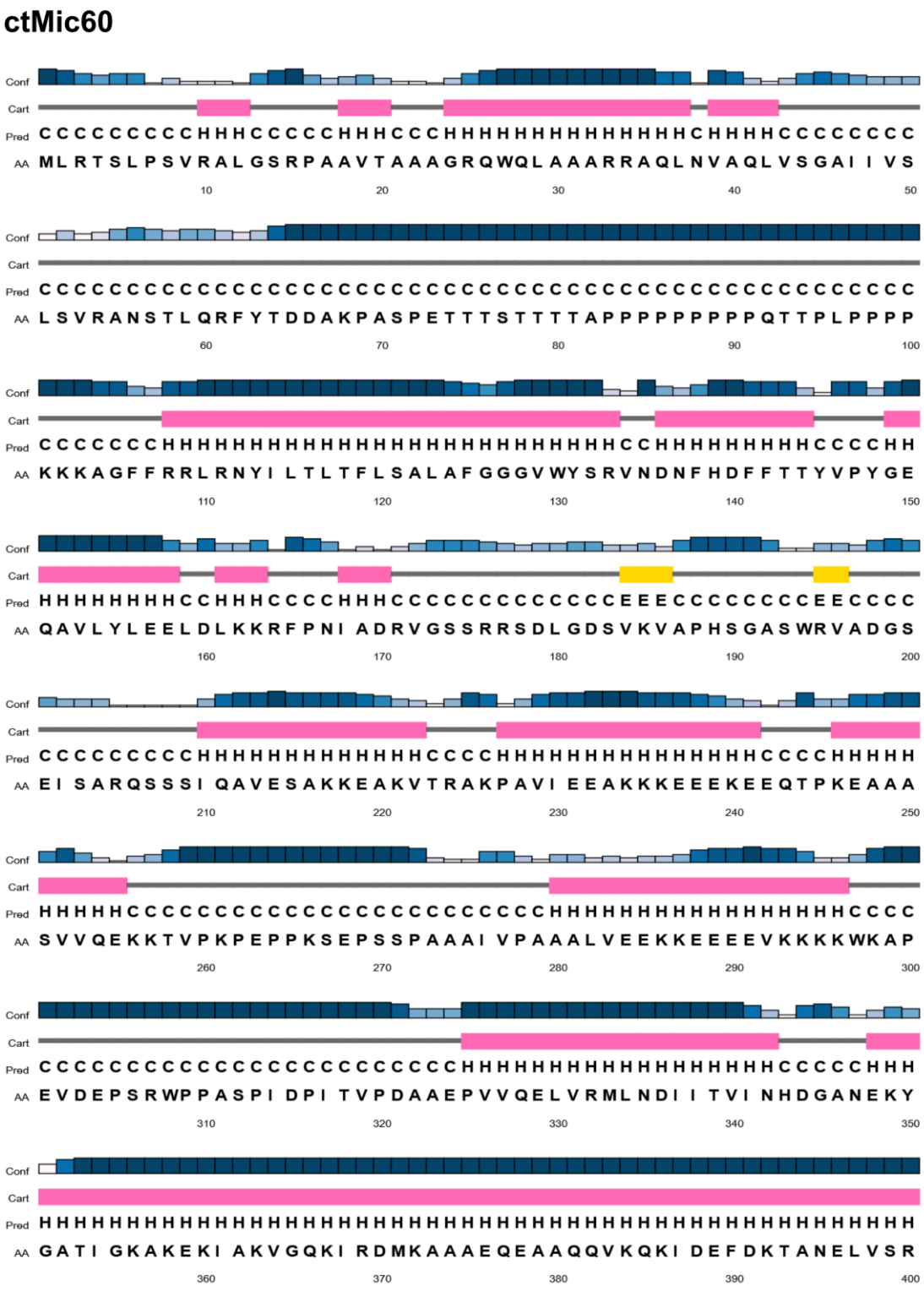

Figure C.1: Secondary structure prediction of ctMic60, part 1. *PSIPRED* result (Buchan and Jones, 2019; Jones, 1999; 03/2020).

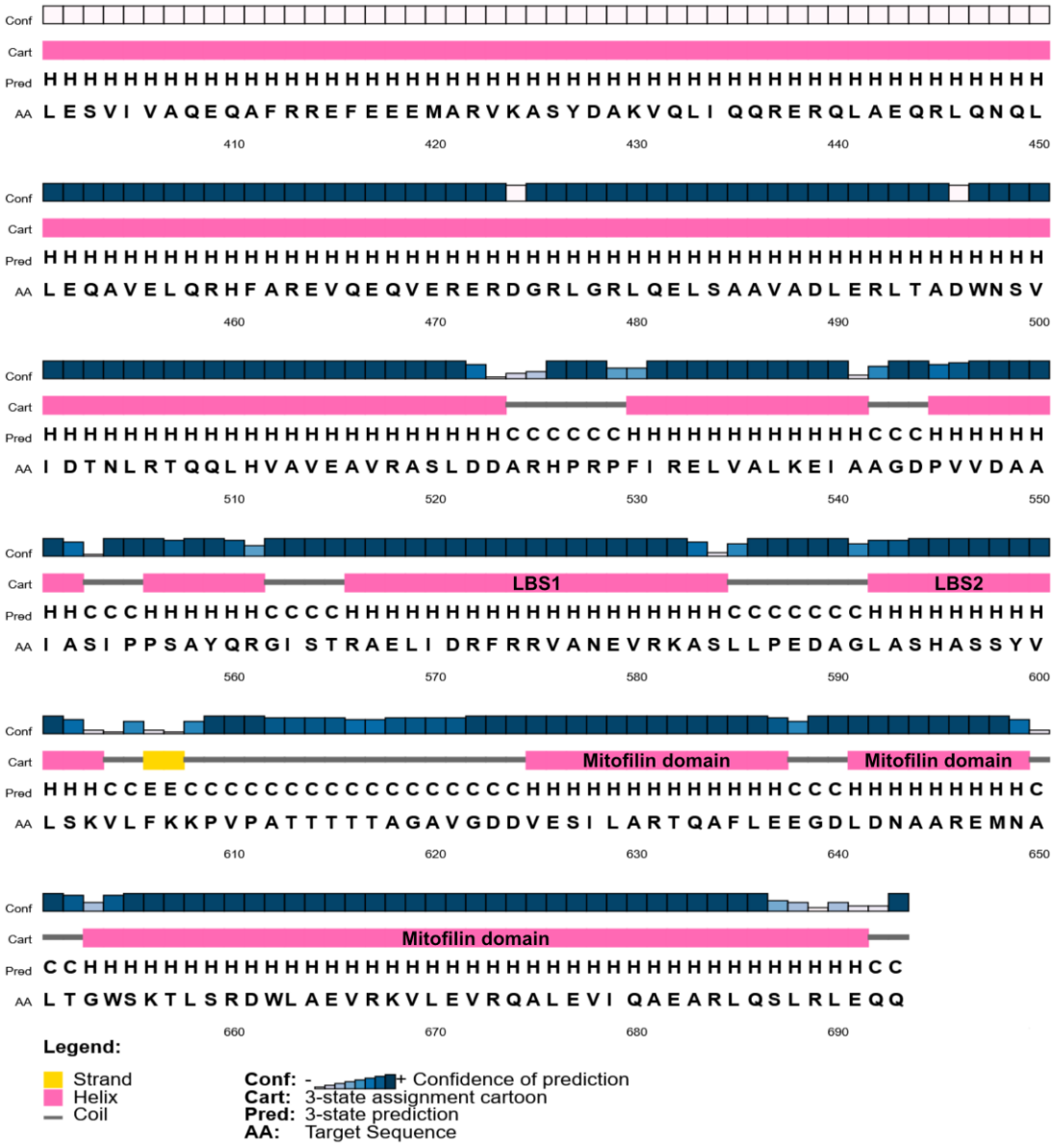

Figure C.2: Secondary structure prediction of ctMic60, part 2. *PSIPRED* result (Buchan and Jones, 2019; Jones, 1999; 03/2020). LBS1, LBS2 and mitofilin domain are labelled.

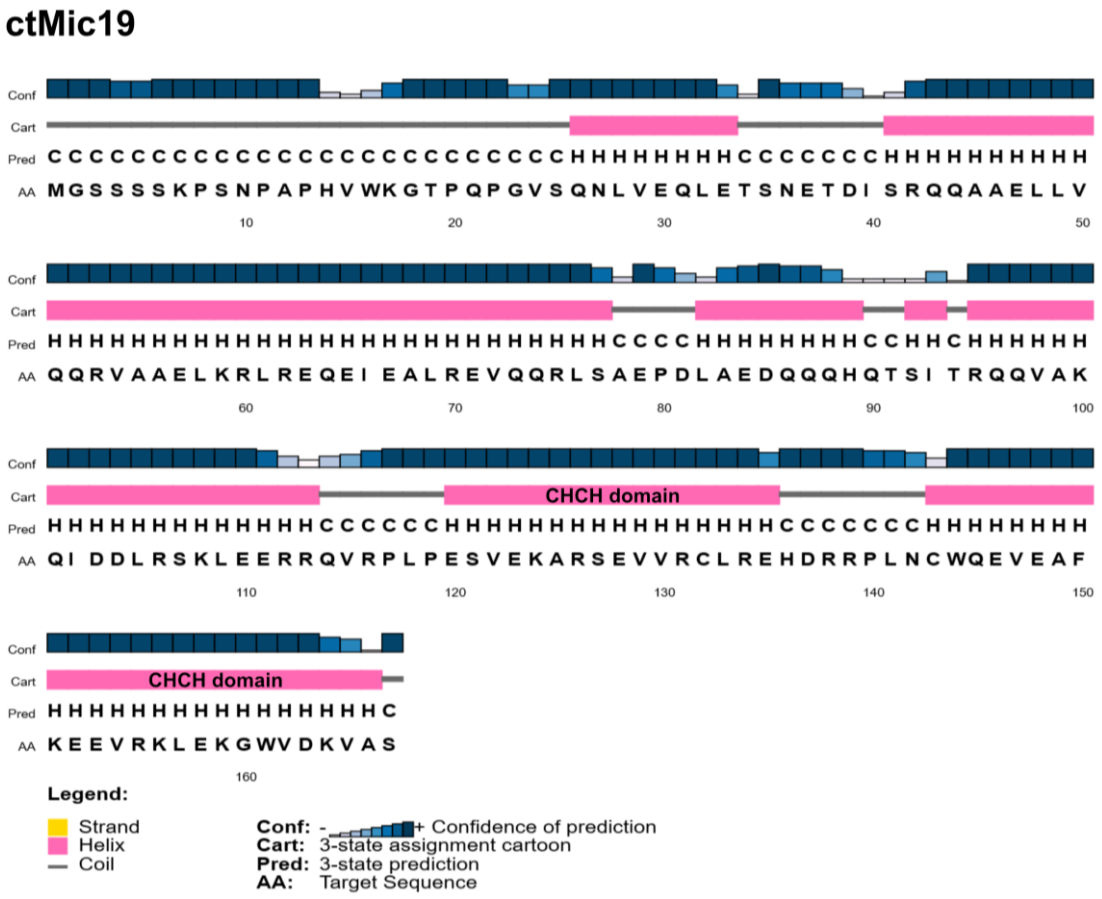

Figure C.3: Secondary structure predictions of ctMic19 and Mitofilin-CHCH_2. *PSIPRED* results (Buchan and Jones, 2019; Jones, 1999; 03/2020). LBS1, mitofilin domain and CHCH domain are labelled. Mitofilin-CHCH_2 after removal of the His_6-tag; GP: vector derived.

D. SEC-RALS result

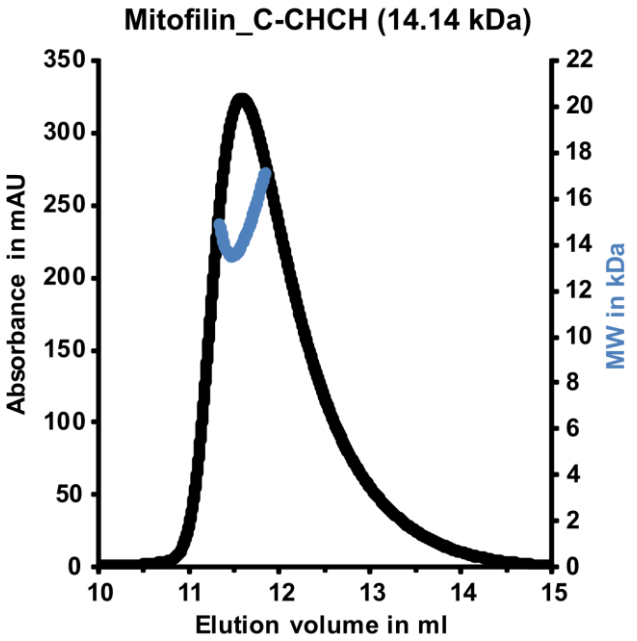

Figure D.1: SEC-RALS result of Mitofilin_C-CHCH. An ÄKTApurifier chromatography system was coupled to a RALS-refractive index detector (Malvern) and connected to a Superdex 75 10/300 GL column (GE Healthcare). 100 µl of a 3 mg/ml protein solution was applied. The peak area is shown. Absorption was measured at 280 nm (primary y-axis, black curve). Data were analyzed with OmniSec software v5.00 (Malvern). Blue curve: calculated molecular weight (MW) in kDa (secondary y-axis); the peak tip ±0.25 ml is depicted. MW of the monomer is indicated in parentheses (calculated with ProtParam, ExPASy Server (Gasteiger et al., 2005)).

E. Mass spectrometry results

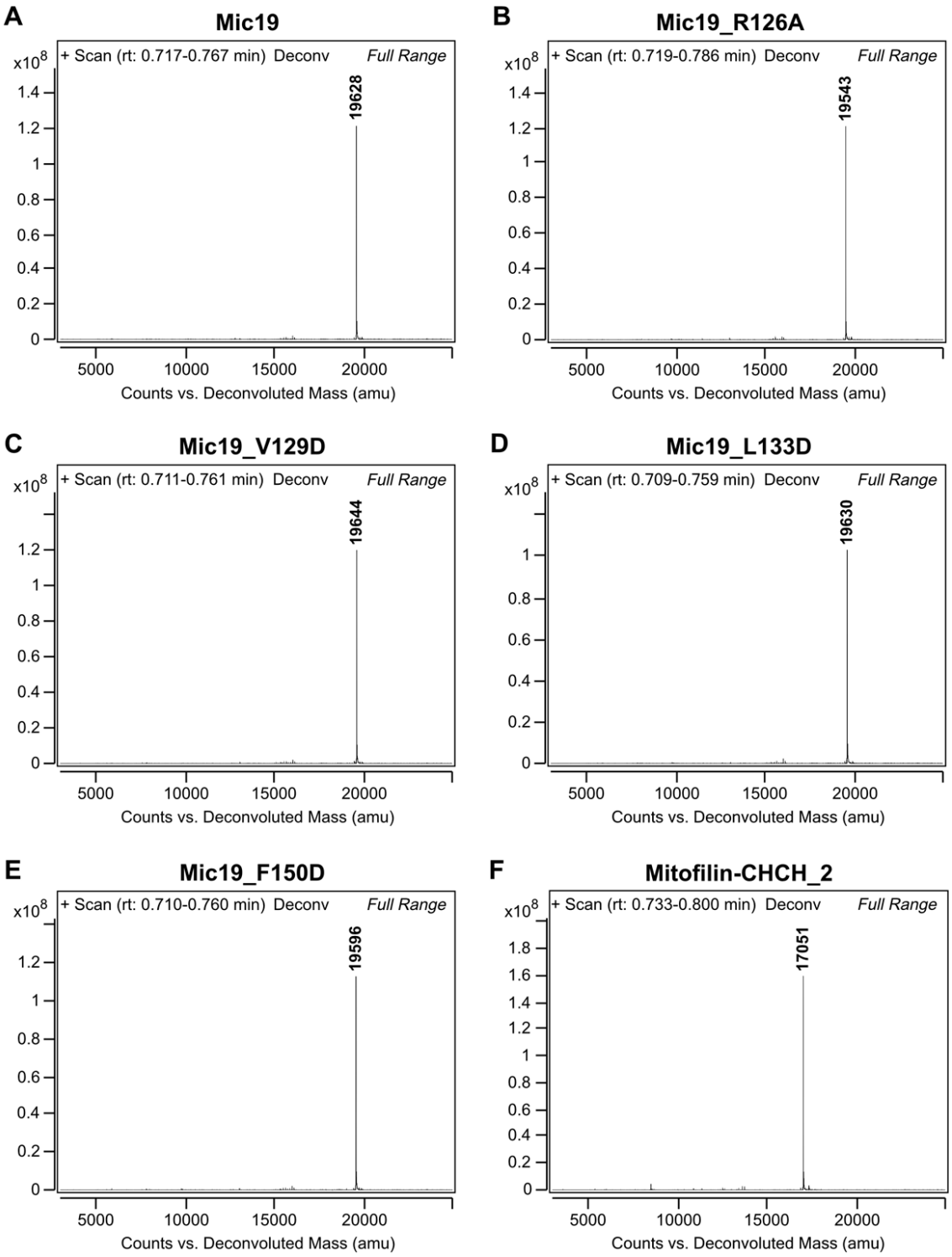

Figure E.1: Mass spectrometry (LC-ESI-Q-TOF-MS) deconvoluted spectra of Mic19 constructs and Mitofilin-CHCH_2. Numbers above the peaks show the molecular mass in Da. The results indicate that the disulfide bond of the CHCH domain is formed in all analyzed constructs. Experiments were performed at the Protein Production & Characterization Platform at MDC, supported by Anja Schütz.

Danksagung

Mein erster Dank gilt Prof. Dr. Oliver Daumke für die Möglichkeit, in seiner Arbeitsgruppe meine Doktorarbeit anfertigen und an diesem spannenden Projekt arbeiten zu können. Ich danke ihm sehr für die hervorragende Betreuung und seine vielen hilfreichen Ratschläge.

Ich möchte mich bei Prof. Dr. Udo Heinemann für die vielen nützlichen Tipps und Hinweise in unseren gemeinsamen Gruppentreffen bedanken. Auch durch den Besuch seiner ausführlichen Strukturbiologievorlesungen konnte ich mein Wissen erweitern. Zusätzlich danke ich Prof. Dr. Udo Heinemann für die Übernahme des Zweitgutachtens.

Besonders möchte ich Tobias Bock-Bierbaum und Manuel Hessenberger für die großartige Zusammenarbeit an unserem gemeinsamen Projekt danken. Die umfangreichen Diskussionen und Ratschläge haben mir bei meiner Forschungsarbeit sehr geholfen.

Des Weiteren möchte ich Yvette Roske für die Hilfe bei der Aufnahme der Diffraktionsdaten am Elektronenspeicherring BESSY II (Berlin-Adlershof, Deutschland) danken und natürlich auch dem Helmholtz-Zentrum Berlin für den Zugang.

Ein besonderer Dank gilt Martin van der Laan und den Arbeitsgruppenmitgliedern Florian Wollweber, Janina Laborenz, Alexander von der Malsburg, Karina von der Malsburg und Sibylle Jungbluth für die gute Zusammenarbeit, den wissenschaftlichen Austausch und die vielen hilfreichen Diskussionen.

Ich bedanke mich bei Elisa Lisicki für die Analyse und ausführliche Quantifizierung der Hefe-Mitochondrien und bei Dr. Hauke Lilie für die Analyse meiner Proteine mittels analytischer Ultrazentrifugation. Des Weiteren möchte ich mich bei Dr. Erik Werner für die Anfertigung des Modells von Mic60-Mic19 bedanken.

Außerdem möchte ich den MDC Technologie-Plattformen Elektronenmikroskopie (Bettina Purfürst, Séverine Kunz, Christina Schiel) und Proteinproduktion & Charakterisierung (Anja Schütz, Tracy Dornblut, Janett Tischer) für den Gerätezugang und die Instandhaltung danken.

Ich danke allen derzeitigen und ehemaligen Mitgliedern der AG Daumke und AG Heinemann, im Besonderen, Jeffrey Noel, Audrey Xavier, Saif Mohd, Elena Vazquez Sarandeses, Stephan Grunwald, Katja Fälber, Marie Witt, Arthur Alves de Melo, Séverine Kunz und Oleg Ganichkin, für die hilfreichen Tipps und Diskussionen. Des Weiteren danke ich Carola Bernert, Jeanette Schlegel und Sabine Werner für die Zuarbeit und Instandhaltung der Labore. Einen herzlichen Dank auch an Birgit Cloos für die administrative Unterstützung.

Ein besonderer Dank gilt meiner Familie, die mich während meines gesamten Studiums auf unterschiedliche Weise unterstützt hat. Vor allem mein Mann hat mir geholfen, die schwierigen Phasen meiner Promotion und den plötzlichen Tod meiner Mutter zu überstehen.

Selbstständigkeitserklärung

Hiermit versichere ich, dass die vorliegende Dissertation von mir selbstständig und ohne unerlaubte Beihilfe verfasst wurde und ich keine anderen als die angegebenen Quellen und Hilfsmittel (einschließlich Abbildungen, Tabellen u. Ä.) verwendet sowie wörtliche und sinngemäße Zitate als solche kenntlich gemacht habe; und dass diese Dissertation keiner anderen Fakultät oder Universität zur Prüfung vorgelegen hat.

Berlin, 23. September 2021

Kathrin Funck

Publications

(Addendum, added on 26.09.2022)

Parts of this thesis have been published after the submission (24.09.2021) and disputation (18.02.2022) in the following manuscript:

Bock-Bierbaum, T., Funck, K., Wollweber, F., Lisicki, E., von der Malsburg, K., von der Malsburg, A., Laborenz, J., Noel, J.K., Hessenberger, M., Jungbluth, S., Bernert, C., Kunz, S., Riedel, D., Lilie, H., Jakobs, S., van der Laan, M., and Daumke, O. (2022). Structural insights into crista junction formation by the Mic60-Mic19 complex. Sci Adv *8*, eabo4946.
Submitted: 07.02.2022; accepted: 15.07.2022; published: 31.08.2022

Coordinates and diffraction data have been deposited (01.10.2021) and released (07.09.2022) in the *Protein Data Bank* (PDB) with the accession codes 7PV0 and 7PV1.